Item No. 830-H-15   NASI.60:1158

NASA Technical Paper 1158

Preliminary Study of a Large Span-Distributed-Load Flying-Wing Cargo Airplane Concept

Lloyd S. Jernell

MAY 1978

NASA

105

NASA Technical Paper 1158

Preliminary Study of a Large Span-Distributed-Load Flying-Wing Cargo Airplane Concept

Lloyd S. Jernell
Langley Research Center
Hampton, Virginia

SUMMARY

A preliminary study has been conducted of an aircraft capable of trans-porting containerized cargo over intercontinental distances. The specifica-tions for payload weight, density, and dimensions in essence configure the wing and establish unusually low values of wing loading and aspect ratio. The structural weight comprises only about 18 percent of the design maximum gross weight. Although the geometric aspect ratio is 4.53, it is estimated that the winglet effect of the wing-tip-mounted vertical tails increases the effective aspect ratio to approximately 7.9.

Sufficient control power to handle the large rolling moment of inertia dictates a relatively high minimum approach velocity of 315 km/hr (170 knots). The airplane has acceptable spiral, Dutch roll, and roll-damping modes. A hardened stability augmentation system is required.

The most significant noise source is that of the airframe. However, for both take-off and approach, the levels are below the FAR-36 limit of 108 dB.

The design mission fuel efficiency is approximately 50 percent greater than that of the most advanced, currently operational, large freighter air-craft. The direct operating cost is significantly lower than that of current freighters, the advantage increasing as fuel price increases.

INTRODUCTION

Large, long-range, subsonic cargo aircraft of the future probably will use large cargo containers and have payload capabilities much greater than those of present-day aircraft. A design concept which holds promise for such an air-plane accommodates payload distribution along the wingspan to counterbalance the aerodynamic loads, with a resultant decrease in the in-flight wing bending moments and shear forces. Decreased loading of the wing structure, coupled with the very thick wing housing the cargo, is expected to result in relatively low overall structural weight in comparison with that of conventional aircraft.

There are many potential problem areas associated with this type aircraft, including aerodynamic efficiency, control (particularly in roll due to the high moment of inertia about that axis), and airport handling because of its large size. In order to evaluate some of these problems, the preliminary study of a large distributed-load cargo airplane was performed. Portions of this work were conducted by the Vought Corporation - Hampton Technical Center (contract NAS1-13500) under the technical direction of the Vehicle Integration Branch, Aeronautical Systems Division, Langley Research Center. Vought personnel included were C. B. Quartero, leader and mission analyst; G. F. Washburn, structures; P. Baldasare, mass properties; L. A. Bodin and R. R. Combs, Jr., aerodynamics; G. L. Martin, stability and control; W. A. Lovell, propulsion; and J. W. Russell, noise. The results of this study are summarized herein.

NASA-funded studies of alternate configurations are documented in references 1 to 3. A review of the current airfreight system and its future prospects is presented in reference 4.

SYMBOLS

Values are presented in both SI and U.S. Customary Units. The measurements were made in U.S. Customary Units.

A	aspect ratio
b	wing span
C_D	drag coefficient, $\dfrac{Drag}{qS}$
C_L	lift coefficient, $\dfrac{Lift}{qS}$
$C_{m_{0.25\bar{c}}}$	pitching-moment coefficient about $0.25\bar{c}$
C_n	yawing-moment coefficient, $\dfrac{Yawing\ moment}{qSb}$
C_{n_β}	directional stability parameter, $dC_n/d\beta$, per deg
c	local chord
$\bar{c}$	mean aerodynamic chord
c_a	speed of sound at ambient conditions
c_r	rudder local chord
c_{vt}	vertical tail local chord
D	diameter; also drag
F_b	blade passing frequency
g	gravitational constant
h	altitude, also height of vertical tail
h_{web}	height of wing-spar web
L/D	lift-drag ratio
M	Mach number

2

M'_X swept-wing-axes net limit bending moment

$M'_{Y_{ea}}$ net limit torsion about wing-box elastic axis

N_D number of fan blades

q dynamic pressure

q_s wing-box-skin shear flow

q_v wing vertical beam shear flow

q_{web} beam-web shear flow

r radius

S wing reference area

S_v vertical-tail area

S'_Z swept-wing-axes net limit shear

T thrust

$T_{t,a}$ ambient absolute temperature

$T_{t,jet}$ jet total absolute temperature

$\left(\dfrac{T_{t,2}}{T_{t,1}}\right)_{engine}$ ratio of total absolute temperature at low-pressure turbine discharge station to that at fan inlet station

$\left(\dfrac{T_{t,2}}{T_{t,1}}\right)_{fan}$ ratio of total absolute temperature at fan discharge station to that at fan inlet station

t thickness; also time

t_2 time to double amplitude

t/c wing-section thickness ratio

V velocity; also vertical shear

W gross weight

x distance from nacelle lip measured parallel to center line

Y cross-sectional neutral axis

α angle of attack, referenced to airfoil center line, deg

β angle of sideslip, deg

δ_e elevon deflection, positive for trailing edge down, deg

δ_f flap deflection, deg

δ_r rudder deflection, positive for trailing edge left, deg

ζ damping ratio

η wing station, measured from fuselage center line along center line of wing box

$\ddot{\theta}$ nose-down pitching acceleration at minimum demonstrated velocity and maximum gross weight, radians/sec^2

ϕ roll angle, deg

ω_n natural frequency

Subscripts:

elastic   nonrigid structure

le   leading edge

max   maximum

min   minimum

rigid   rigid structure

trim   trimmed condition

Notation:

BPR   ratio of inlet air mass flow of fan to that of core engine

c.g.   center of gravity

dB   decibels, referenced to 2×10^{-5} N/m^2

EAS   equivalent airspeed

EPNL   effective perceived noise level

HSAS   hardened stability augmentation system

Hz   Hertz

MLW   maximum landing weight

4

MIN DEM   minimum demonstrated velocity

OASPL   overall airframe sound pressure level

OWE   operating weight, empty

rpm   revolutions per minute

RLW   reserve-fuel landing weight

SPL   sound pressure level

TOGW   take-off gross weight

TSFC   thrust specific fuel consumption

ZFW   zero-fuel weight

BASIC DESIGN CRITERIA

The study required the preliminary design of a span-distributed load airplane capable of transporting large containers of cargo over transcontinental distances. The basic design criteria are as follows:

Configuration - flying wing, with wing-tip vertical tails and a relatively small fuselage for flight deck and crew accommodation

Wing planform - 30° sweep, no taper

Airfoil - t/c = 0.20, one of several Langley-developed airfoils or modifications thereof

Cargo-compartment dimensions - sufficient to handle 2.44 m × 2.44 m (8 ft × 8 ft) cargo containers of assorted lengths

Payload weight - 2 668 933 N (600 000 lbf)

Payload density - 1571 N/m^3 (10 lbf/ft^3), including container

Propulsion - current-production turbofan engines, scaled if necessary

Range - 5926 km (3200 n. mi.)

Cruise Mach number - at least 0.7

Runway length - 3658 m (12 000 ft) maximum

Cargo-compartment pressurization - none

Cargo loading location - at wing tips

CONFIGURATION DEVELOPMENT

The final configuration is shown in figure 1. The following sections give a description of the configuration and the fundamental design philosophy.

Wing

Planform.- Having specified sweep, taper ratio, container size, and pay-load weight and density, the remaining criteria pronouncedly affecting overall wing geometry were airfoil shape and cargo arrangement. Since the airfoils under consideration were similar in thickness distribution, cargo arrangement was the first variable studied to establish the approximate wing planform. Configurations accommodating two, three, and four rows of containers parallel to the wing leading edge were considered. The two-row configuration provided an aspect ratio of approximately 7.6, but required a span of roughly 134 m (440 ft). It was felt that a span of this magnitude not only would pose serious runway and cargo-terminal compatability problems, but would also exact consider-able structural-weight penalty in order to insure sufficient wing stiffness for maximum maneuver and taxi loads.

In contrast, the four-row arrangement reduced the required span to approxi-mately 66 m (215 ft), but also reduced the aspect ratio to approximately 3.1. This configuration obviously would have lower aerodynamic efficiency because of the higher induced drag. Consequently, the three-row configuration, having a span of approximately 88 m (290 ft) and an aspect ratio of approximately 4.5, was chosen as having the best compromise between structures, aerodynamics, and ground operations.

It should be pointed out that the specifications for payload weight, density, and dimensions in essence configure the wing and establish the wing loading. No attempt was made to employ twist as a means of altering the span-wise load distribution since it would require either larger payload-structure clearances or create loading problems because the cargo floor would not be level. It was determined early in the study that the configuration would have a wing loading of only about 3352 N/m^2 (70 lbf/ft^2). Although it follows that because of the low span loading in comparison with conventional aircraft, the configuration would have relatively low induced drag; it also would exhibit relatively high profile drag because of the high thickness ratio.

Airfoil.- The airfoil selection was based primarily on the need for a two-dimensional critical Mach number of approximately 0.7, very low pitching moment, and maximum utilization of wing volume for the cargo compartment. Data on supercritical airfoils developed to date indicate that this type of profile would meet the cruise speed and volume-utilization requirements; however, most supercritical airfoils inherently display large negative pitching moments because of the relatively severe rearward camber.

Limited research has been conducted at the Langley Research Center on thick airfoils applicable to span-loaded aircraft. These airfoils typically have the large leading-edge radius and thickness distribution characteristic of supercritical airfoils, but are cambered so as to provide low pitching

moment. Two airfoils were selected as candidates for application to the present design study. One utilized a moderate amount of positive camber over approximately the forward 70 percent of the chord, but was reflexed over the remaining rearward section to provide an essentially zero pitching moment about the quarter chord. The other airfoil was a modification of an early super-critical airfoil in which the camber was removed and the thickness ratio increased to 0.20.

Early in the design study, unpublished wind-tunnel data became available on a 30° sweep, distributed-load cargo aircraft model incorporating the afore-mentioned reflexed airfoil. These data indicated that at cruise Mach number and angle of attack, boundary-layer separation existed over roughly the rear-ward 30 percent of the upper surface (the region of the reflexed surface). Sufficient data were not available to ascertain whether the separation was a Mach number effect or due simply to the low test Reynolds number. Furthermore, theoretical data from the analysis program of reference 5 (which computes the flow field about an airfoil at supercritical Mach numbers) predicts that for an assumed lift coefficient of 0.40, the drag-rise Mach number for the reflexed airfoil is 0.03 less than that for the symmetrical airfoil. In addition, pre-liminary layouts of the wing structure for both airfoils showed that the sym-metrical airfoil was slightly more efficient in terms of wing volume utili-zation for the cargo compartment. Hence, the symmetrical airfoil was selected for the design study.

Dihedral.- A wing dihedral angle of 3° was employed to alleviate the need for the relatively long main landing gear required to provide for ground clear-ance of the wing tip and deflected elevon during landing and take-off.

Fuselage

The fuselage was originally configured solely for flight deck, crew accom-modation, and nose gear. However, it was later found necessary to install a fuel tank in the unused volume so as to provide a greater range of center-of-gravity management.

Vertical Tails

The wing-tip-mounted vertical tails, designed according to the suggested guidelines of reference 6, have a quarter-chord sweep of 30°, a taper ratio of 0.30, and an aspect ratio of 2.31. The airfoil used is an 8-percent-thick modification of the GA(W)-1 airfoil (17-percent thickness) described in refer-ence 7. The nonplanar lifting surface method of reference 8 was used to opti-mize cant and toe-in angles of the fins for the best combination of aerodynamic efficiency and structural weight.

Engines and Nacelles

The configuration has six turbofan engines (scaled from the JT9D-7 engine) to provide the required thrust. The engines, mounted on pylons above the wing,

were originally positioned so that roughly 80 percent of the nacelle was ahead of the wing leading edge. Later it was necessary to move the nacelles rearward to lessen the large adverse effect of the nacelles and pylons on directional stability as well as to avoid possible adverse interference drag from pylons located within the supercritical flow region of the upper surface of the wing. In the final position, the nacelle inlet lip is located at approximately the 35-percent local-chord station.

Controls and High-Lift System

The elevons have a chord equal to 20 percent of the wing chord, and extend from the 60-percent semispan station to the vertical tails. Maximum elevon deflection is $\pm 40^\circ$. The spoilers, required to augment roll control because of the high inertia in roll, have a chord equal to 15 percent of the wing chord and are located inboard on the wing as shown in figure 1. The nonsplit rudders have a chord equal to 20 percent of the vertical-tail local chord and a maximum deflection of $\pm 40^\circ$. The high-lift system consists of simple trailing-edge flaps having a chord equal to 15 percent of the wing chord and extending from the wing center line to the 60-percent semispan station. Maximum flap deflection is 20°.

Fuel Tanks

The fuel tanks are located as shown in figure 2. The wing tanks are positioned ahead of the front wing box beam and behind the rear beam. The forward tanks extend outward to the 50-percent semispan station, whereas the rearward tanks extend to the inboard main gear wheel wells. The fuselage tank was provided to widen the range of control over the center of gravity.

Landing Gear

The landing gear (see fig. 1) is composed of a twenty-wheel, four-strut main gear and a two-wheel nose gear. The inboard pair of main gear, utilizing six-wheel bogies, are located rearward of the wing-box rear beam at approximately the 33-percent semispan station. The outboard gear have four-wheel bogies and are positioned forward of the wing box front beam at approximately the 77-percent semispan station. To facilitate landing load distribution, the oleo-pneumatic suspensions of the pair on each side are interconnected. A landing gear of this configuration might require steering of at least one pair of main gear; however, such an analysis was beyond the scope of this study.

STRUCTURES

Since all structural components other than the wing box are of conventional design, the structural analyses of these items were confined to component layout and determination of mass properties using statistical data. Because of the unique geometry and loading requirements of the wing, a detailed study was performed wherein the wing-box structural concept was developed and the dimensions of its structural components were analytically determined.

The final wing-box design, shown in figure 3, incorporates conventional stiffened, stressed-sheet structure constructed primarily of 2024-T3 aluminum, 7075-T6 aluminum being employed where the higher allowable stress can be used to advantage. Two vertical beams, reinforced by vertical stiffeners, are connected by beam-type upper and lower rib caps which, in turn, are supported by tension tubes located between the cargo bays. The rib caps support the stringer-stiffened wing skins. The lower rib caps also support the spanwise beams of the cargo subfloor. Figure 4, which shows a cross section of the wing normal to the leading edge, provides additional details of the wing box at a typical rib station.

Maximum design loads criteria established early in the study are

(a) 2.5-g balanced flight maneuver at maximum gross weight and cruise Mach number and altitude and

(b) 2.0-g taxi at maximum gross weight

The final structural analysis is based on the following additional conditions:

(1) Maximum design gross weight of 6 052 250 N (1 360 600 lb)

(2) For 2.5-g flight maneuver, the center of gravity is located at $0.29\bar{c}$, M = 0.75, and altitude, 8595 m (28 200 ft)

(3) For 2.0-g taxi, the center of gravity positioned at $0.35\bar{c}$

The procedures employed in the design of the wing box are based on the methods of reference 8. Although the analyses are of comparatively limited scope, the results are considered to be adequate for preliminary design purposes. The values of wing shear, bending moment, and torsion, calculated for the maximum-design-load conditions, are shown in figures 5, 6, and 7, respectively. The airloads for 2.5-g flight maneuver were calculated by using a computer program based on the method of reference 9.

Because of the simple wing-box geometry and the desire to minimize component gage changes, structural analyses were conducted only at the eight structural semispan stations shown in figure 8. As will be noted, two stations represent the ribs supporting the inboard and outboard main gear. A shear flow diagram similar to that of figure 9 was generated at each station to determine beam-web and skin thicknesses.

The vertical shear is distributed equally between the two vertical beams. The beam webs are permitted to buckle and are designed to carry the vertical shear and the wing-skin shear flow due to torsion with the webs in the diagonal tension-field condition. The variation of web thickness along the structural semispan is shown in figure 10. The web stiffeners, spaced at 38.10 cm (15 in.) intervals, are of the geometry shown in figure 11. The spanwise variation of stiffener cross-sectional area is presented in figure 12.

The beam caps, stringers, and skins are designed to carry all bending loads. In addition, the skins, which are allowed to buckle, also support the chordwise shear loads due to torsion. Hence, the sizing of these components and determination of stringer spacing required several iterations. The loads on the beam caps and stringers (including effective skin) were calculated at the eight semispan stations using a distance of 307.34 cm (121.00 in.) between beam-cap centroids and an average distance of 365.76 cm (144.00 in.) between stringer centroids. Sectional geometries of these components are shown in figure 11. The spanwise variation of beam-cap and stringer cross-sectional areas are presented in figures 13 and 14, respectively. For a given skin thickness, the allowable buckling chordwise shear stress is proportional to stringer spacing; therefore, the close stringer spacing (20.42 cm (8.04 in.)) allows a relatively high buckling stress. The variation of skin thickness along the semispan is shown in figure 15.

The wing box structure includes 130 frame-type ribs. In addition, four beam-type ribs of heavier forged aluminum are located at the main-gear attachment points. All ribs are spaced at 76.20-cm (30.00-in.) intervals. The upper and lower I-beam rib caps are designed for the load resulting from the 2.5-g flight maneuver. The analysis and sizing were performed only at wing station 2001.32 cm (787.92 in.) (measured along the wing box center line), which is the location of the rib supporting the inboard main gear. The rib cap loads at this point were assumed to be typical of those throughout the wing box.

The cargo subfloor structure consists of the lower rib cap, which also serves as the main chordwise subfloor beam, and four spanwise beams located below each of the three cargo bays. The spanwise beams, consisting of upper and lower caps and stiffened webs, have a 25.40 cm (10.00 in.) depth determined by design layout. No structural analyses were performed on the subfloor components.

Although the study airplane exhibits a low ratio of structural weight to gross weight in comparison with conventional cargo aircraft, weight reduction is limited since neither weight nor the external loads are uniformly distributed along the span. Component weights of such items as propulsion units, fuel and tanks, and landing gear cause considerable spanwise variation of weight, and realistically, even the assumed uniform distribution of payload weight is an ideal case which would rarely be encountered. With regard to external loads, the airloads are not uniform because of the aforementioned impracticability of utilizing wing twist. The results of the studies indicated that the extreme depth of the spars is not as advantageous as might be expected since the failure modes occur in buckling with very low maximum allowable stress. Preliminary estimates, wherein extrapolations of empirical data representing all-aluminum structures were utilized, indicated a wing structural weight of approximately 287 N/m^2 (6 lbf/ft^2); however, detail design studies predicted an all-aluminum weight of approximately 421 N/m^2 (8.8 lbf/ft^2). Further studies, wherein it was assumed that 90 percent of the wing secondary structure, control surfaces, and flaps could be constructed of epoxy composite material, indicated that the overall wing weight could be reduced to 402 N/m^2 (8.4 lbf/ft^2).

The mass properties analysis consisted of the determination of aircraft weights, moments of inertia, and center-of-gravity ranges. Mass properties of the wing box were obtained analytically by using data generated during the structural design. Those of the wing secondary structure, control surfaces, and flaps were estimated by using statistical data, with an adjustment for a 20-percent component weight reduction through the use of epoxy composite material for 90 percent of the structure. The fuselage properties are those of a typical subsonic transport forebody, adjusted for structural modification due to the increased loads of the nose gear and fuselage fuel tank. Data for the vertical tails, landing gear, nacelles, and fuel system were obtained statistically with the use of a computer program developed by Vought-Hampton. The mass characteristics of the scaled JT9D-7 engines were calculated with the use of engine data and scale factors provided by the manufacturer. Mass properties of all other items were obtained from data for a large commercial transport currently in operation, with adjustments applied where appropriate.

The weight breakdown by component and by group is listed in table I. The airplane has an operating empty weight of 1 719 682 N (386 600 lbf) and a design gross weight of 6 052 250 N (1 360 600 lbf). A bar graph of the weight breakdown is provided in figure 16. The structural weight comprises only about 18 percent of the maximum gross weight and exemplifies the magnitude of structural efficiency achievable through the utilization of the span-distributed loading concept. Unpublished in-house studies by several airframe manufacturers indicate that roughly 95 percent of the available air freight market would not require pressurization; therefore, no studies were conducted to determine the structural weight penalties associated with pressurizing the cargo compartment.

The moments of inertia about the stability axes and the product of inertia about the principal axis are presented in table II for several significant conditions. Of course, the roll inertial moment is relatively much greater than those of conventional cargo aircraft which carry the payload in the fuselage.

The center-of-gravity gross-weight envelope is presented in figure 17 for an assumed uniform design-payload distribution and also for the ferry mission. The forward center-of-gravity limit represents the restriction imposed by the available control power for aircraft rotation during take-off. The rearward limits represent longitudinal dynamic stability restrictions. As will be noted, for both the design-payload and ferry missions, the rearward dynamic limits during the approach mode severely restrict utilization of the reserve fuel. However, the resolution of this problem was not pursued because of the limited scope of the study. The optimum cruise center-of-gravity position (zero elevon deflection) is 0.29$\bar{c}$. The fuel distribution for various points on the center-of-gravity gross weight (GW) envelope are presented in table III.

AERODYNAMICS

Because of the high span and inherent low wing loading associated with this configuration, both span and chord were held to the minimum required for

cargo containers, container clearance, and structural thickness. Based on the results of the final structural analysis, values chosen for the span and stream-wise chord are 88.39 m (290.00 ft) and 19.51 m (64.00 ft), respectively. The resultant aspect ratio is 4.53.

In comparison to current cargo aircraft, the configuration has numerous unconventional features which affect the aerodynamic characteristics, including the low values of wing loading and aspect ratio, a high section-thickness ratio, wing-tip-mounted vertical tails, no horizontal tail, and upper-surface-mounted engines.

In comparison to conventional cargo aircraft, the study airplane exhibits relatively low induced drag due to the low span loading. However, the configuration develops relatively high profile drag due to the high thickness ratio. Also, the high thickness-ratio wing posed a design challenge because of the large adverse pressure gradients over the rearward surfaces at cruise condi-tions, which resulted in an increased tendency for flow separation. The reso-lution of the separation problem was complicated by the requirement for very low pitching moment, which negated full implementation of supercritical airfoil technology. In the latter part of the study, an effort was made to employ a small amount of camber to improve the aerodynamic efficiency; however, this approach was abandoned because of center-of-gravity limit problems. Friction drag was calculated by standard methods, using flat-plate turbulent friction coefficients adjusted for the effects of supervelocity, interference, pro-tuberances, gaps, and boundary-layer separation near lifting-surface trailing edges. Nacelle drag was also adjusted for boattail effects and loss of leading-edge suction.

The induced drag was calculated by using the method of reference 9. In this method the configuration was represented as planar surfaces conforming to the camber planes of the wing and vertical tails. Although the geometric aspect ratio is only 4.53, the effect of the wing-tip-mounted vertical tails is to increase the effective aspect ratio to approximately 7.9.

A tailless design incurs large trim drag penalties if the trimming moments are obtained by means of the elevons. This effect is even more pronounced in the present configuration since a moderate upward deflection of the elevon significantly decreases the induced efficiency increment of the vertical fin. Thus, trim is obtained by fuel management wherein fuel is pumped between tanks so as to maintain zero elevon deflection; in cruise, therefore, trim drag is zero. At take-off and landing, dynamic stability limits the allowable travel of the center of gravity. Appropriate trim-drag penalties were assessed against the aircraft in the landing and take-off configurations.

The increase in drag due to localized supersonic flow was determined from two-dimensional airfoil calculations by using the computer program of refer-ence 5. Adjustments were made for three-dimensional effects using simple sweep theory. Drag-rise increments of the fuselage, and engine nacelles and pylons were neglected since sufficient experimental data were not available. However, it is believed that the contributions of the components are relatively small.

The lift characteristics, including flap and elevon deflections, were obtained by using the computer program of reference 10. This method calculates the aerodynamic characteristics of wing-body-tail combinations in subsonic and supersonic potential flow. The wing and fuselage of the configuration are represented as a large number of panels, each of which contains aerodynamic singularities. Because of the limitations of the program, the engine nacelles and pylons were not included in the input geometry; however, the effects of these components on lift are believed to be minor because of engine location. The method of reference 11 was employed to account for the effects of engine exhaust on cruise lift and drag.

Lift-drag polars, with and without ground effect ($h/b \approx 0.1$ and $h/b \gtrsim 1$), are shown in figures 18 and 19 for the landing and take-off modes, respectively. A flap deflection of 20° is used for both take-off and landing. The difference in polars for the two flight modes is due to thrust effects on trim requirements. Figure 20 presents the variation of lift with angle of attack for the aforementioned flight conditions.

Cruise lift-drag polars are shown in figure 21. The corresponding lift-drag ratios are shown in figure 22. The curve for $M = 0.75$, which has a maximum lift-drag ratio of 19.00, compares favorably with the combination of lift-drag ratio ($L/D = 18.65$) and specific fuel consumption computed for the cruise mode. As will be discussed in the section "Mission Analysis," these optimum values correspond to the maximum range as determined from the Breguet range equation.

STABILITY AND CONTROL

The static and dynamic analyses of the aircraft stability and control are based on data generated by the method of reference 10, the data of reference 12, the previously discussed aerodynamic and mass-properties data, and the methods of reference 13.

Criteria

The criteria employed in determining the stability and control requirements were obtained from reference 14, with the exception of the longitudinal dynamic guidelines, which are based on unpublished data. The longitudinal criteria are as follows:

(a) For all weights and center-of-gravity positions, the time to double amplitude shall be greater than 2 seconds (SAS requirement because aircraft is statically unstable over most of operational center-of-gravity range).

(b) The forward center-of-gravity position during take-off shall be determined by the ability to provide the required control power for aircraft rotation and to maintain take-off lift coefficient.

(c) The rearward center-of-gravity position during approach shall be determined by the ability to provide a nose-down pitching acceleration of 0.08 rad/sec^2 at minimum demonstrated velocity and maximum gross weight.

The criteria for determining the lateral-directional stability and control requirements are as follows:

(a) The aircraft shall have positive effective dihedral.

(b) The aircraft shall be directionally stable for all flight modes.

(c) There shall be adequate on-the-ground directional control to provide trim in a 56-km/hr (30-knot), 90° cross wind.

(d) The minimum cross-wind control velocity shall be sufficiently low to allow nose-wheel steering.

(e) There shall be adequate directional control to counteract an outboard engine failure at maximum-thrust engine-failure velocity.

(f) At approach velocity, the lateral control shall be sufficient to provide a roll-response capability of 30° within 2.5 seconds after initiation of a rapid, full lateral control input.

(g) At approach velocity, the directional control shall be capable of providing a sideslip angle of 10° with not more than 75 percent of full lateral control required to maintain wings-level flight.

(h) The aircraft shall have an inherent Dutch roll stability.

Longitudinal Stability and Control

The estimated control capabilities of the aircraft for an elevon-deflection range of ±40° and a center-of-gravity position of 0.25c̄ are shown in figures 23 to 25 for the cruise, initial climb-out, and approach modes, respectively. Flap deflections employed were 0° for cruise, and 20° for both climb-out and approach. The data exhibit the pronounced effect of elevon deflection on lift coefficient. In fact, upon comparing elevon and flap size, it is obvious that the variations of lift and drag due to elevon deflection are of the same order of magnitude as those resulting from flap deflection. Hence, for the study airplane it is especially important that, where practicable, trim be accomplished by center-of-gravity management rather than by elevon employment. However, for the initial climb-out and for approach modes, which require high lift coefficients, the center of gravity should be positioned at the rearward limit in order to maximize available lift for maneuvering.

Estimates of elevon deflection required to trim the aircraft for various center-of-gravity positions during initial climb-out, cruise, and approach are presented in figure 26. It will be noted that cruise-mode trim with 0° elevon deflection requires a center-of-gravity position of approximately 0.29c̄. The

14

data also show the significant effect of center-of-gravity position on elevon deflection required for trim during climb-out and approach.

The longitudinal-control capabilities for the climb-out and approach modes are replotted in figures 27 and 28, respectively, along with the statically determined limits for center-of-gravity travel and the corresponding trimmed lift coefficients. The climb-out forward static center-of-gravity limit of $0.28\bar{c}$ was determined by the control power required to rotate the aircraft at a velocity of 263 km/hr (142 knots) at maximum take-off gross weight. The rearward static center-of-gravity limit for both climb-out and approach is $0.50\bar{c}$ and is based on the ability to provide a nose-down pitching acceleration of 0.08 rad/sec^2 at minimum demonstrated velocity and maximum gross weight. The approach forward static center-of-gravity limit of $0.23\bar{c}$ is not determined by maximum control power, but on the ability to attain a lift coefficient 1.5 times the approach lift coefficient. Since the aircraft is statically unstable over most of the center-of-gravity range, a hardened stability augmentation system (HSAS) is required for stability. (HSAS is a backup stability augmentation system having a reliability comparable to that of the primary structure.)

Controls-fixed dynamic analyses of the aircraft were conducted for the climb-out and approach modes. The estimated time required to double amplitude as a function of center-of-gravity position is shown in figure 29. According to unpublished data, a 2-second minimum time to double amplitude is the limit for which a current HSAS would be able to provide adequate stability. The resulting rearward center-of-gravity limit for the initial climb-out at maximum gross weight is $0.309\bar{c}$. For the approach mode, the rearward limits are $0.304\bar{c}$ and $0.318\bar{c}$, respectively, for the maximum and reserve-fuel gross weights. These limits, which impose greater restrictions on rearward center-of-gravity travel than the aforementioned static limit, prevent the use of elevon settings optimized for maximum lift during take-off and landing. Therefore, efficient operation of the aircraft in these flight modes would require the development of a very rapid reaction (fast response) control system. However, such a system, which might include small secondary surfaces on the elevons, was not analyzed in the present study.

The rearward dynamic center-of-gravity limit for the clean configuration during the climb and acceleration mode is shown in figure 30 (for the minimum time of 2 seconds to double amplitude). The rate of change of the rearward limit with aircraft velocity is sufficiently low to allow the use of fuel transfer for maintaining the center of gravity within the required limits.

Lateral-Directional Stability and Control

The methods of reference 13 were employed in determining the lateral-directional characteristics. Although the engine nacelles and pylons generate a large part of the side force, these components have a relatively small effect on yawing moment since their longitudinal position is near the aircraft center of gravity. The vertical tails are considerably larger than those required to meet the criterion that $C_{n_\beta} > 0$. However, tail design was not based on

directional stability minimum requirements. Instead, the tails were designed primarily to increase aerodynamic efficiency by following the winglet design guidelines. (See ref. 6.)

Figure 31 exhibits the effects of control deflection and local rudder-tail chord ratio on the directional control capability of the aircraft. Also shown is the minimum control power necessary to meet the requirement of maintaining a straight flight path during take-off with an outboard engine inoperative. Based on these data, a rudder-tail chord ratio of 0.2 and a maximum deflection of $\pm 40^{\circ}$ were selected.

The lateral response of the aircraft was estimated by solving the single-degree-of-freedom equation of motion in roll for a maximum step control input. The results are presented in figure 32 for the three levels of flying quali-ties requirements specified in reference 14. The data indicate that the air-plane has satisfactory roll response at an approach velocity greater than 315 km/hr (170 knots); this is a considerably higher velocity than the 278 km/hr (150 knots) believed to be desirable. The level-2 requirement can be met at a velocity of 248 km/hr (134 knots). These speeds, rather than maximum lift, control the aircraft approach speed. A lower approach velocity could be attained by a roll-response requirement reduced from those of reference 14. Extensive development of more powerful lateral control systems would be neces-sary to reduce the landing speed further; however, such development is beyond the scope of this study.

The ability of the aircraft to meet steady-sideslip trim requirements during take-off and landing was estimated by solving the two-degree-of-freedom equations for roll and yaw steady-state trim. The results indicate that 36 per-cent of the maximum rudder deflection and 46 percent of the maximum elevon deflection are required to maintain a wings-level approach with a 10° sideslip angle. This is well within the specified allowable limit of 75-percent maximum control deflection.

Figure 33 shows the minimum elevon and rudder deflections required for lateral and directional control during the take-off ground run with a 56-km/hr (30-knot), 90° cross wind. It will be noted that adequate control is available about both axes at a minimum velocity of 145 km/hr (78 knots). Control at lower velocities can be accomplished by nose-wheel steering.

An examination of the roots of the characteristic equation of motion indi-cates that the airplane has acceptable spiral and Dutch roll modes and an accept-able roll-damping mode. Table IV presents a comparison of the inherent lateral-directional characteristics of the airplane with the assumed requirements.

PROPULSION

The engines selected for the study are scaled JT9D-7 turbofans which have been sized to provide an installed static thrust of 240 200 N (54 000 lbf) each

at sea-level standard atmosphere conditions. The engine is of two-spool, axial-flow design with high bypass and compression ratios. The production engine maximum ambient temperature limits for constant thrust, as recommended by the manufacturer, are as follows:

(a) Take-off thrust - standard day + 12° C

(b) Maximum climb thrust - standard day + 10° C

(c) Maximum cruise thrust - standard day + 15° C

Although permitted within these recommended limits, constant thrust operation above standard day temperature results in a considerable increase in fuel consumption. A detailed description of the production engine, along with basic (uninstalled) performance data, is presented in reference 15.

The unscaled, installed engine performance data were generated by correcting the basic performance data for inlet recovery, service airbleed, and auxiliary power extraction by using the methods of reference 15.

Typical installation losses in the study airplane engine performance are as follows:

M	h		Thrust rating	Atmospheric conditions	Percent change	
	m	ft			T	TSFC
0	0	0	Take-off	Standard day + 10° C	-8.5	1.6
.40	6 100	20 000	Maximum climb	Standard day	-5.3	2.7
.75	10 670	35 000	Maximum cruise	Standard day	-5.5	4.6

With the exception of take-off performance, the data are based on sea-level standard atmospheric conditions. However, the take-off data were computed for sea-level standard day + 10° C since, as specified in Federal Aviation Regulations, Part 36, these are the atmospheric conditions at which engine noise shall be evaluated. These atmospheric conditons also meet the Federal Aviation Regulations Part 25 requirements for determining aircraft take-off performance.

The data indicate that at take-off velocities and altitudes, the primary and fan nozzles are operating subcritically; that is, the fully expanded exhaust flow areas are equal to the respective nozzle throat areas.

The inlet recovery presented in figure 34 is based on the geometry of an inlet employed in the study documented in reference 16. Although the inlet was originally designed for a cruise Mach number of 0.98, it was selected for the present study since it exhibits a relatively high pressure recovery of 0.994 at the cruise Mach numbers considered herein. It was assumed that the inlet mass flow is equal to that required by the engine throughout the flight envelope;

17

hence, performance was not penalized for inlet spillage drag. The engine service airbleed schedule is shown in figure 35. Power extraction for electrical and hydraulic systems was held constant at 48.5 kW (65.0 hp). It was assumed that the nozzle efficiencies of the scaled and reference engines are of equal magnitude; therefore, no additional performance penalties were assessed for nozzles.

The characteristics of the scaled engine were obtained by using the methods of reference 17. Flow rate, exhaust gas mass flow, and fully expanded exhaust gas area were adjusted by the relative thrust ratio (ratio of required installed thrust to production engine installed thrust). The effects of relative thrust ratio on fan rotational velocity (rpm), and engine weight and dimensions are shown in figure 36. The weight of the scaled engine is 54 206 N (12 186 lbf), including manufacturer-furnished standard equipment. This weight does not include the inlet, fan cowling, nozzles, or engine-driven airframe accessories. The installed performance data for the climb and cruise modes are presented in figures 37 to 41. Data for the take-off and part-power cruise modes are shown in figures 42 to 49.

The nacelle incorporates a full-length fan duct, and coplanar primary and fan nozzles. The inlet length is equal to the maximum inlet diameter. The nozzle lengths are equal to 1.5 times the primary nozzle diameter. The maximum nacelle diameter is equal to the maximum inlet diameter plus 40.6 cm (16.0 in.) for engine-driven accessories and nacelle ventilation. The nacelle external dimensions are presented in table V.

MISSION ANALYSIS

The design-mission criteria specify that the aircraft shall be capable of transporting a 2 668 933 N (600 000 lbf) payload a minimum distance of 5926 km (3200 n. mi.) at a cruise Mach number of at least 0.7 and shall require a runway length no greater than 3658 m (12 000 ft). (See section "Basic Design Criteria.") As previously mentioned, the engine selected for the study is a scaled JT9D-7 turbofan. The purpose of the mission analysis is to optimize the required thrust for minimum fuel consumption and to obtain the required fuel weights and gross weights, as well as to determine the performance. All performance characteristics are based on standard atmospheric conditions, take-off and landing data being calculated for sea-level altitude.

Performance Criteria

The criteria employed in determining the various performance parameters are:

Take-off.- The take-off distance, based on Federal Aviation Regulations, Part 25, is defined as the greater of either 1.15 times the all-engine take-off distance or the balanced field length with one engine inoperative. Fuel allowance includes 10 minutes at taxi power and 1 minute at take-off power.

Acceleration and climb.- A constant equivalent airspeed shall be maintained until the cruise Mach number is reached.

Cruise.- A cruise climb shall be performed at altitudes optimized for minimum fuel consumption unless constrained by the service ceiling.

Reserve fuel.- The total mission fuel shall include the reserves recommended by the Air Transport Association for international flights, consisting of allowances for:

(a) Increased trip time of 10 percent

(b) Missed approach, followed by acceleration to climb velocity

(c) Flight to alternate airport, 370-km (200-n. mi.) distance

(d) Hold for 30 minutes at an altitude of 457 m (1500 ft)

Method of Analysis

The take-off and landing performance data were generated with the use of unpublished computer programs developed by the Vought Corporation, Hampton Technical Center. Mission performance was evaluated with the use of an unpublished mission analysis computer program developed at the Langley Research Center.

Performance Characteristics

Preliminary estimates indicated that because of the relatively low wing loading, engine size is determined by cruise ceiling rather than by take-off field length. In order to determine the design mission engine size and fuel weight, several iterations of the mission performance calculations were required. The final results, presented in figure 50, show the effects of installed thrust on take-off field length and design mission range. These data are based on a mission fuel weight of 1 663 635 N (374 000 lbf). The selected scale represents an engine which generates a sea-level standard day installed take-off thrust of 240 204 N (54 000 lbf). The corresponding design mission range is 5954 km (3215 n. mi.). The take-off field length at maximum gross weight with 20° flap deflection is 2499 m (8200 ft), which is considerably less than the specified maximum allowable field length. The effect of engine size on operating empty weight and gross weight are shown in figures 51 and 52, respectively.

Take-off rotation is initiated at a velocity of 252 km/hr (136 knots). Lift-off is accomplished at an angle of attack of 5.5° and a velocity of 282 km/hr (152 knots). The climb segment is performed at an equivalent airspeed of 519 km/hr (280 knots).

The effects of cruise Mach number on the design mission lift-drag ratio and range are shown in figure 53. A reduction in Mach number to 0.68 results in an

increase in mission range to 6543 km (3533 n. mi.), which is 10 percent greater than that for a cruise Mach number of 0.75.

The effects of gross weight on approach velocity and landing distance for a flap setting of 20° are presented in figure 54. The approach employs a 3° glide slope. The relatively high approach velocity is determined by the roll response capability of the aircraft. The spoilers assist in braking during the ground roll. The landing distance for the design mission landing weight is 3018 m (9900 ft). For the design mission take-off gross weight, the distance is 3200 m (10 500 ft).

The variation of payload capability with range is shown in figure 55. For the lower payloads, the aircraft is capable of very long range because of the large wing volume available for fuel stowage.

A summary of the design mission performance characteristics is presented in table VI. Of particular interest is the design mission fuel efficiency, which is estimated to be 1.19 Mg-km/N (3.16 ton-n. mi./lbf) of fuel burned. This value is approximately 50 percent greater than that of the most advanced, currently operational, large freighter aircraft.

NOISE

The engine and airframe noise characteristics of the study airplane during take-off and approach were estimated at the measurement points (ref. 18) shown in figure 56. Point 2 represents the location of maximum sideline noise along a line parallel to and 649 m (0.35 n. mi.) from the runway center line. The methods employed and the results are discussed in the following sections.

Method of Analysis

Engine noise.- The noise characteristics of the fan and jet were evaluated separately and then combined to determine the overall engine noise level. The fan noise characteristics were determined according to the method of reference 19, which predicts the variation of fan sound pressure level SPL with frequency and directivity at a source noise radius of 46 m (150 ft). Frequency and directivity angle are treated as functions of fan performance factors. This technique assumes that a fraction of the mechanical work is converted into output sound power; hence, both the total temperature rise and mass flow of the fan were used in determining the fan source noise. Fan noise is also affected by the design and operating Mach numbers of the rotor tips, the number of stator vanes, the blade-passing frequency, and the rotor-stator spacing ratio. The blade passing frequency is the product of the number of fan blades and fan revolutions per second. The rotor-stator spacing ratio is the average axial distance between the rotor blades and stator vanes divided by the average rotor-blade axial length. Table VII lists typical input parameters used to predict the fan-source-noise sound pressure level for each engine. It should be noted that the fan total temperature rise, mass flow, and rotational velocity are dependent on engine performance, which varies during the take-off mode.

The jet noise characteristics of the engines were predicted by using the coannular and single jet methods of reference 20, which predict the variation of jet noise sound pressure level with frequency and directivity angle at a source radius of 46 m (150 ft). The magnitude of the jet noise is dependent on aircraft velocity and the flow characteristics of each jet, including exit area and velocity, mass flow, total temperature ratio, and density. Typical input parameters for predicting coannular jet noise are listed in table VIII.

Following thrust cutback, the mass flow of the fan jet is considerably greater than that of the primary jet (see table VIII). Therefore, for this segment of the take-off mode, the jet noise was determined by applying the single jet method to the fan exit flow. Figure 57 shows the variation of the source noise sound pressure levels with frequency at a directivity angle of 130° for both the fan and jet following thrust cutback. As indicated, jet source noise is predominant at the lower frequencies, whereas fan source noise is greater at the higher frequencies. However, at the observer locations, the jet noise levels are predominant because of atmospheric attenuation of the high frequency fan noise.

Before combining the source noise values of the fan and jet, corrections were applied to each spectra to account for the wing shielding effects due to mounting the engines above the wing. Based on preliminary data correlations by the Pratt and Whitney Aircraft Group, noise reductions of 3 dB were applied where the wing interferes with the fan or jet noise source directivity. For the study airplane, these reductions were applied to the fan source noise at angles greater than 20° relative to the engine inlet axis and to the jet source noise at angles less than 100° relative to the inlet axis. The resulting levels of fan and jet noise were then added at the one-third common octave band frequencies to obtain a total engine noise spectra over the applicable ranges of directivity.

For a given instant during take-off the engine source noise is computed at the observer location along the directivity angle determined by the observer position relative to the aircraft. The prediction method includes the effects of tone, spherical divergence, atmospheric attenuation, multiple engines, and ground reflection. Thus, at each observer station on the ground at a particular instant, there is a preceived noise level generated by the engines. The time history of the perceived noise level is then integrated to obtain an effective perceived noise level (EPNL) at each observer position.

Airframe noise.- Reference 21 presents the results of a study in which airframe noise data were correlated for multiengine commercial and military aircraft with aspect ratios from approximately 7 to 10. As part of the study documented in reference 22, airframe noise was also evaluated for an arrow-planform supersonic transport configuration having an aspect ratio of approximately 1.9. Since the study airplane has an aspect ratio of 4.53, it was assumed that airframe noise could be approximated by averaging the values predicted by the reference methods. Figure 58 shows the minimum altitude as a function of fly-over velocity for an airframe noise level of 108 dB at the FAR 36 center-line measurement point as predicted by the reference methods. Also shown is the curve representing the estimated noise level of the study airplane. However, as previously mentioned in the section "Aerodynamics," the winglet effect of

the vertical tails increases the effective (aerodynamic) aspect ratio to approximately 7.9. Hence, it is believed that the average-value curve representing the study airplane may be somewhat conservative.

Predicted Noise Levels

Engine noise at take-off.- In order to minimize engine noise at the center-line measurement point (located 6486 m (3.5 n. mi.) from the break-release point), engine thrust was reduced 5944 m (19 500 ft) from brake release. The thrust cutback point was determined from the results of a previous study reported in reference 23. To optimize the noise level of the study airplane at the measurement points, the take-off profile was varied to evaluate the effect of cutback altitude on the engine effective perceived noise level (EPNL) at both the sideline and center-line measurement points. Figure 59 indicates that as altitude is increased engine sideline noise increases and center-line engine noise decreases. Figure 59 also exhibits a decrease in the overall airframe sound pressure level (OASPL) at the center-line measurement point as thrust cutback altitude is increased. It will be noted that airframe OASPL is approximately 5 dB greater than the center-line engine EPNL. Since OASPL is an instantaneous sound pressure level rather than a time-weighted value, it should be reduced slightly to correlate with the EPNL; however, the amount of reduction is less than 4 dB. Consequently, the most significant noise source of the study airplane is that of the airframe.

It was determined that at a cutback distance of 5944 m (19 500 ft), the maximum allowable altitude is 515 m (1691 ft), because aircraft acceleration capability is inadequate to attain higher altitudes. To reach this maximum altitude, the required all-engine take-off field length is 2248 m (7375 ft). At cutback, thrust is reduced to provide a climb gradient of 4 percent in accordance with regulations of reference 18. The take-off profile and two measurement points (ref. 18) are shown in figure 60. The lift-off velocity is 287 km/hr (155 knots). At the point-1 measurement station, the velocity is 321 km/hr (173 knots), the lift coefficient is 0.75, and the lift-drag ratio is 19.1.

The variations of EPNL along the runway center line and along the side-line (649 m (0.35 n. mi.) from the center line) are shown in figures 61 and 62, respectively. Figure 61 exhibits an airframe OASPL of 94.8 dB at the 6486-m (3.5-n. mi.) center-line measurement point. Therefore, without engine cutback, engine EPNL would exceed the airframe noise. Contour plots for engine EPNL values of 90 dB and 100 dB at engine cutback are presented in figure 63.

Engine noise during approach.- During approach, the engines operate at idle thrust and have a considerably lower noise level than the airframe. Figure 56 shows the 3° approach profile and the reference 18 measurement point which is located 1853 m (1.0 n. mi.) from the 15.2-m (50.0-ft) threshold point. The aircraft landing weight is 4 704 439 N (1 057 600 lbf) and the landing velocity is 300 km/hr (162 knots). For a 3° approach profile, the altitude at the 1853-m (1.0-n. mi.) point is 112 m (369 ft). These values were employed in the airframe noise calculations.

Airframe noise.- The airframe OASPL of the study aircraft was computed by averaging the values generated by the methods of references 21 and 22. The input values and the corresponding OASPL values from each method at the two runway center-line measurement points are presented in table IX. As shown, the values of airframe OASPL at the measurement points during take-off and approach are 94.78 dB and 104.77 dB, respectively. However, these values may be conservative since they are based on the geometric aspect ratio of 4.53 rather than on the effective aspect ratio of approximately 7.9.

DIRECT OPERATING COST

The variation of the study airplane unit cost with the number of airplanes produced is shown in figure 64 based on 1977 dollars. These costs were calculated by use of the method of reference 24.

Figure 65 presents the variation of productivity with fleet size, a utilization rate of 3500 hours per year, a load factor of 0.65, and a range of 5426 km (3200 n. mi.) being assumed. According to reference 25, the 1976 airfreight traffic for the International Civil Aviation Organization airlines - excluding the Soviet Union and China - was approximately 13.4 billion revenue ton miles. Although the cargo traffic handled by these airlines has increased at an average annual rate of about 15 percent since 1960, various surveys forecast a future growth rate ranging from roughly 6 to 12 percent annually for the period into the 1990's. If a 9-percent growth rate is assumed, traffic volume in 1995 would be approximately 116×10^9 Mg-km. However, it is expected that most of this cargo would continue to be carried by conventional freighters and within the belly holds of passenger aircraft. Hence, it would appear that there might be a market for a fleet of roughly 100 span-distributed load aircraft.

The effect of range on direct operating cost (DOC) is shown in figure 66 for several fleet sizes and load factors. These data were generated by using the standard Air Transport Association method of reference 26 with adjustments to reflect 1977 costs. For all cases shown, the effects of range on DOC are small.

Figure 67 shows the effects of fleet size and fuel price on DOC for load factors of 1.00 and 0.65. For the lower range of fleet size, which appears to meet future market requirements, DOC is very sensitive to the number of aircraft produced. Also, DOC is highly dependent on fuel price, which is extremely unpredictable for the operational period of the study airplane. A comparison of the data with those of a current freighter of slightly less design range indicates that for the anticipated fleet size, the study airplane has lower DOC, the difference increasing as load factor decreases and fuel price increases. Since the study airplane utilizes scaled versions of a currently produced engine, it is expected that anticipated advancements in engine design would afford a further improvement in the DOC of the distributed load airplane. However, it should be kept in mine that for the operational time period considered, advancements in technology may provide an improvement in the DOC of future conventional freighter designs to the extent that their efficiency may be comparable with that of the distributed-load airplane.

Lastly, it should also be realized that the requirement for exceptionally wide runways may lead to a very small initial production rate, and thus greatly increases the financial burden of the airframe manufacturer.

CONCLUSIONS

A preliminary study has been conducted of a large span-distributed load cargo aircraft capable of transporting a 2 668 933 N (600 000 lbf) payload of containerized cargo over intercontinental distances. The conclusions are as follows:

1. The specifications for payload weight, density, and dimensions in essence configure the wing, and establish unusually low values of wing loading and aspect ratio.

2. The structural weight comprises only about 18 percent of the design maximum gross weight and exemplifes the magnitude of structural efficiency achievable through the utilization of the span-distributed loading concept.

3. Although the geometric aspect ratio is 4.53, it is estimated that the winglet effect of the wing-tip-mounted vertical tails increases the effective aspect ratio to approximately 7.9.

4. A lift-drag ratio of nearly 19 is attained during cruise.

5. Trim drag in cruise is negated by controlling the center of gravity by fuel management.

6. A hardened stability augmentation system (HSAS) is required. Controls-fixed longitudinal dynamic analyses for the take-off and approach modes indicate that utilization of a current HSAS imposes restrictions on the rearward center-of-gravity travel which preclude the use of optimum elevon settings. Therefore, efficient operation of the aircraft in these flight modes would require the development of a faster reacting control system.

7. Sufficient control power to handle the large rolling moment of inertia dictates a relatively high minimum approach velocity of 315 km/hr (170 knots).

8. The airplane has acceptable spiral, Dutch roll, and roll-damping modes.

9. Because of the relatively low wing loading, engine size is determined by cruise ceiling rather than by take-off field length.

10. The most significant noise source is that of the airframe. However, for both take-off and approach the levels are below the limit (108 dB) of Federal Air Regulations, Part 36.

11. The design mission fuel efficiency is approximately 50 percent greater than that of the most advanced, currently operational, large freighter aircraft.

12. The direct operating cost is significantly lower than that of current freighters with the advantage increasing as fuel price increases.

Langley Research Center
National Aeronautics and Space Administration
Hampton, VA 23665
February 24, 1978

REFERENCES

1. Whitlow, David H.; and Whitener, P. C.: Technical and Economic Assessment of Span-Distributed Loading Cargo Aircraft Concepts. NASA CR-144963, 1976.

2. Technical and Economic Assessment of Span-Loaded Cargo Aircraft Concepts. NASA CR-144952, 1976.

3. Johnston, William M.; Muehlbauer, John C.; Budaily, Roy R.; Farmer, Ben T.; Honrath, John F.; and Thompson, Sterling G.: Technical and Economic Assessment of Span-Distributed Loading Cargo Aircraft Concepts. NASA CR-145034, 1976.

4. Whitehead, Allen H., Jr.: The Promise of Air Cargo - System Aspects and Vehicle Design. NASA TM X-71981, 1976.

5. Bauer, F.; Garabedian, P.; Korn, D.; and Jameson, A.: Supercritical Wing Sections II - A Handbook. Volume 108 of Lecture Notes in Economics and Mathematical Systems, Springer-Verlag, 1975.

6. Whitcomb, Richard T.: A Design Approach and Selected Wind-Tunnel Results at High Subsonic Speeds for Wing-Tip Mounted Winglets. NASA TN D-8260, 1976.

7. McGhee, Robert J.; and Beasley, William D.: Low-Speed Aerodynamic Characteristics of a 17-Percent-Thick Airfoil Section Designed for General Aviation Applications. NASA TN D-7428, 1973.

8. Bruhn, E. F.: Analysis and Design of Airplane Structures. Tri-State Offset Co. (Cincinnati, Ohio), c.1949. (Revised, Jan. 1952.)

9. Goldhammer, M. I.: A Lifting Surface Theory for the Analysis of Nonplanar Lifting Systems. AIAA Paper No. 76-16, Jan. 1976.

10. Woodward, F. A.: An Improved Method for the Aerodynamic Analysis of Wing-Body-Tail Configurations in Subsonic and Supersonic Flow. NASA CR-2228, pts. I-II, 1973.
    Part I - Theory and Application.
    Part II - Computer Program Description.

11. Putnam, Lawrence E.: An Analytical Study of the Effects of Jets Located More Than One Jet Diameter Above a Wing at Subsonic Speeds. NASA TN D-7754, 1974.

12. Abbott, Ira H.; and Von Doenhoff, Albert E.: Theory of Wing Sections, Dover Publ. Inc., c.1959.

13. USAF Stability and Control Datcom. Contracts AF 33(616)-6460 and F33615-74-C-3021, McDonnell Douglas Corp., Oct. 1960. (Revised Jan. 1975.)

14. Flying Qualities of Piloted Airplanes. Mil. Specif. MIL-F-8785B(ASG), Aug. 7, 1969.

15. JT9D Commercial Turbofan Engine Installation Handbook. Marketing Support. Pratt & Whitney Aircraft, United Technologies, Mar. 1967. (Revised Aug. 1975.)

16. General Electric Co.: Propulsion System Studies for an Advanced High Subsonic, Long Range Jet Commercial Transport Aircraft. NASA CR-121016, 1972.

17. Anderson, B. A.: Scaling the JT9D Engine. TDM-1990 Revised, Pratt & Whitney Aircraft, United Aircraft Corp., Apr. 1968.

18. Noise Standards: Aircraft Type and Airworthiness Certification. Federal Aviation Regulations, pt. 36, FAA, June 1974.

19. Heidmann, M. F.: Interim Prediction for Fan and Compressor Source Noise. NASA TM X-71763, 1975.

20. Stone, James R.: Interim Prediction Method for Jet Noise. NASA TM X-71618, 1974.

21. Hardin, Jay C.; Fratello, David J.; Hayden, Richard E.; Kadman, Yoran; and Africk, Steven: Prediction of Airframe Noise. NASA TN D-7821, 1975.

22. Baber, Hal T.; and Swanson, E. E.: Advanced Supersonic Technology Concept AST-100 Characteristics Developed in a Baseline-Update Study. NASA TM X-72815, 1976.

23. Advanced Supersonic Technology Concept Study Reference Characteristics. NASA CR-132374, 1973.

24. Oman, B. H.: Vehicle Design Evaluation Program. NASA CR-145070, 1977.

25. Aerospace Industries Association of America, Inc.: Aerospace Facts and Figures, 1975/76. Aviation Week & Space Technol., [1975].

26. Standard Method of Estimating Comparative Direct Operating Costs of Turbine Powered Transport Airplanes. Air Transp. Assoc. of America, Dec. 1976.

TABLE I.- GROUP WEIGHT SUMMARY

	Weight	
	N	**lbf**
Structures:		
Wing	690 244	155 173
Vertical tails	33 949	7 632
Fuselage	18 727	4 210
Landing gear	289 023	64 975
Nacelles	46 813	10 524
Total, structures	1 078 756	242 514
Propulsion:		
Engines	317 674	71 416
Thrust reversers	45 470	10 222
Miscellaneous systems	9 421	2 118
Fuel system, tanks, and plumbing	53 290	11 980
Total, propulsion	425 855	95 736
Systems and equipment:		
Surface controls	74 730	16 800
Auxiliary power	4 270	960
Instruments	9 946	2 236
Hydraulics	39 767	8 940
Electrical	39 086	8 787
Avionics	10 040	2 257
Furnishings and equipment	8 719	1 960
Air conditioning	890	200
Anti-icing	934	210
Total, systems and equipment	188 382	42 350
Weight, empty	1 692 993	380 600
Crew and baggage (4)	4 003	900
Unusable fuel	18 238	4 100
Engine oil	4 337	975
Passenger service	111	25
Operating weight, empty	1 719 682	386 600
Containerized cargo, gross	2 668 933	600 000
Zero-fuel weight	4 388 615	986 600
Mission fuel	1 663 635	374 000
Design take-off gross weight	6 052 250	1 360 600

TABLE II.- MASS DATA SUMMARY

	Design take-off			Reserve fuel	
Gross weight, N (lbf)	6 052 250 (1 360 600)			4 704 439 (1 057 600)	
Flight mode	Cruise	Landing	Take-off	Cruise	Landing
Longitudinal location of center of gravity, m	29.8	30.1	30.1	29.8	30.3
(ft)	(97.7)	(98.6)	(98.9)	(97.7)	(99.5)
percent $\bar{c}$	29.0	30.4	30.9	29.0	31.8
Roll inertia, I_X, kg-m^2	315×10^6	316×10^6	318×10^6	284×10^6	285×10^6
(slug-ft^2)	(232×10^6)	(233×10^6)	(234×10^6)	(209×10^6)	(210×10^6)
Pitch inertia, I_Y, kg-m^2	50×10^6	49×10^6	49×10^6	53×10^6	48×10^6
(slug-ft^2)	(37×10^6)	(36×10^6)	(36×10^6)	(39×10^6)	(35×10^6)
Yaw inertia, I_Z, kg-m^2	352×10^6	350×10^6	349×10^6	320×10^6	314×10^6
(slug-ft^2)	(259×10^6)	(258×10^6)	(257×10^6)	(236×10^6)	(231×10^6)
Product of inertia, I_{XZ}, kg-m^2	1.6×10^6	1.5×10^6	1.1×10^6	0.9×10^6	1.2×10^6
(slug-ft^2)	(1.2×10^6)	(1.1×10^6)	(0.8×10^6)	(0.7×10^6)	(0.9×10^6)
Principal axis inclination, rad	-0.044	-0.041	-0.039	-0.025	-0.044
(deg)	(-2.52)	(-2.35)	(-2.23)	(-1.43)	(-2.52)

29.

TABLE III.- FUEL DISTRIBUTION

Point (a)	Center of gravity, percent $\bar{c}$	Design gross weight, N (lb)	Total fuel, N (lb)	Fuselage tank, N (lb)	Wing forward tanks, N (lb)	Wing aft tanks, N (lb)
1	15.0	6 052 250 (1 360 600)	1 663 635 (374 000)	315 824 (71 000)	1 347 811 (303 000)	0 (0)
2	29.0	6 052 250 (1 360 600)	1 663 635 (374 000)	0 (0)	606 737 (136 400)	1 056 898 (237 600)
3	30.4	6 052 250 (1 360 600)	1 663 635 (374 000)	0 (0)	476 707 (107 168)	1 186 928 (266 832)
4	30.9	6 052 250 (1 360 000)	1 663 635 (374 000)	0 (0)	430 268 (96 728)	1 233 367 (277 272)
5	35.5	6 052 250 (1 360 000)	1 663 635 (374 000)	0 (0)	0 (0)	1 663 635 (374 000)
6	29.0	4 704 439 (1 057 600)	315 824 (71 000)	315 824 (71 000)	0 (0)	0 (0)
7	5.6	3 383 317 (760 600)	1 663 635 (374 000)	315 824 (71 000)	1 347 811 (303 000)	0 (0)
8	37.4	3 383 317 (760 600)	1 663 635 (374 000)	0 (0)	0 (0)	1 663 635 (374 000)
9	23.0	2 035 506 (457 600)	315 824 (71 000)	315 824 (71 000)	0 (0)	0 (0)

[a]See figure 17 for correlation of point number.

30.

TABLE IV.- LATERAL-DIRECTIONAL DYNAMIC CHARACTERISTICS

	Stability mode				
	Dutch roll			Roll	Spiral
	ζ_{min}	$(\zeta\omega_n)_{min}$, rad/sec	$\omega_{n,min}$, rad/sec	t_{max}, sec	$t_{2,min}$, sec
Requirements	0.080	0.150	0.400	1.400	20.0
Inherent characteristics:					
MLW	0.285	0.168	0.590	1.367	[a]-40.6
RLW	0.301	0.171	0.570	1.302	[a]-42.3

[a]Negative sign denotes time to half amplitude of oscillation (spirally stable).

TABLE V.- ENGINE NACELLE DIMENSIONS
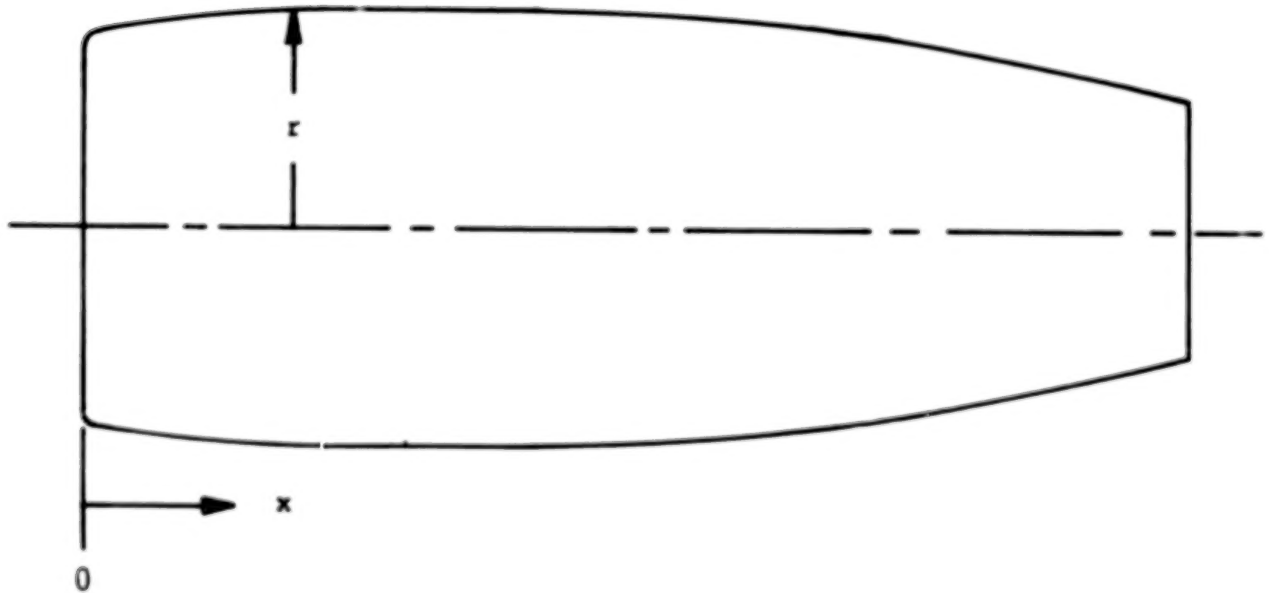
x		r		x		r	
m	in.	m	in.	m	in.	m	in.
0.000	0	1.267	49.9	4.521	178	1.585	62.4
.025	1	1.311	51.6	5.080	200	1.577	62.1
.127	5	1.367	53.8	5.588	220	1.557	61.3
.254	10	1.415	55.7	6.096	240	1.519	59.8
.508	20	1.478	58.2	6.604	260	1.466	57.7
.762	30	1.514	59.6	7.112	280	1.405	55.3
1.016	40	1.539	60.6	7.620	300	1.328	52.3
1.524	60	1.567	61.7	8.128	320	1.224	48.2
2.032	80	1.580	62.2	8.509	335	1.113	43.8
2.769	109	1.585	62.4	8.738	344	1.016	40.0

TABLE VI.- MISSION PERFORMANCE

[Taxi-in fuel taken out of reserves at destination.
Civil Aeronautics Board range equals trip range
minus allowances for maneuver, traffic, and
airway distance]

(a) Aircraft characteristics

Take-off gross weight, N (lbf)	6 052 250	(1 360 600)
Operating weight, empty, N (lbf)	1 719 682	(386 600)
Payload, gross, N (lbf)	2 668 933	(600 000)
Wing area, m^2 (ft^2)	1 724	(18 560)
Sea-level static thrust, per engine, standard day:		
Uninstalled, N (lbf)	262 445	(59 000)
Installed, N (lbf)	240 204	(54 000)
Take-off thrust-weight ratio		0.238
Take-off wing loading, N/m^2 (lbf/ft^2)	3509.62	(73.3)

(b) Design mission

Flight mode	Gross weight, N (lbf)	ΔFuel, N (lbf)	ΔRange, km (n. mi.)	ΔTime, min
Take-off	6 052 250 (1 360 600)			
		24 910 (5 600)	0	11
Start climb . . .	6 027 340 (1 355 000)			
		157 111 (35 320)	370 (200)	31
Start cruise . . .	5 870 229 (1 319 680)			
		1 143 193 (257 000)	5213 (2815)	387
End cruise	4 727 036 (1 062 680)			
		22 464 (5 050)	370 (200)	20
End descent	4 704 573 (1 057 630)			
		22 464 (5 050)		
Taxi-in	4 696 566 (1 055 830)	8 007 (1 800)	0	5
Block fuel and time	1 355 684 (304 770)		454
Trip range	5953 (3215)		

(c) Reserve fuel breakdown

10-percent trip time, N (lbf)	114 319	(25 700)
Missed approach, N (lbf)	17 793	(4 000)
370 km (200 n. mi.) to alternate airport, N (lbf)	116 099	(26 100)
30 minutes holding at 457 m (1500 ft), N (lbf)	67 746	(15 230)
Total reserve fuel	315 957	(71 030)

(d) Initial cruise conditions

C_L	0.333
C_D	0.01782
L/D	18.65
TSFC, kg/N-hr (lbm/lbf-hr)	0.0637 (0.625)
Altitude, m (ft)	10 119 (33 200)

(e) Fuel efficiency

Payload-distance per quantity of fuel burned, Mg-km/N (ton-n. mi./lbf)	1.19 (3.16)

TABLE VII.- INPUT PARAMETERS FOR PREDICTING TAKE-OFF FAN NOISE

```
Diameter,  D, m (ft) . . . . . . . . . . . . . . . . . . . . . 2.643 (8.671)
Fan total temperature rise,  ΔC(ΔF) . . . . . . . . . . . . . 86.06 (154.9)
Mass flow, kg/sec (slugs/sec) . . . . . . . . . . . . . . . 763.35 (52.31)
Number of fan blades . . . . . . . . . . . . . . . . . . . . . . 108
Number of stator vanes . . . . . . . . . . . . . . . . . . . . . 46
Rotor tip Mach number at design . . . . . . . . . . . . . . . . 1.287
Rotor stator spacing ratio . . . . . . . . . . . . . . . . . . . 1.267
Fan rotor speed,  ω, rpm . . . . . . . . . . . . . . . . . . . 2972
Calculated values:
```

Blade passing frequency, $F_b = \dfrac{N_b(\omega)}{60}$, Hz 5350

Rotor tip operating Mach number, $M_{TR} = \dfrac{\pi D \omega}{60 c_a}$ 1.2127

TABLE VIII.- INPUT PARAMETERS FOR PREDICTING TAKE-OFF JET NOISE

```
Primary exit flow characteristics:
  Area, m² (ft²) . . . . . . . . . . . . . . . . . . . . . 0.8393 (9.04)
  Mass flow, kg/sec (slugs/sec) . . . . . . . . . . . . . 157.75 (10.809)
  Velocity, m/sec (ft/sec) . . . . . . . . . . . . . . . 369.65 (1212.75)
  Density,ᵃ kg/m³ (slugs/ft³) . . . . . . . . . . . . . . 0.5102 (0.00099)
```
  Absolute total temperature ratio, $T_{t,jet}/T_{t,a}$ 2.66

```
Fan exit-flow characteristics:
  Area, m² (ft²) . . . . . . . . . . . . . . . . . . . . . 2.3950 (25.78)
  Mass flow, kg/sec (slugs/sec) . . . . . . . . . . . . . 763.48 (52.315)
  Velocity, m/sec (ft/sec) . . . . . . . . . . . . . . . 286.91 (941.32)
  Density,ᵃ kg/m³ (slugs/ft³) . . . . . . . . . . . . . . 1.1132 (0.00216)
```
  Absolute total temperature ratio, $T_{t,jet}/T_{t,a}$ 1.15

```
Aircraft velocity, m/sec (ft/sec) . . . . . . . . . . . . . . . 88.40 (290.03)
```

ᵃDensity is computed by using mass flow, velocity, and jet exit area.

TABLE IX.- AIRFRAME NOISE DURING TAKE-OFF AND APPROACH

(AIRPLANE DIRECTLY OVER MEASUREMENT POINT)

	Take-off (Measurement point 1)	Approach (Measurement point 2)
Aircraft weight, W, N	6 052 250	4 704 439
Wing span, b, m	88.39	88.39
Aspect ratio, A	4.531	4.531
Altitude, h, m	542.90	112.36
Velocity, V, m/sec	89.30	83.39
Wing area, S, m^2	1 724.28	1 724.28
Reference 21 airframe OASPL, dB (eq. (1))	98.38	109.24
Reference 22 airframe OASPL, dB (eq. (2))	91.09	100.27
Study airplane airframe OASPL,[a] dB	94.78	104.77

[a]Study airplane airframe OASPL assumed to be average of equations (1) and (2).

$$OASPL_{airframe} = 10 \log \left[\frac{V^{3.34}(W/9.807)^{0.6}b^{0.63}}{h^{1.83}A^{3.03}} \right] + 56.14 \tag{1}$$

$$OASPL_{airframe} = 10 \log \left[\frac{V^{3.17}(W/9.807)^{0.88}}{h^{1.62}S^{0.16}A^{2.06}} \right] + 41.29 \tag{2}$$
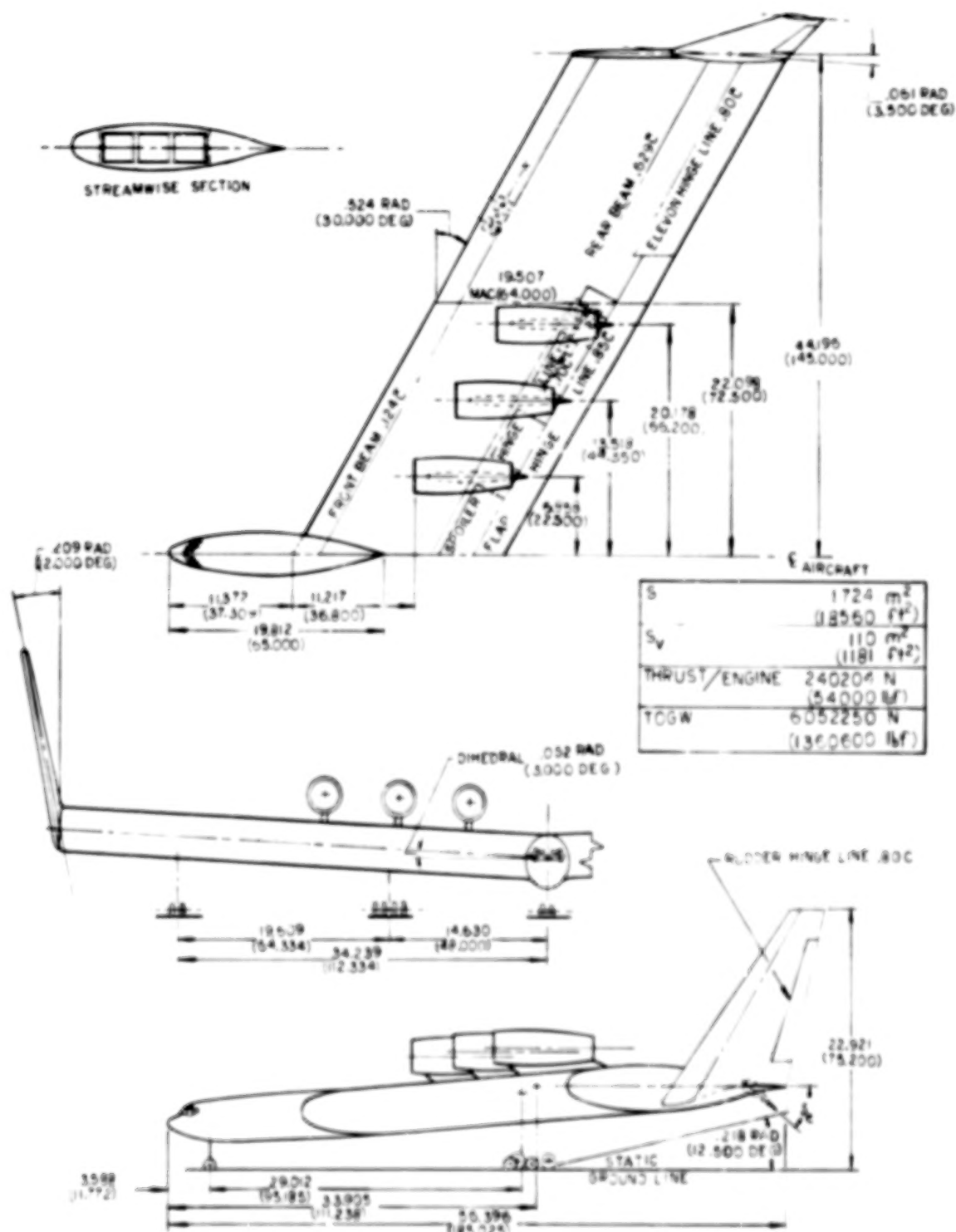
Figure 1.- Span-distributed-load cargo airplane configuration.
Dimensions are shown in meters with feet in parentheses
except as noted.

FUEL TANKS

FRONT BEAM

REAR BEAM
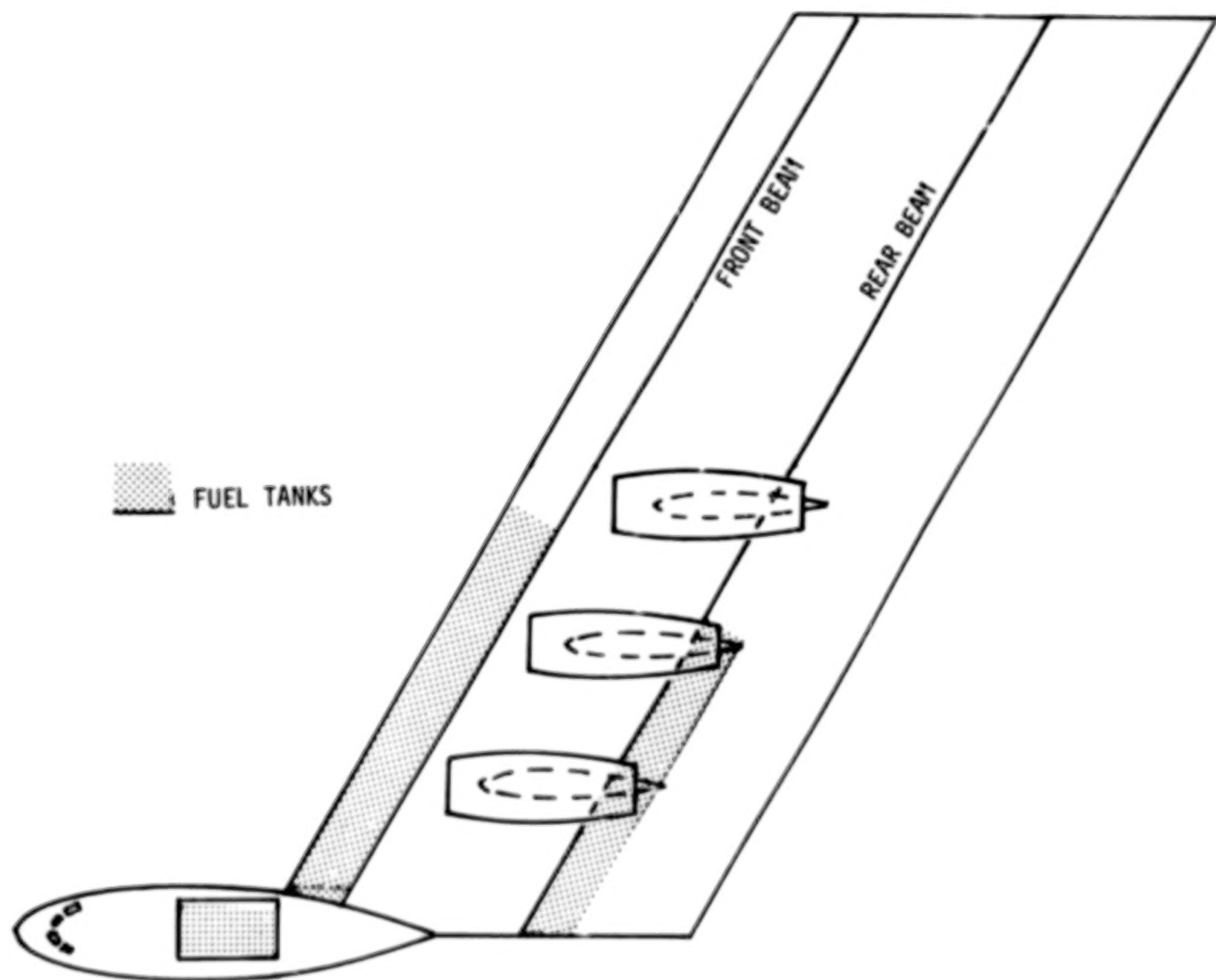
Figure 2.- Schematic of fuel tank locations.

37.

30°
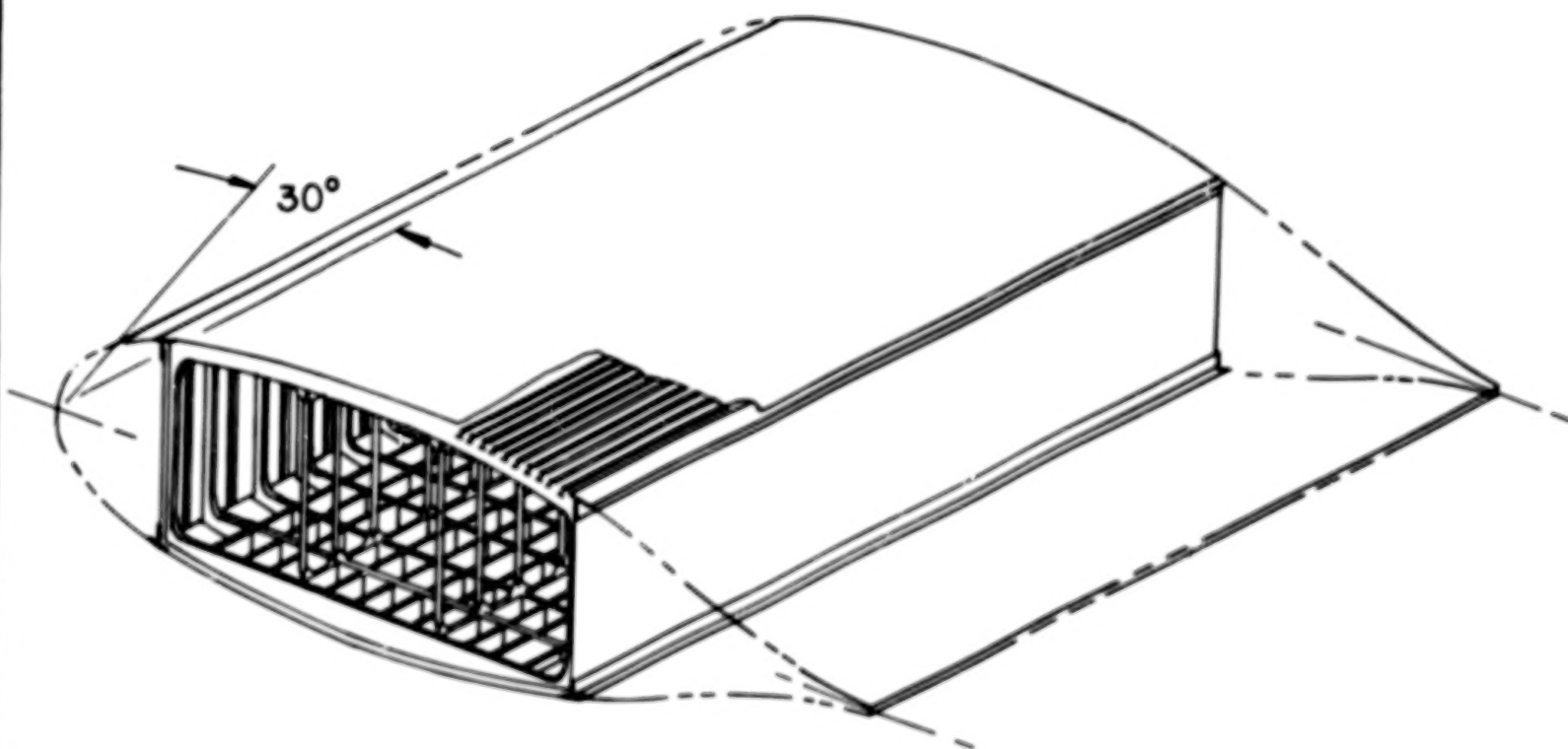
Figure 3.- Schematic of wing-box structural concept.

38.
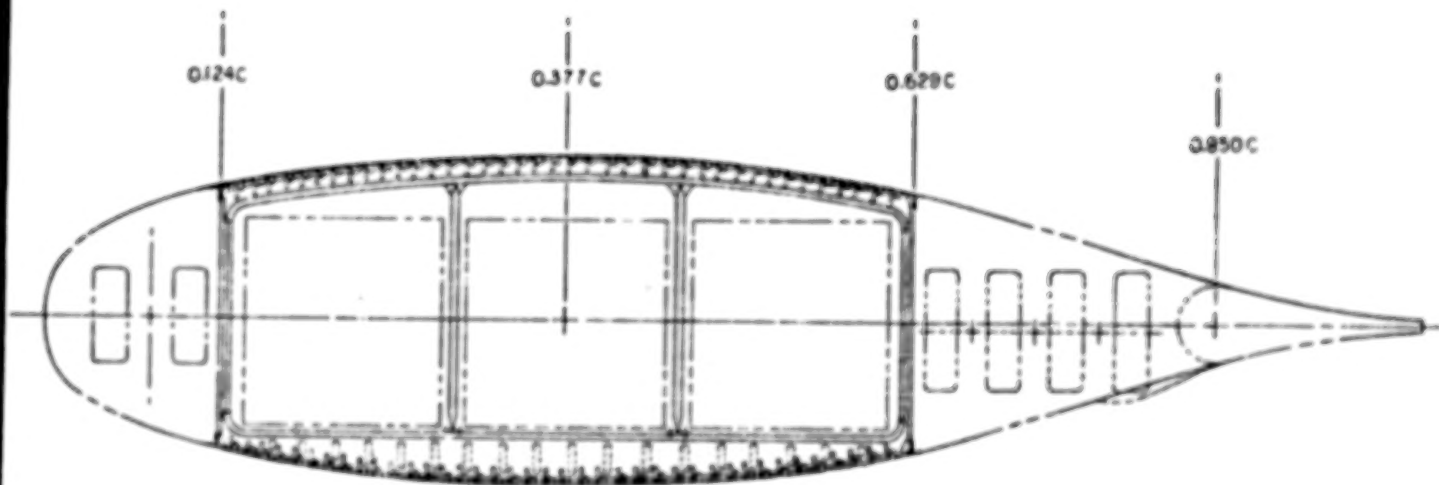
Figure 4.- Cross section of wing normal to leading edge.

39.
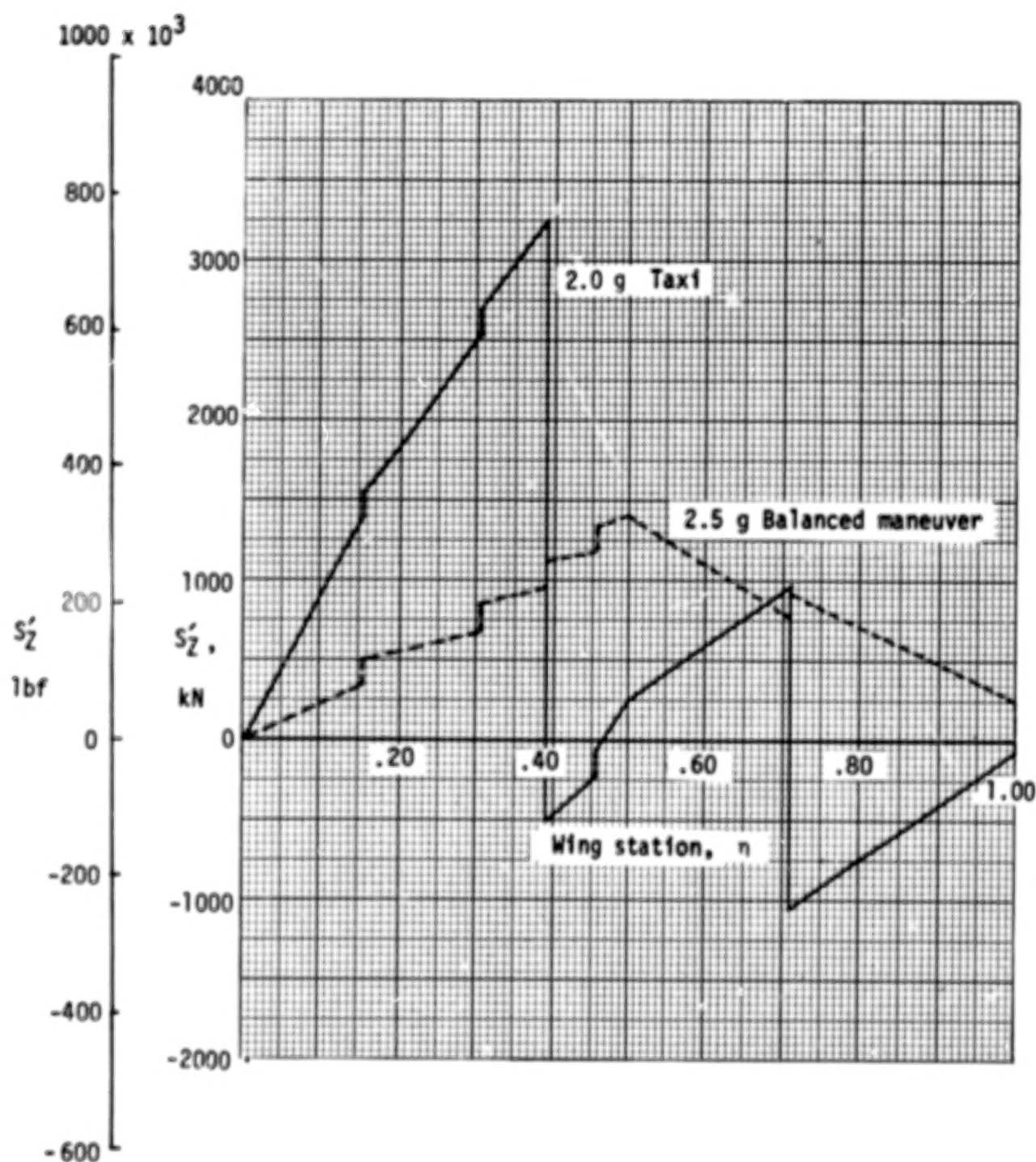
Figure 5.- Net limit swept axis shears.
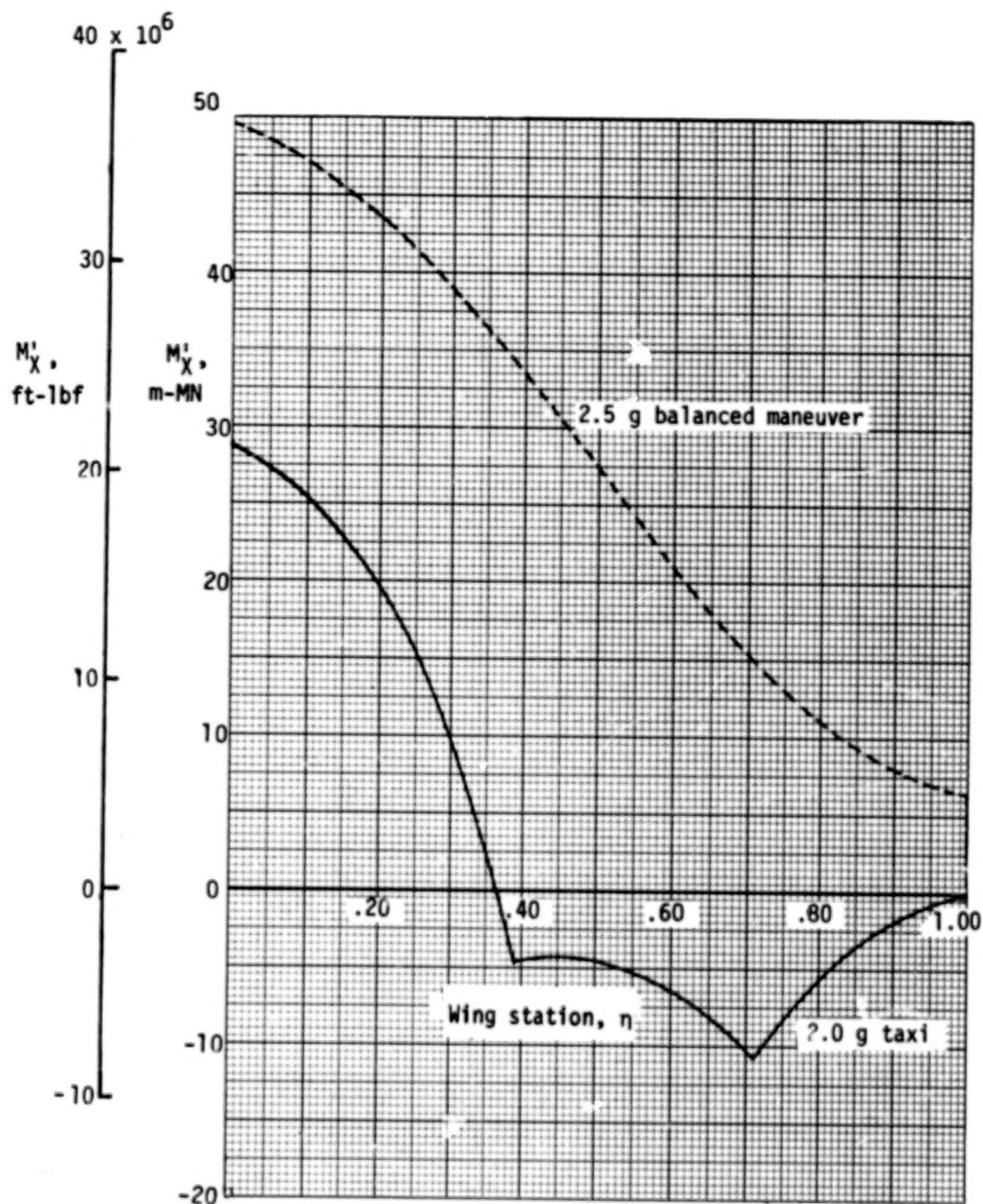
Figure 6.- Net limit swept axis bending moments.
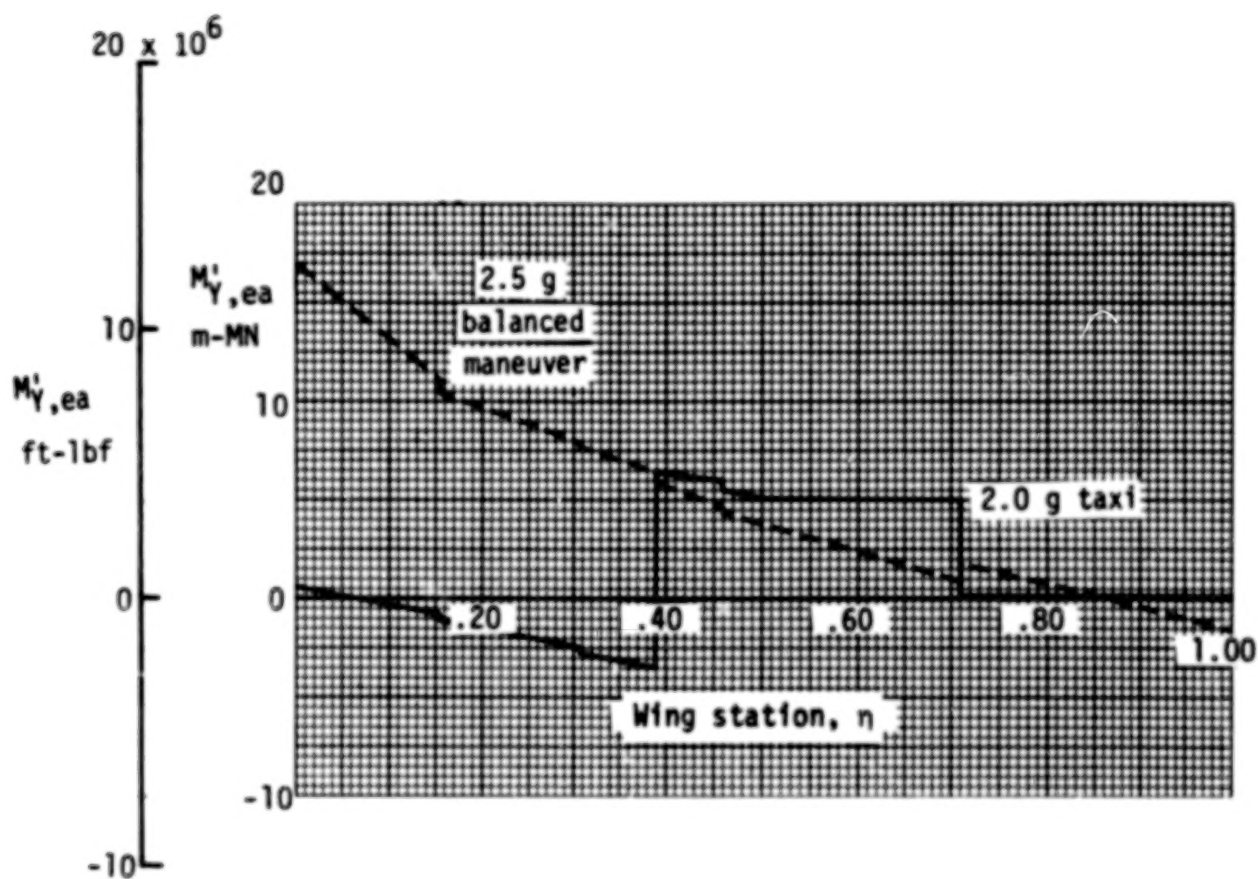
Figure 7.- Net limit swept axis torsions.

Wing station 51.036 m
167.44 ft

Outboard landing
gear position

$\eta = .86$

$\eta = .71$

Aft beam .629 c

Front beam .124 c

$\eta = .43$

$\eta = .39$

$\eta = .37$

$\eta = .26$

Inboard landing
gear position

$\eta = .13$

$\eta = 0$

Wing station 0.00
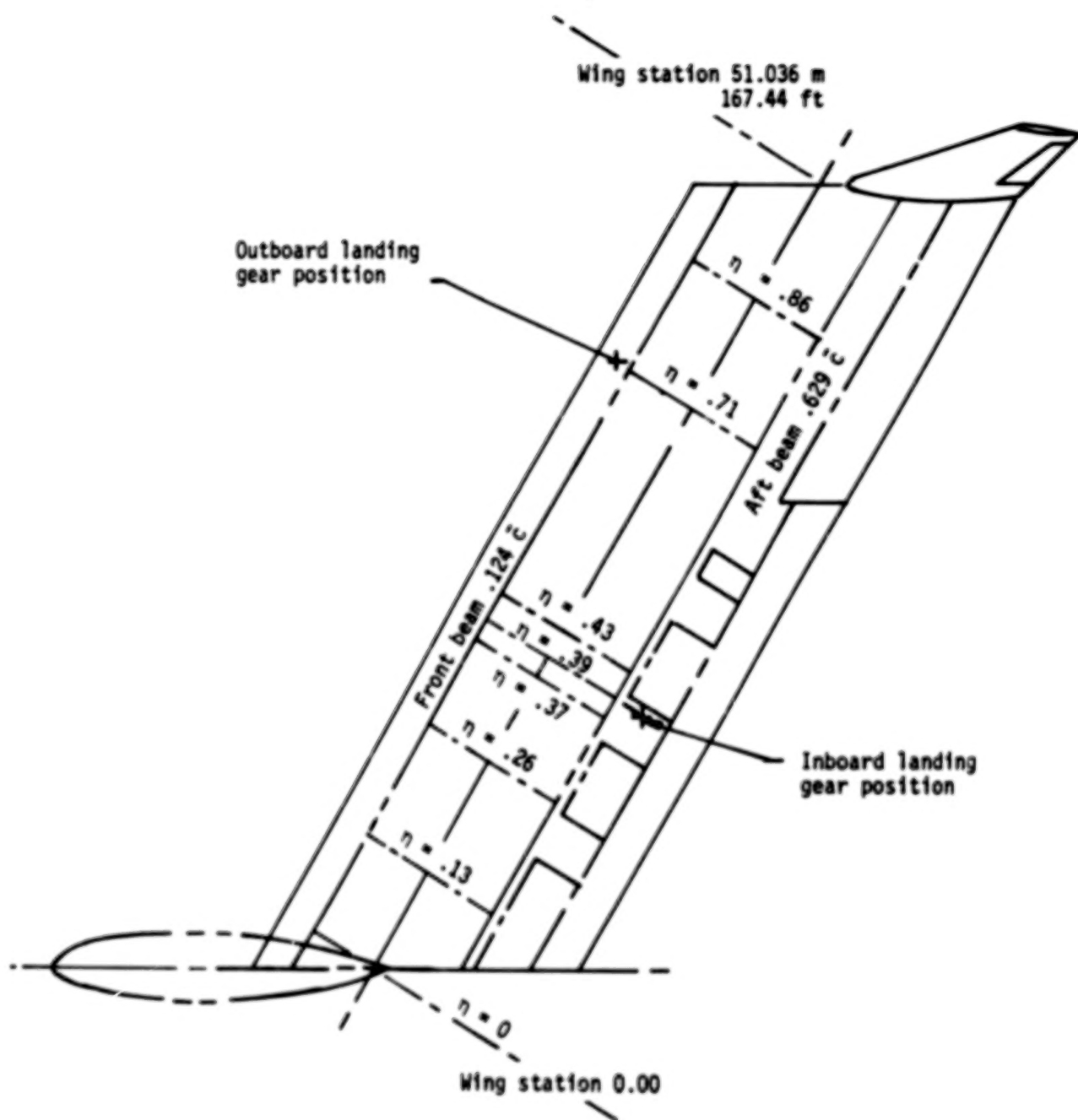
Figure 8.- Semispan stations at which wing-box loads were analyzed.

$q_{web} = q_v + q_s$

$V_{web} = q_{web} (h_{web})$
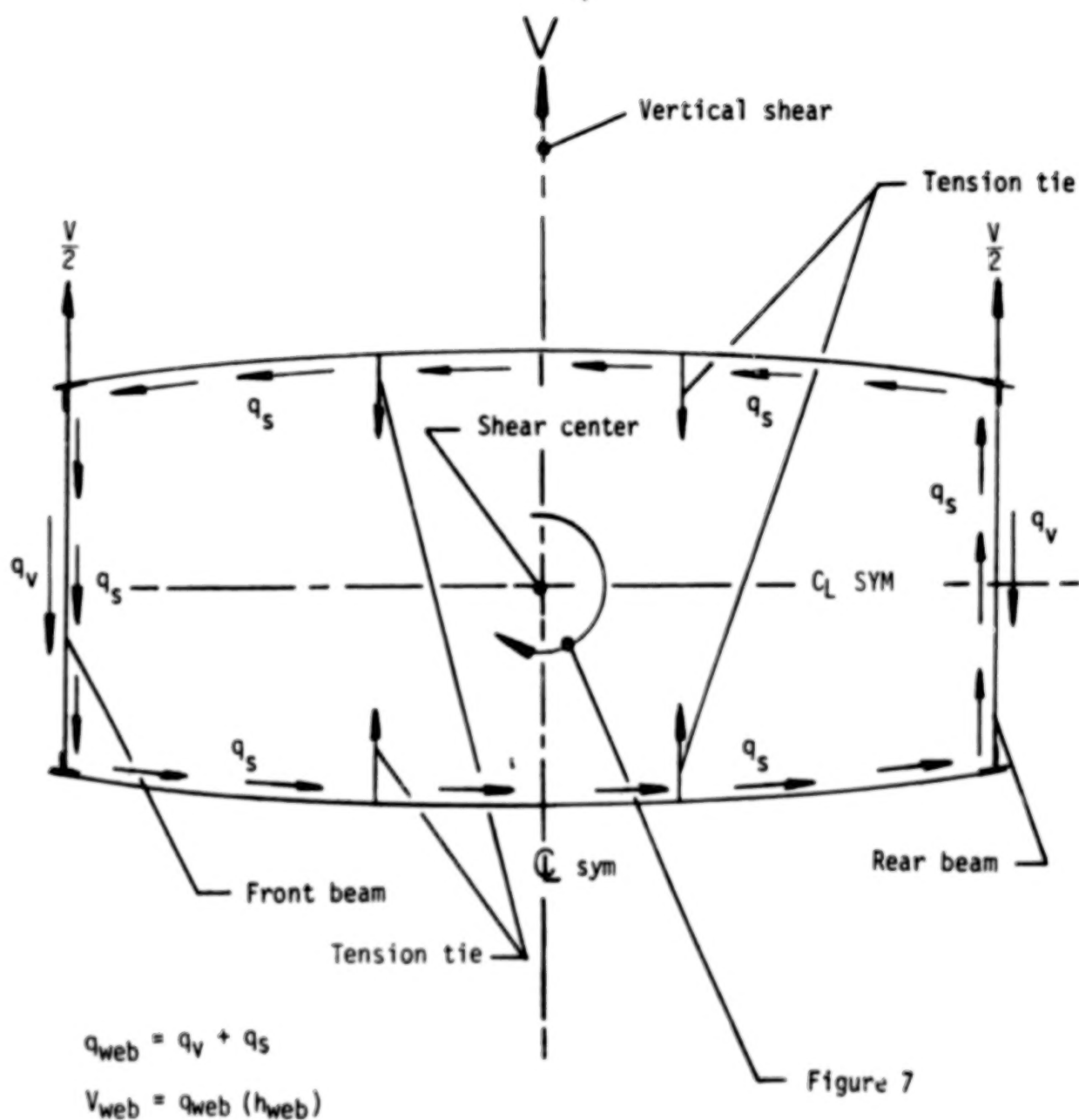
Figure 9.- Shear flow schematic.
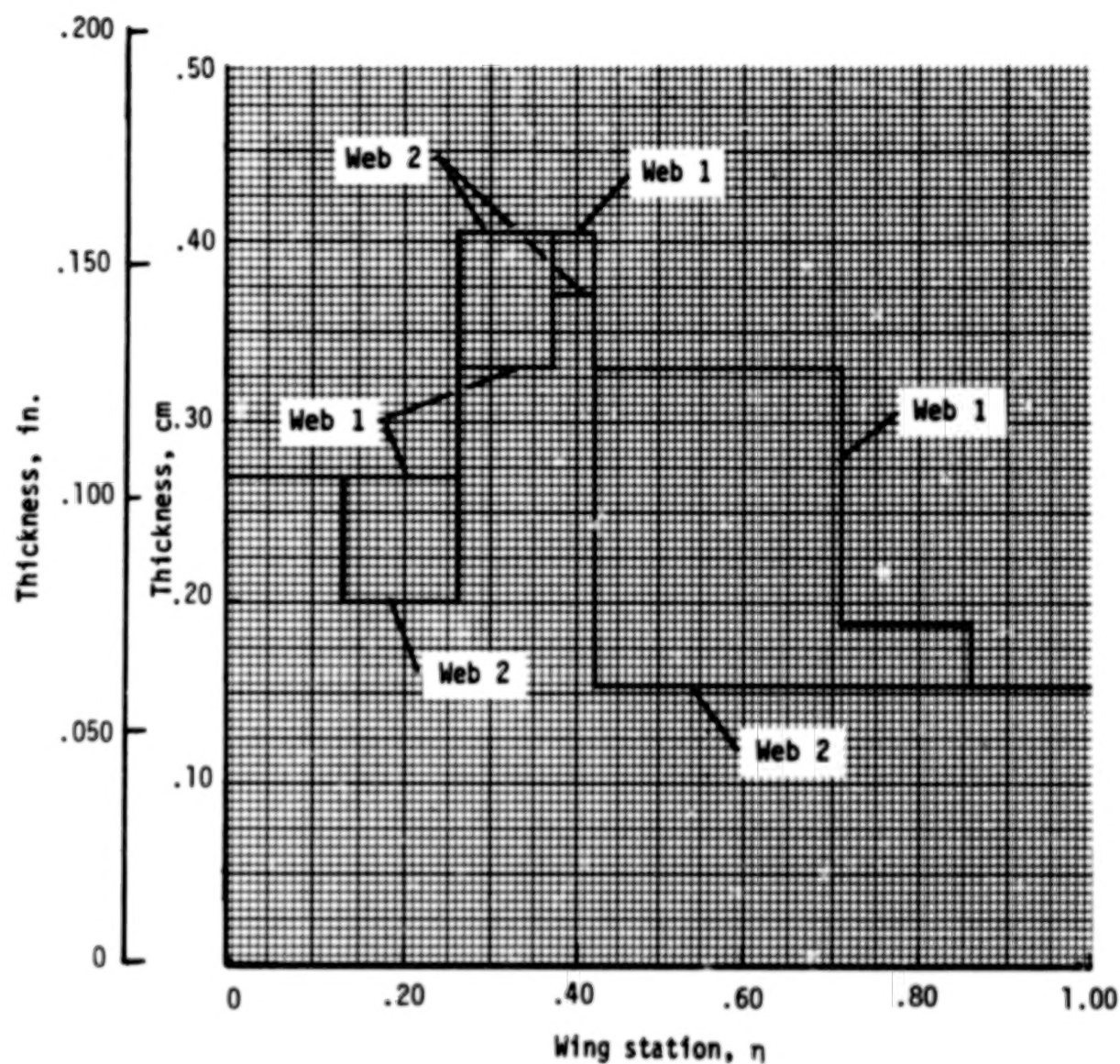
Figure 10.- Web thicknesses of beams 1 (forward) and 2 (rearward).
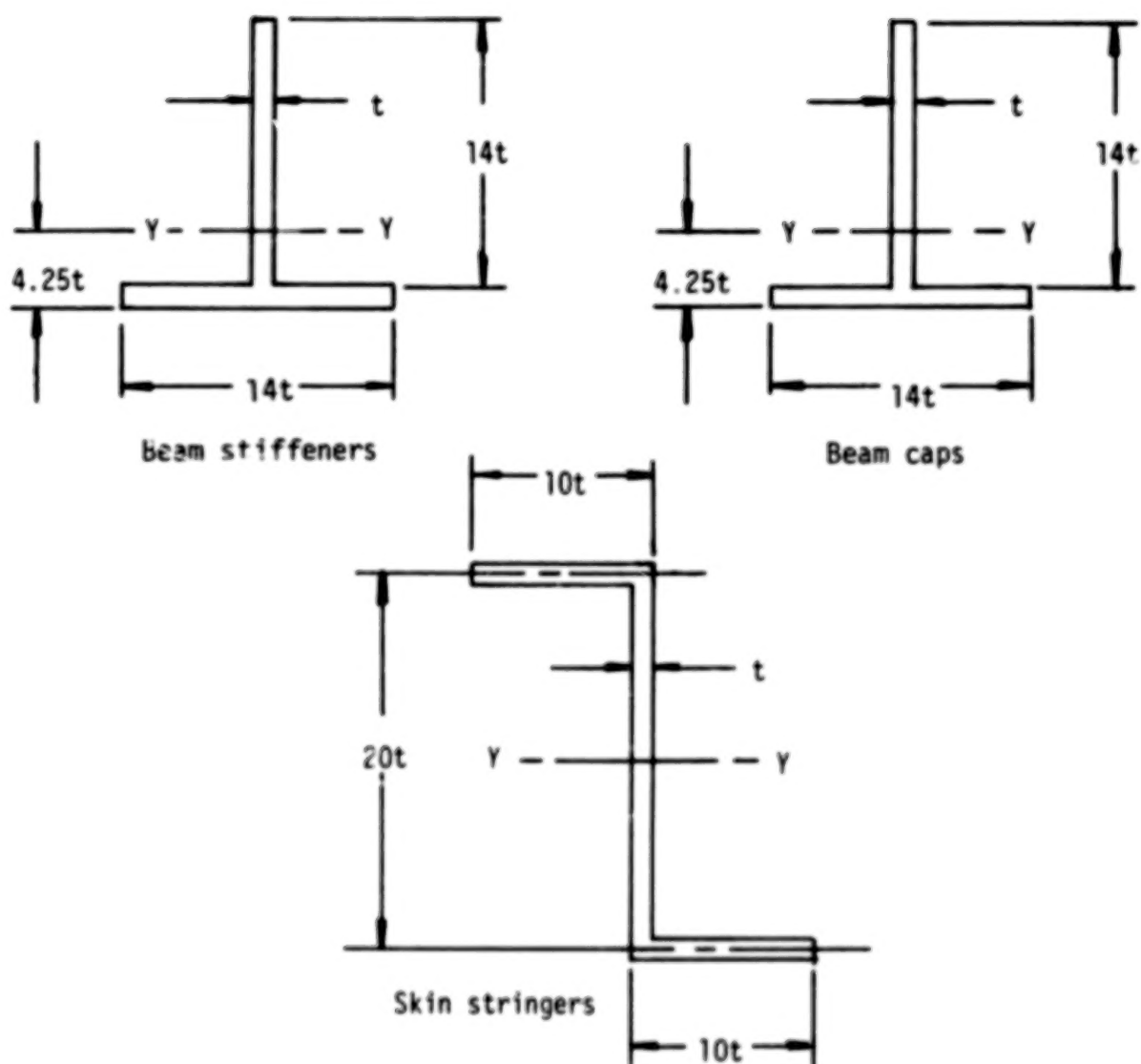
Figure 11.- Cross sections of mean stiffeners, beam caps, and skin stringers.
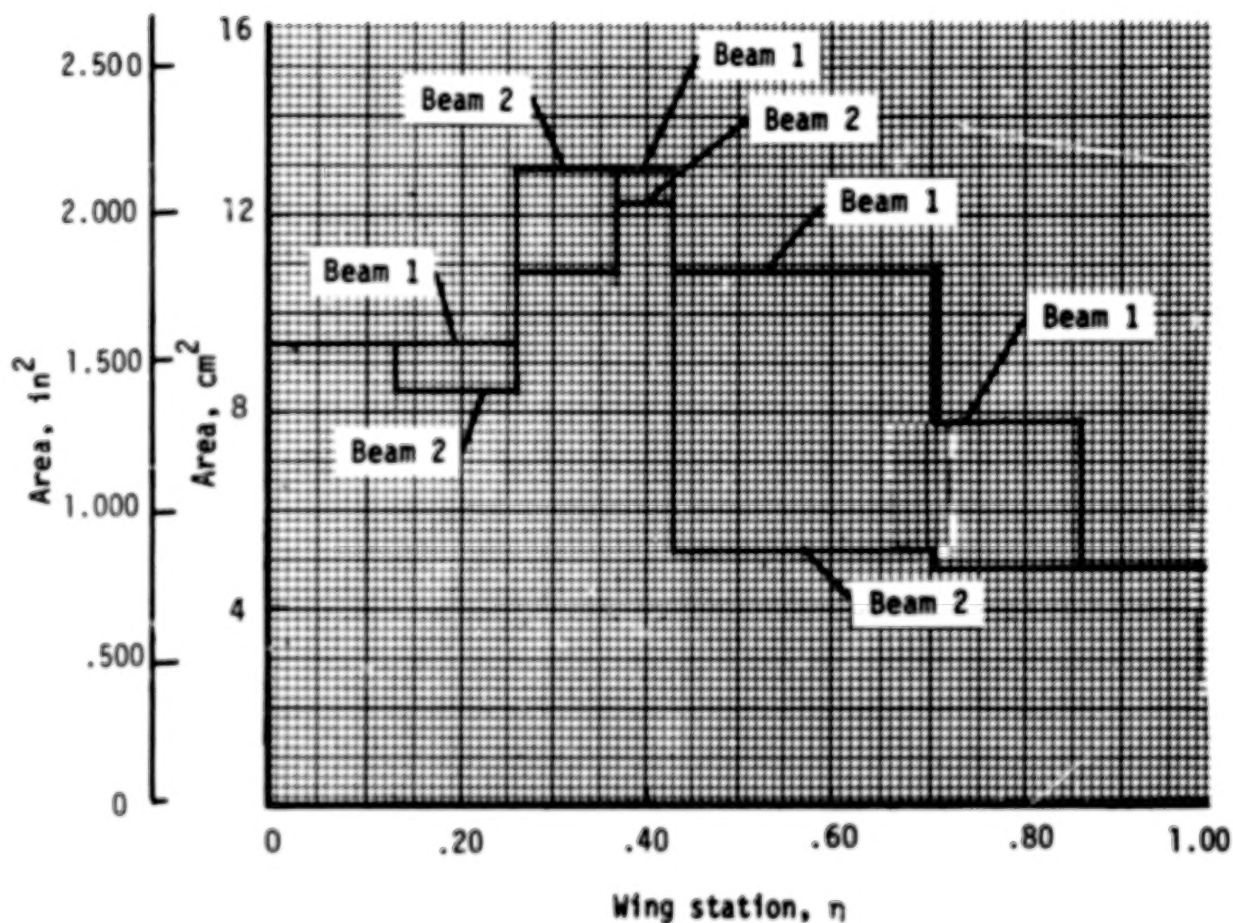
Figure 12.- Stiffener sectional areas of beams 1 (forward) and 2 (rearward).
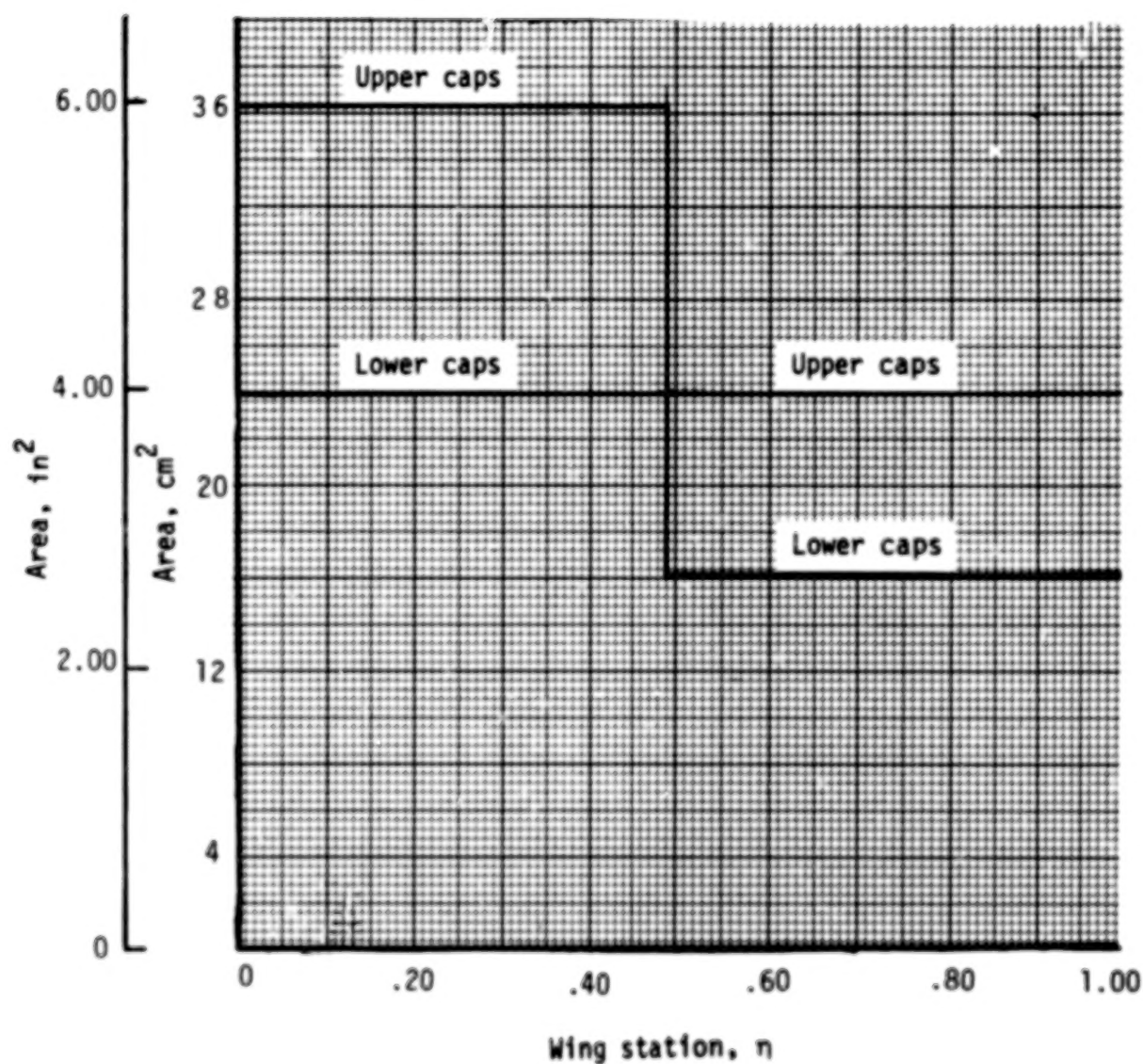
Figure 13.- Upper and lower beam cap sectional areas of beams 1 (forward) and 2 (rearward).
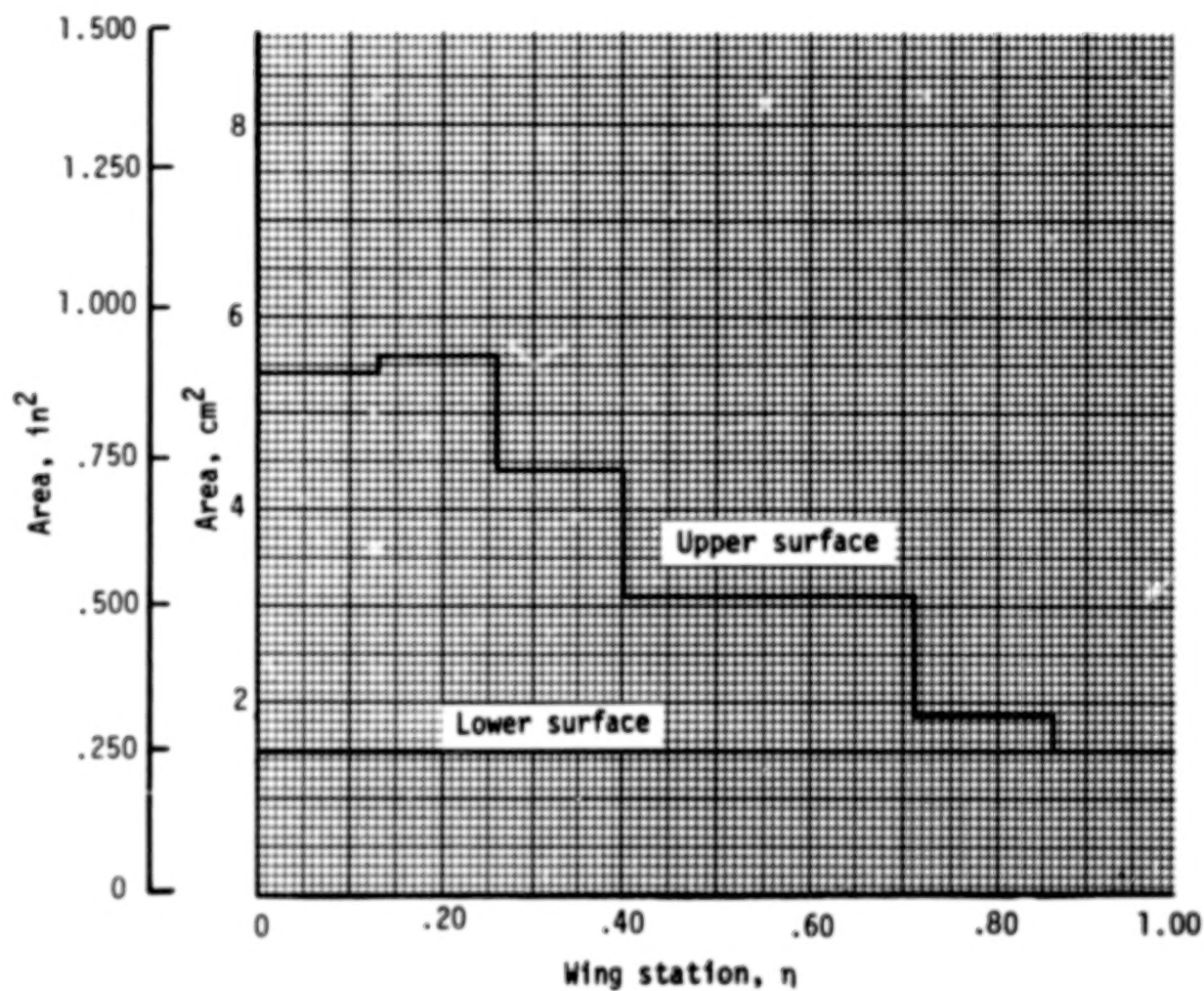
Figure 14.- Wing box stringer sectional areas, upper
and lower surfaces.
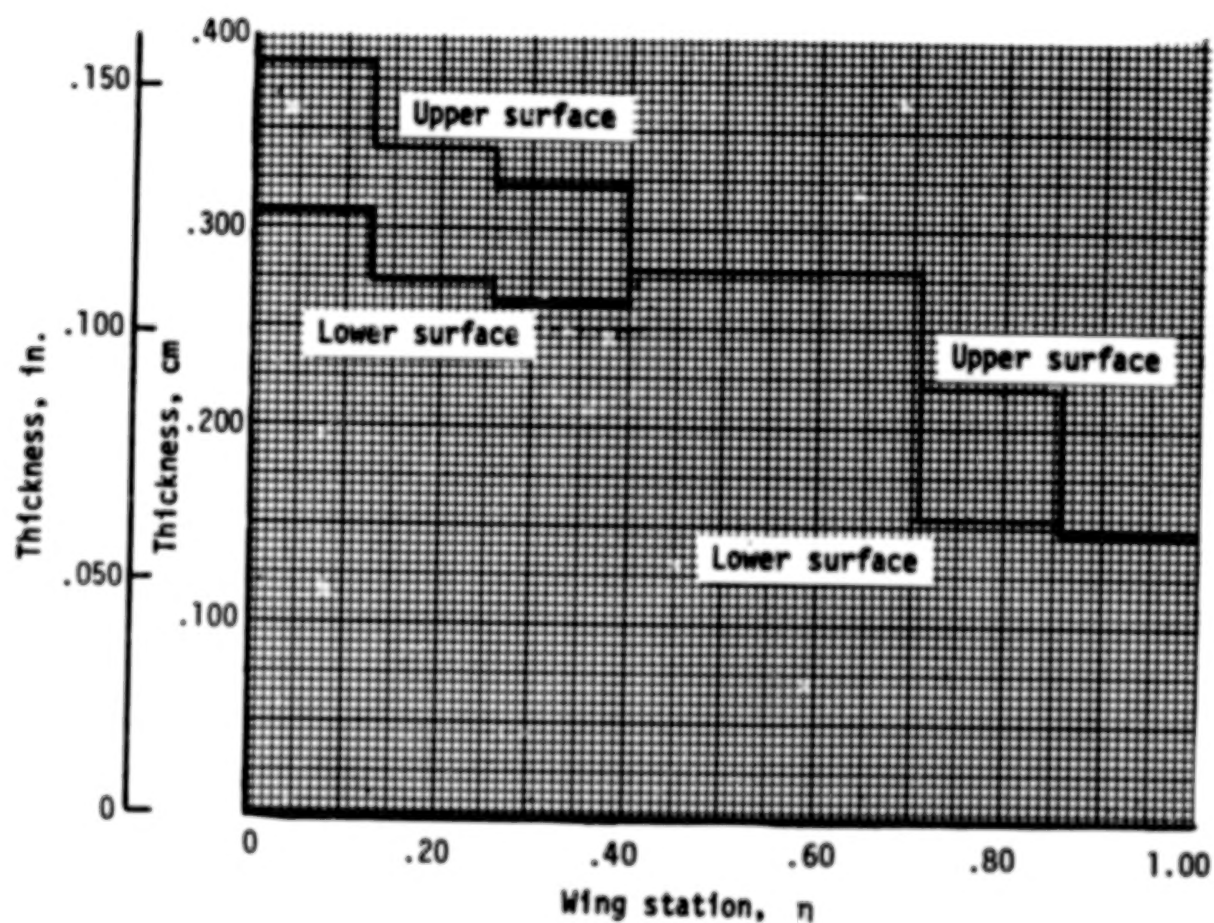
Figure 15.- Wing box skin thickness, upper and lower surfaces.
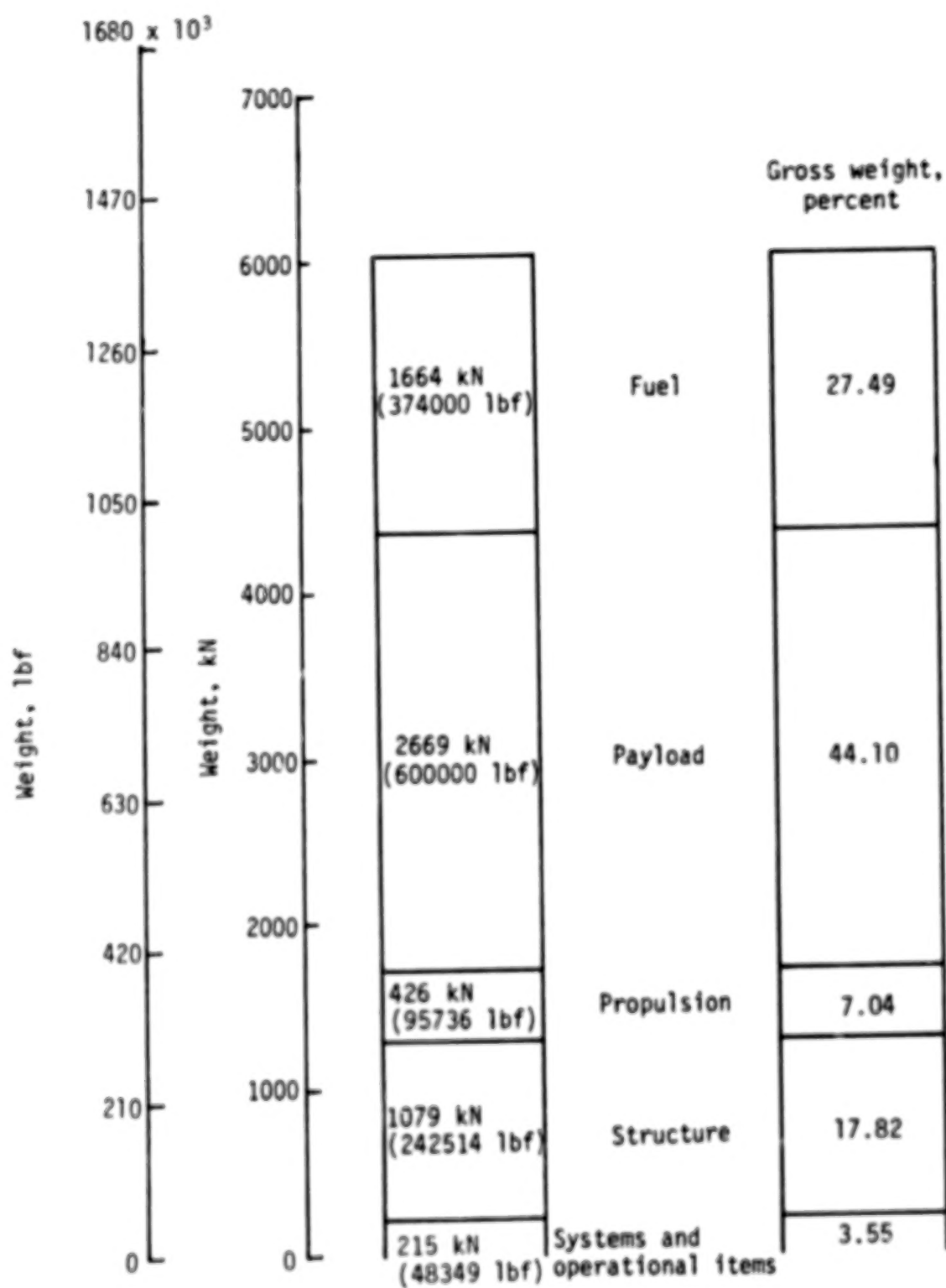
Figure 16.- Gross weight breakdown.
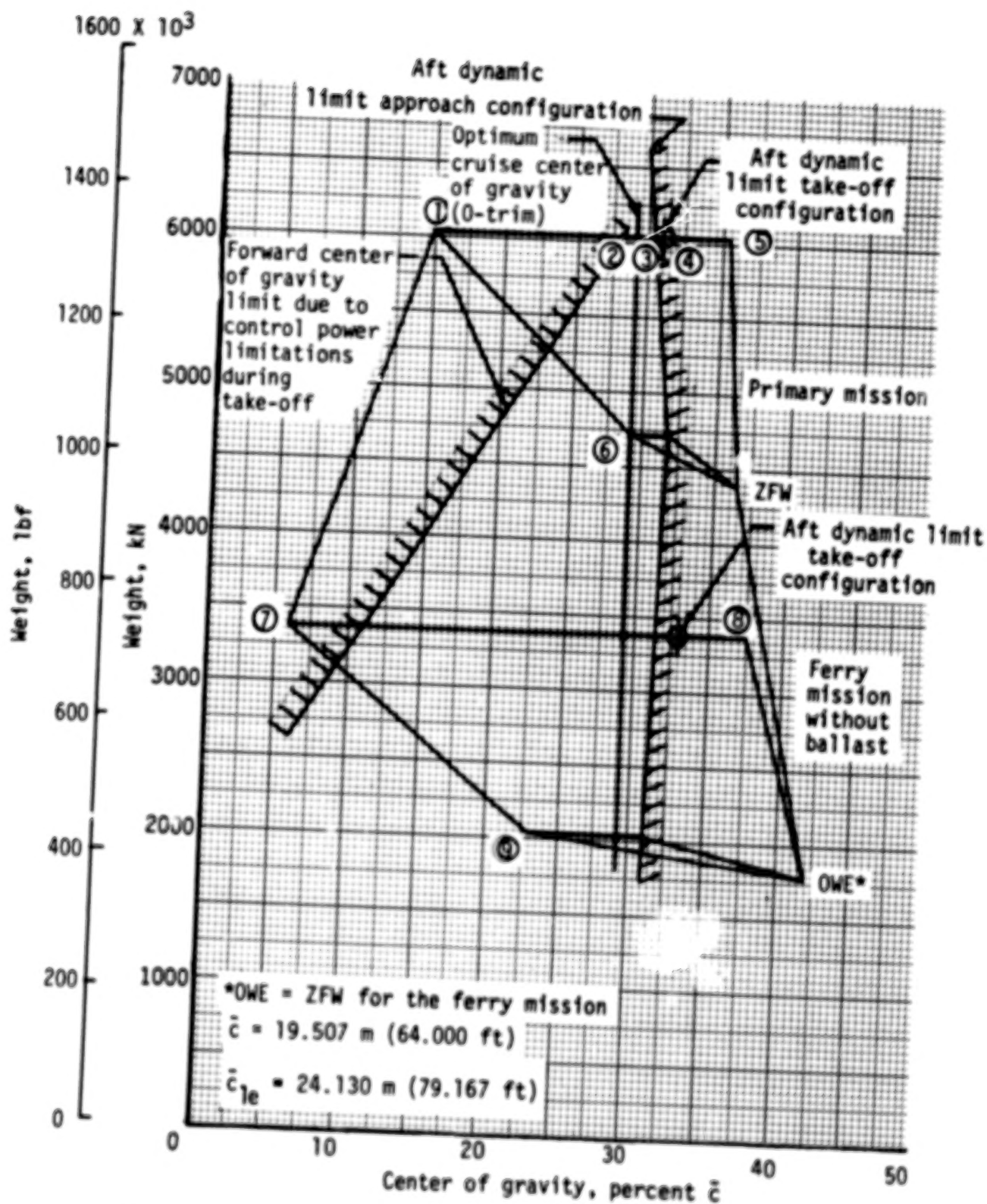
Figure 17.- Loadability envelope with flight limitations. (See table III for correlation of point number.)
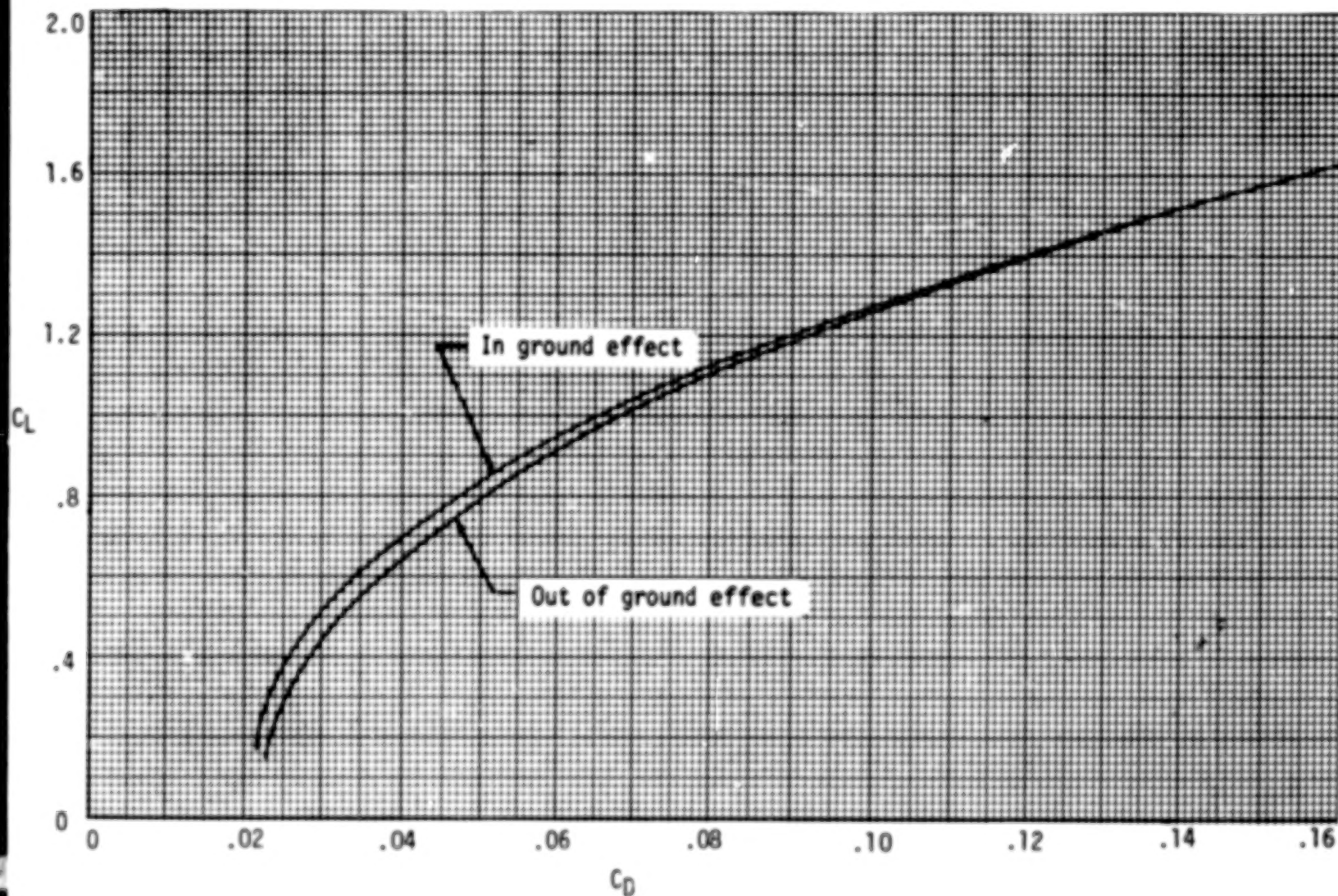
Figure 18.- Landing lift-drag polar. $S = 1724 \text{ m}^2$ (18 560 ft^2); $\delta_f = 20^\circ$; center of gravity, $0.34\bar{c}$; landing gear extended.

53
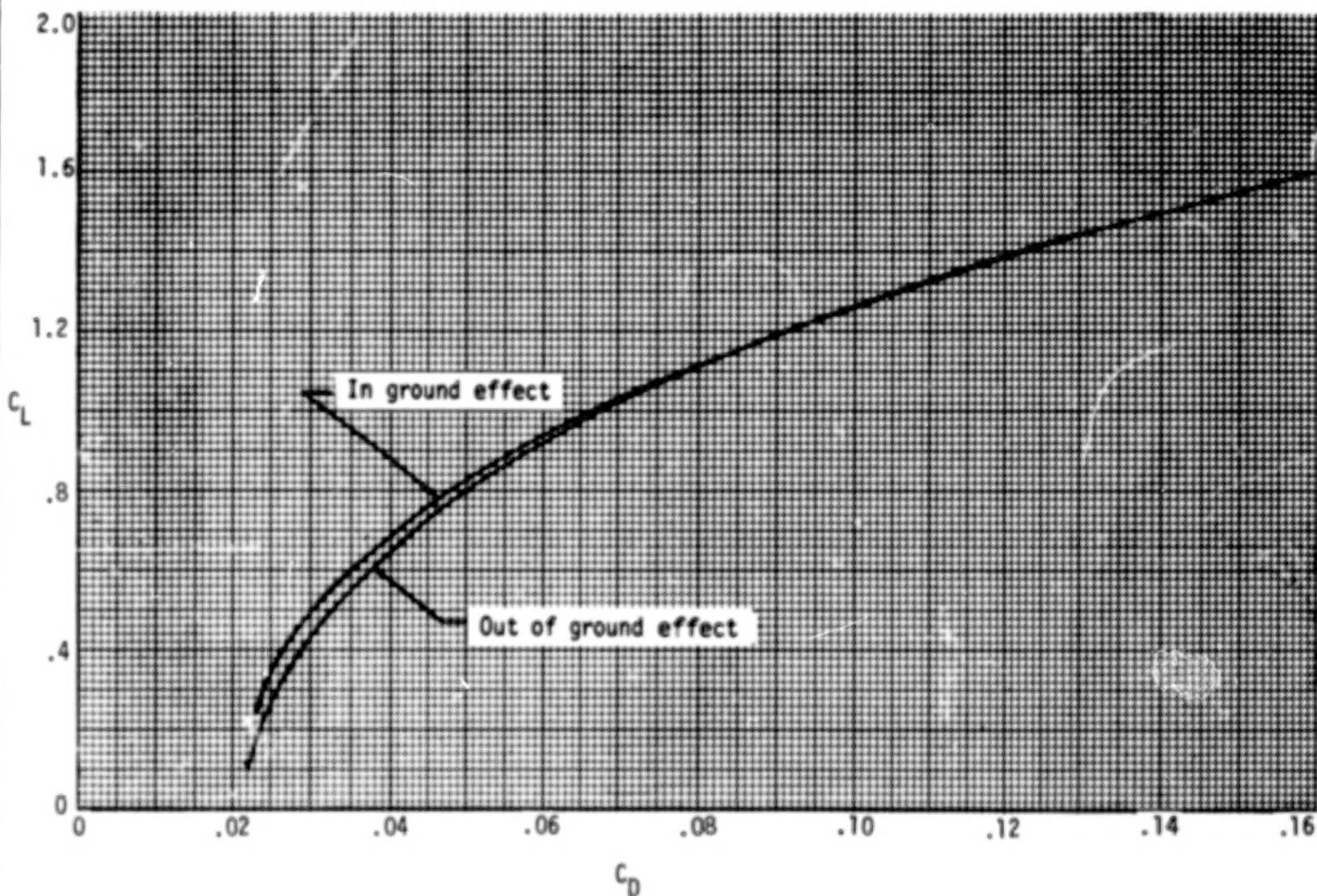
Figure 19.- Take-off lift-drag polar. S = 1724 m² (18 560 ft²); δf = 20°;
center of gravity, 0.34c̄; landing gear extended.

54
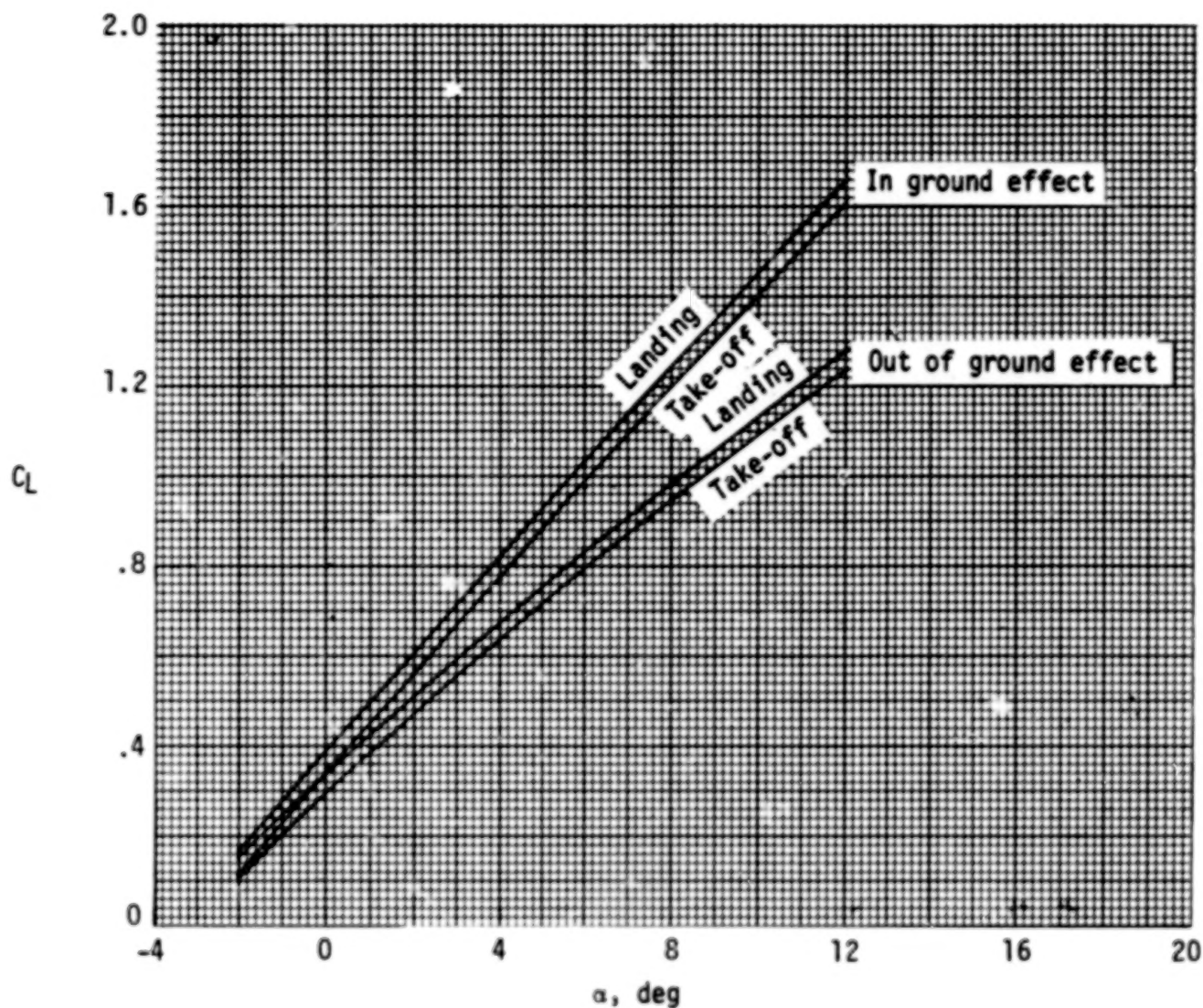
Figure 20.- Lift coefficient variation with angle of attack for take-off and landing. $S_{ref} = 1724$ m^2 (18 560 ft^2); $\delta_f = 20°$; center of gravity, $0.34\bar{c}$; landing gear extended.

55
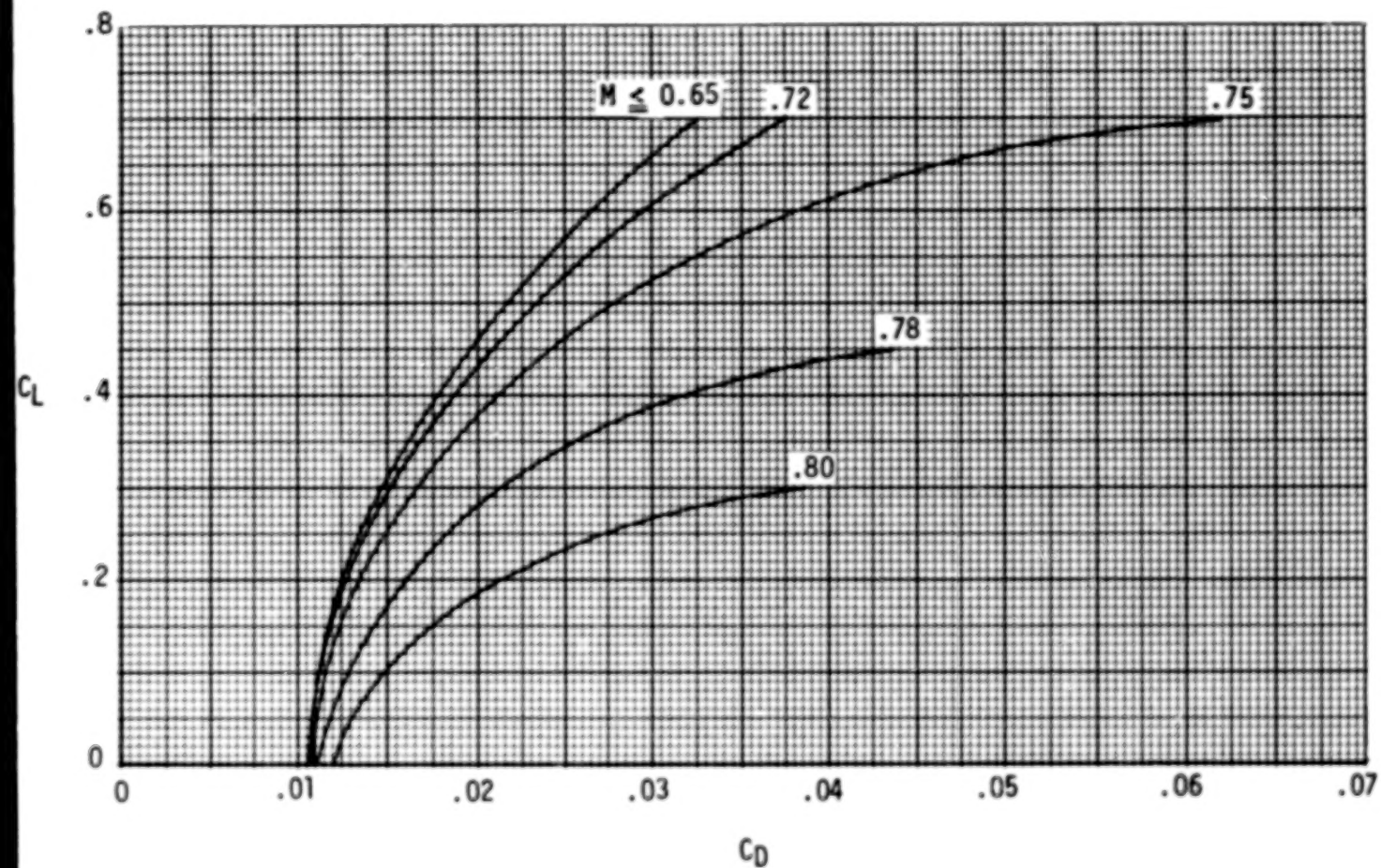
Figure 21.- Cruise lift-drag polars. S = 1724 m^2 (18 560 ft^2).

56
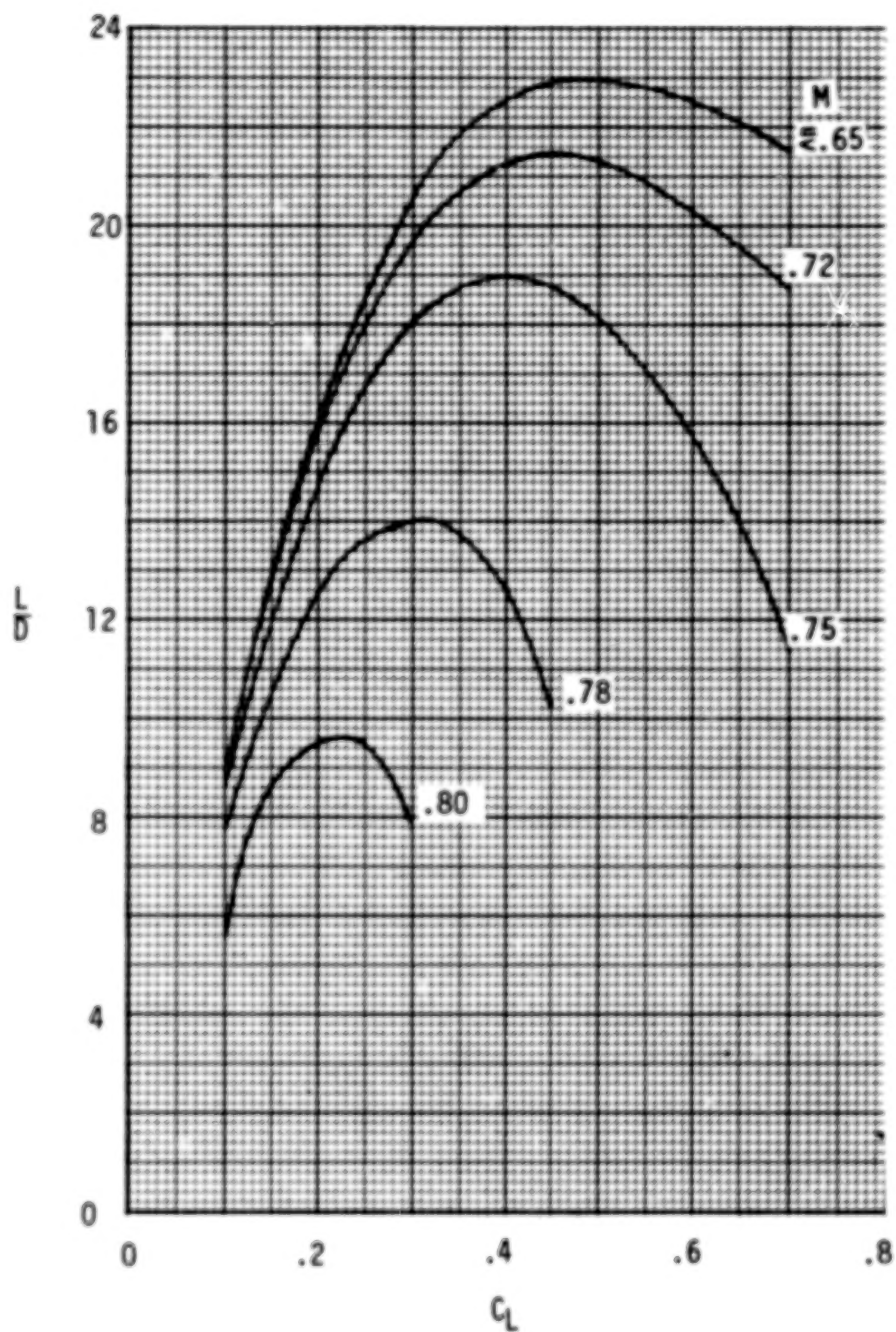
Figure 22.- Lift-drag variation with lift coefficient for several cruise Mach numbers.
$S = 1724$ m^2 (18 560 ft^2).
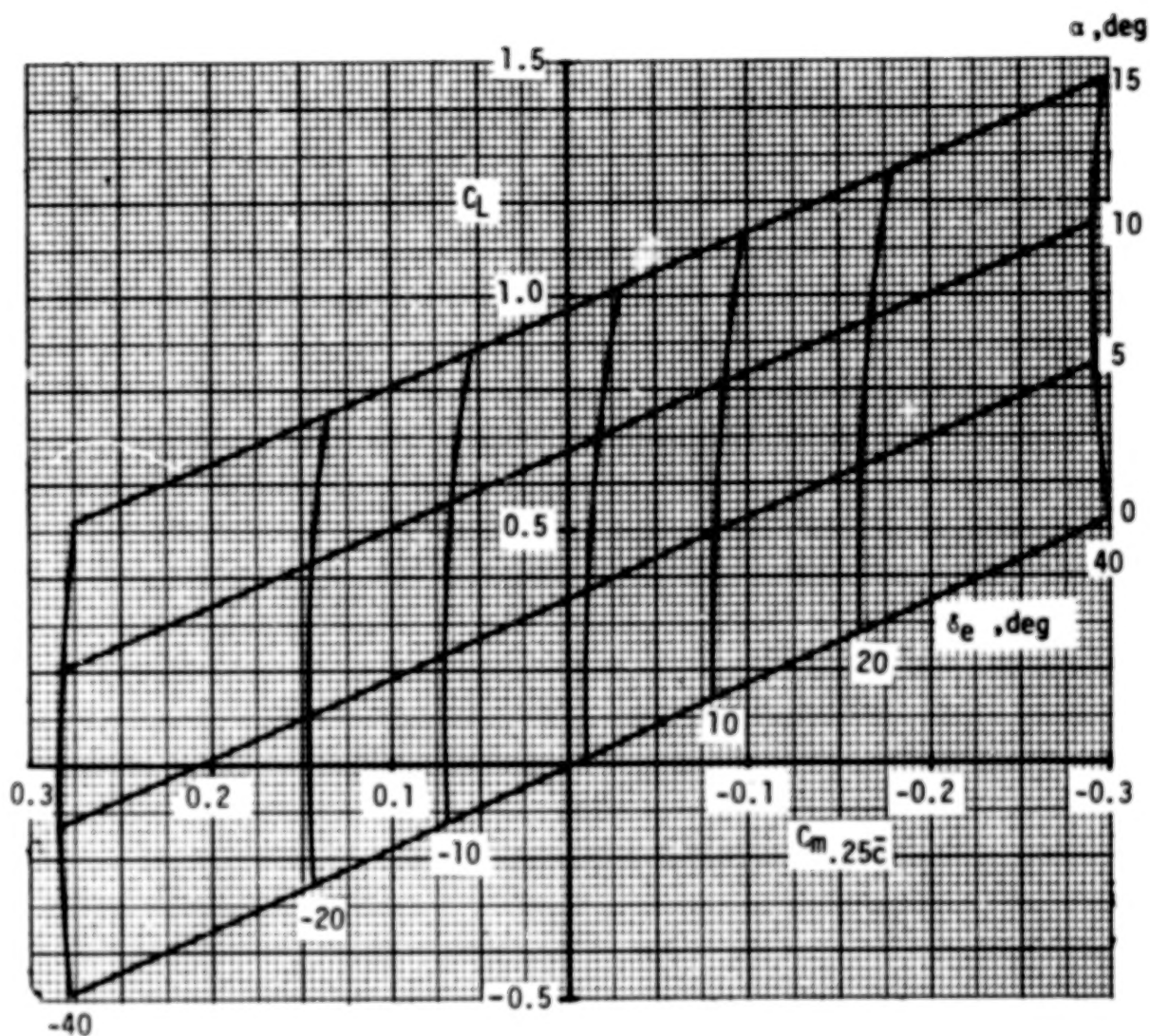
Figure 23.- Effect of elevon deflection on lift and
pitching moment. $\delta_f = 0^o$; cruise.
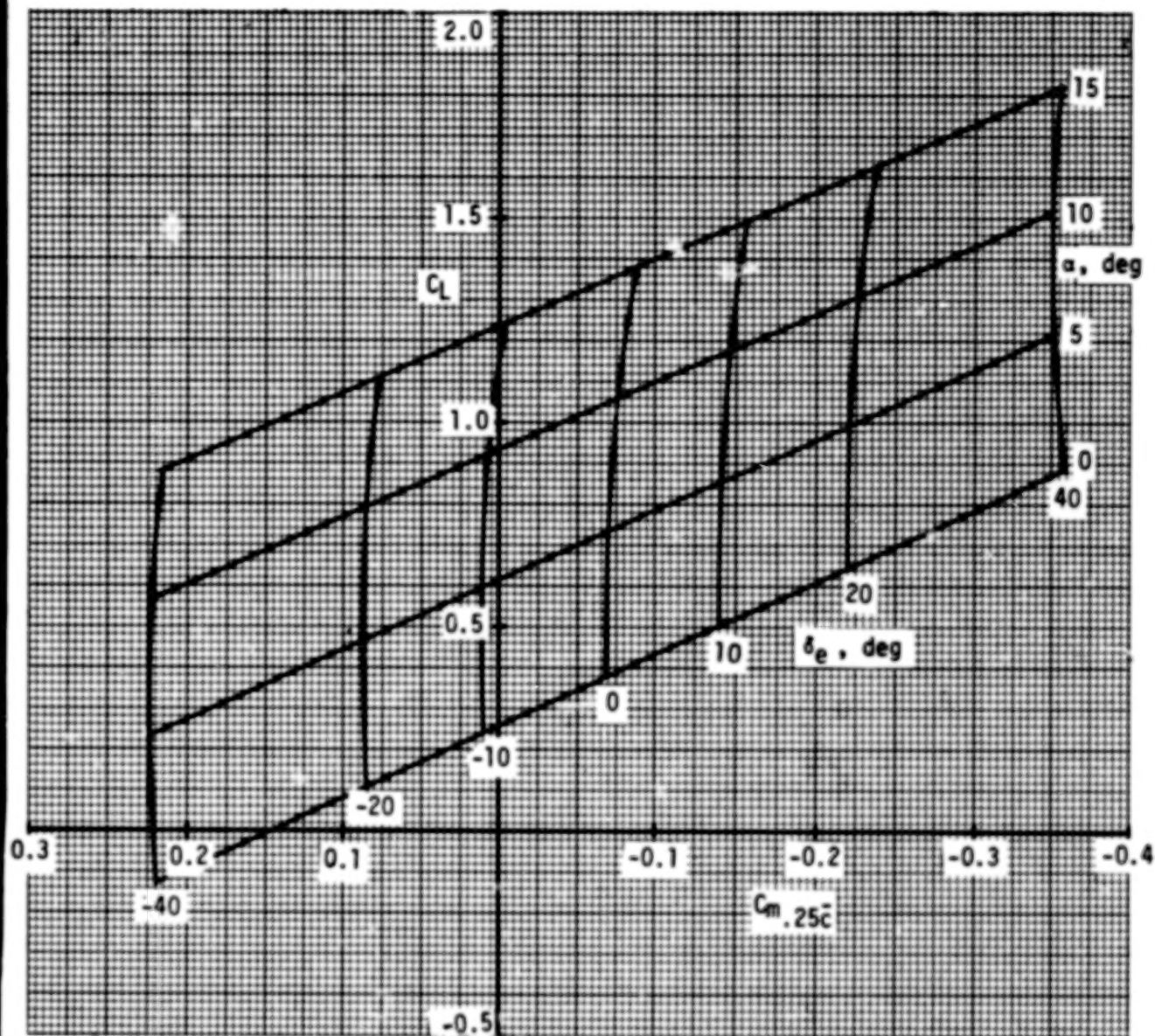
Figure 24.- Effect of elevon deflection on lift and pitching
moment during initial climb-out. $\delta_f = 20°$; initial climb-out;
thrust, 186 825 N (42 000 lbf)/engine.
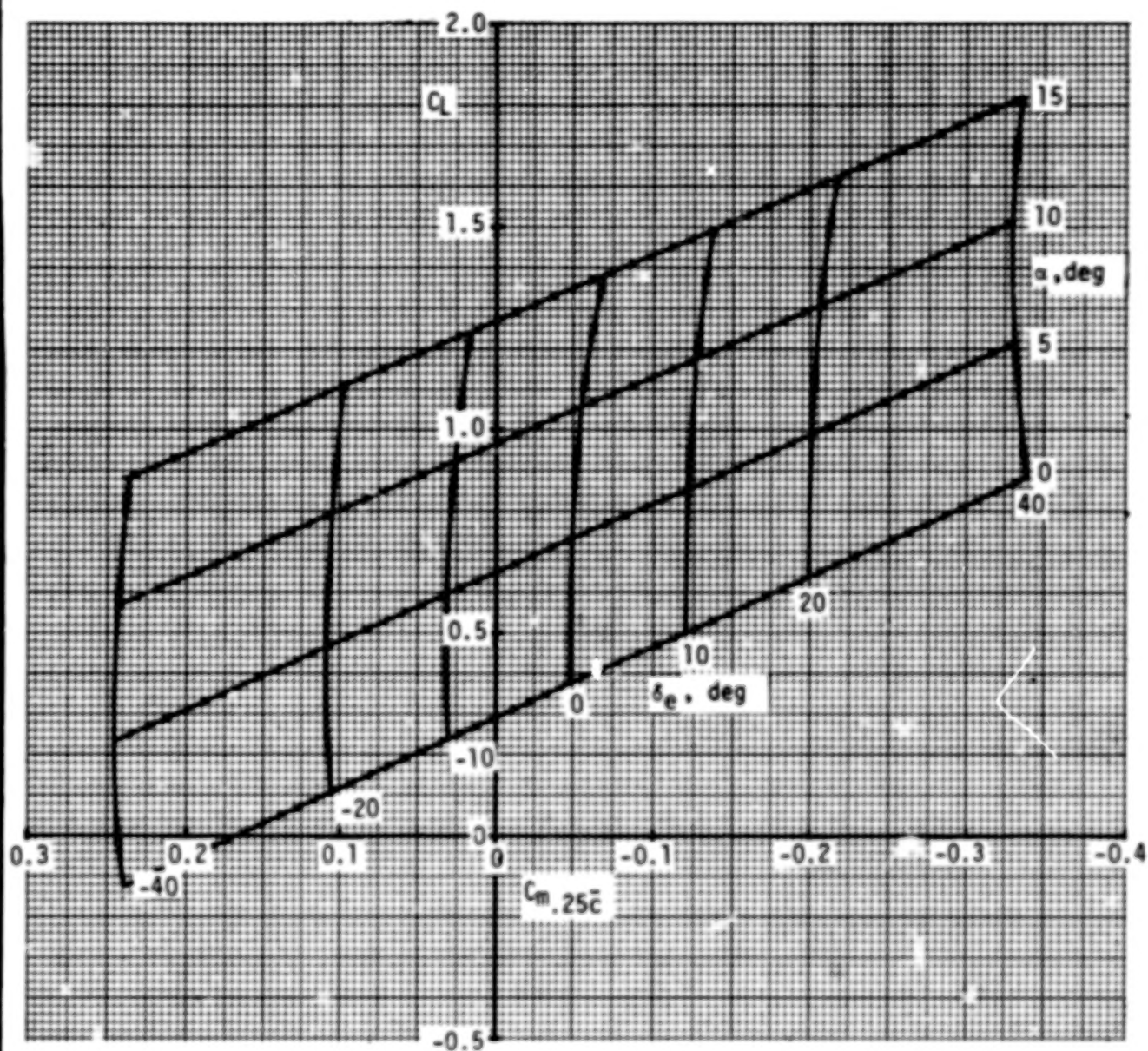
Figure 25.- Effect of elevon deflection on lift and
pitching moment during approach. $\delta_f = 20^o$; approach;
thrust, 24 465 N (5500 lbf)/engine.
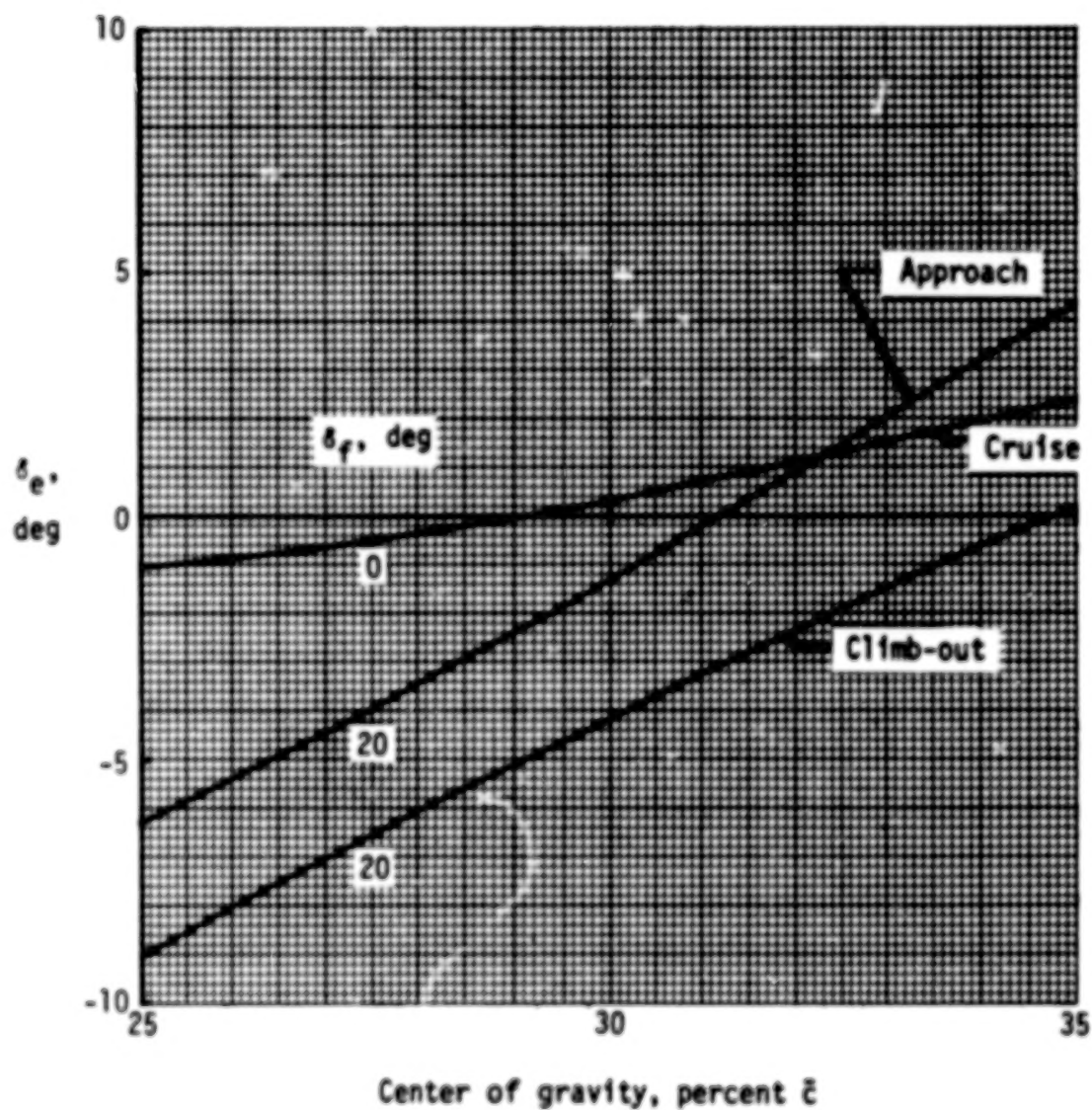
Figure 26.- Elevon required to trim.

61.
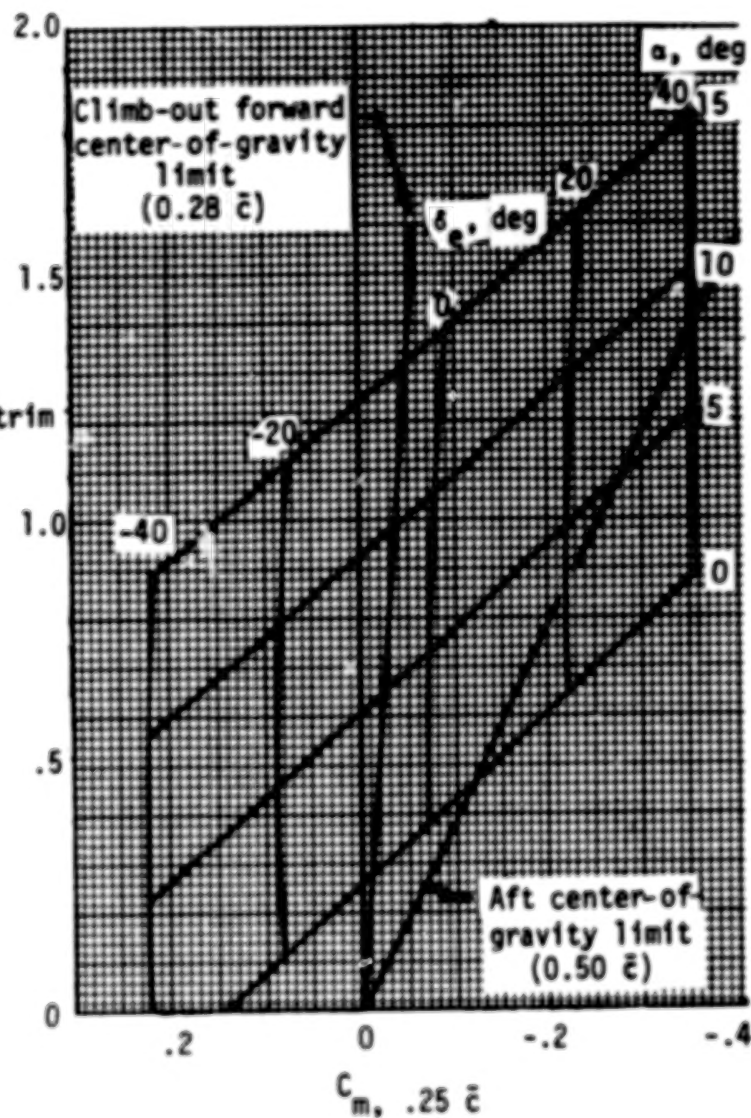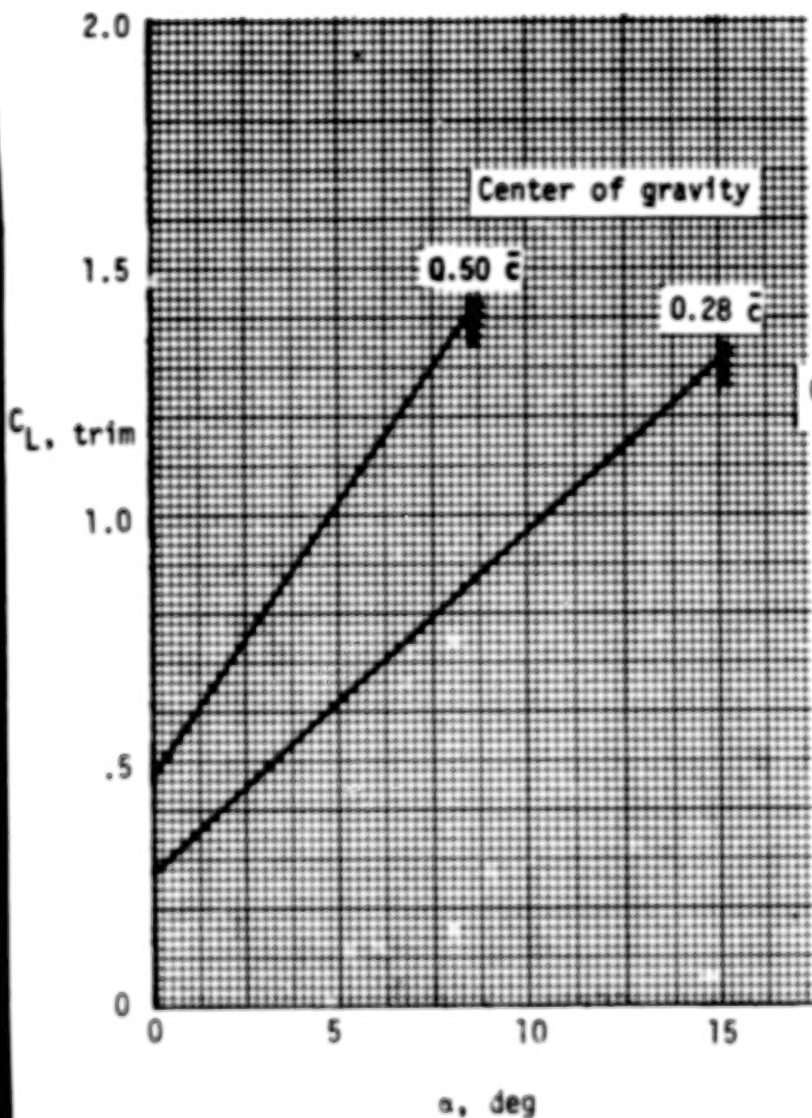
Figure 27.- Span-loader initial climb-out trim and stability. Out-of-ground effect; $\delta_f = 20^\circ$.
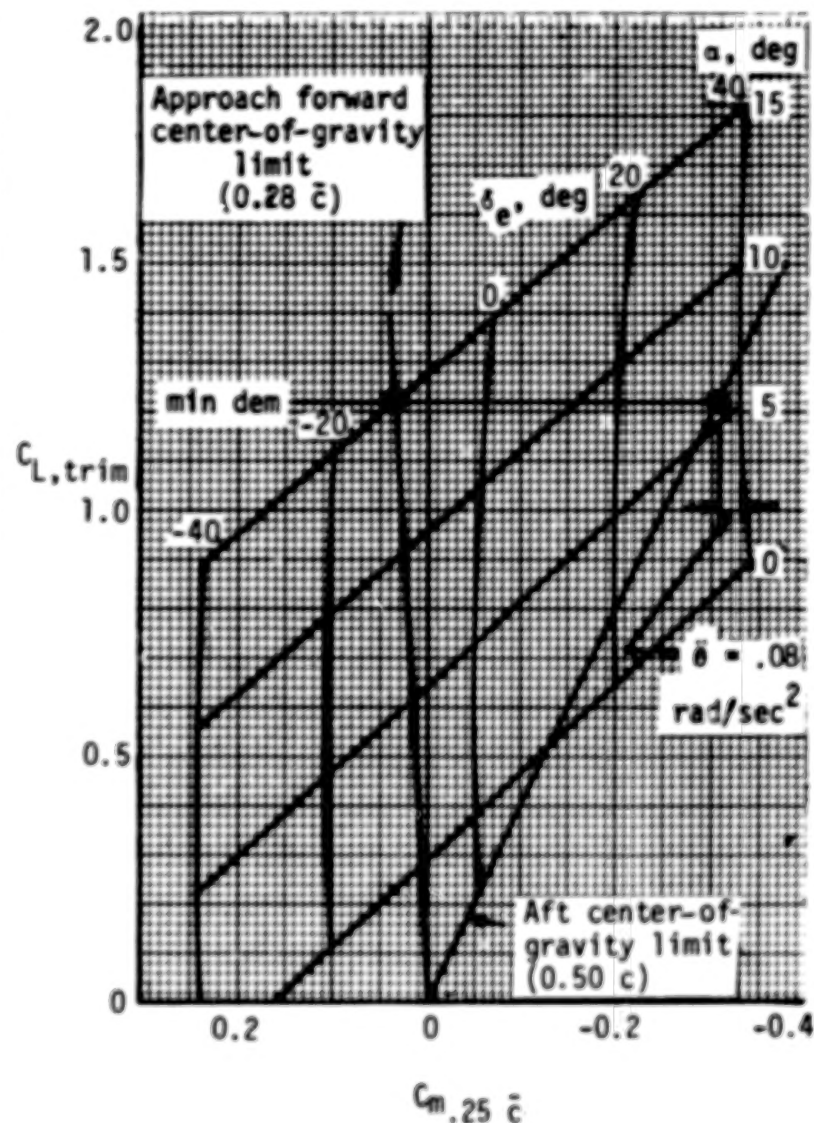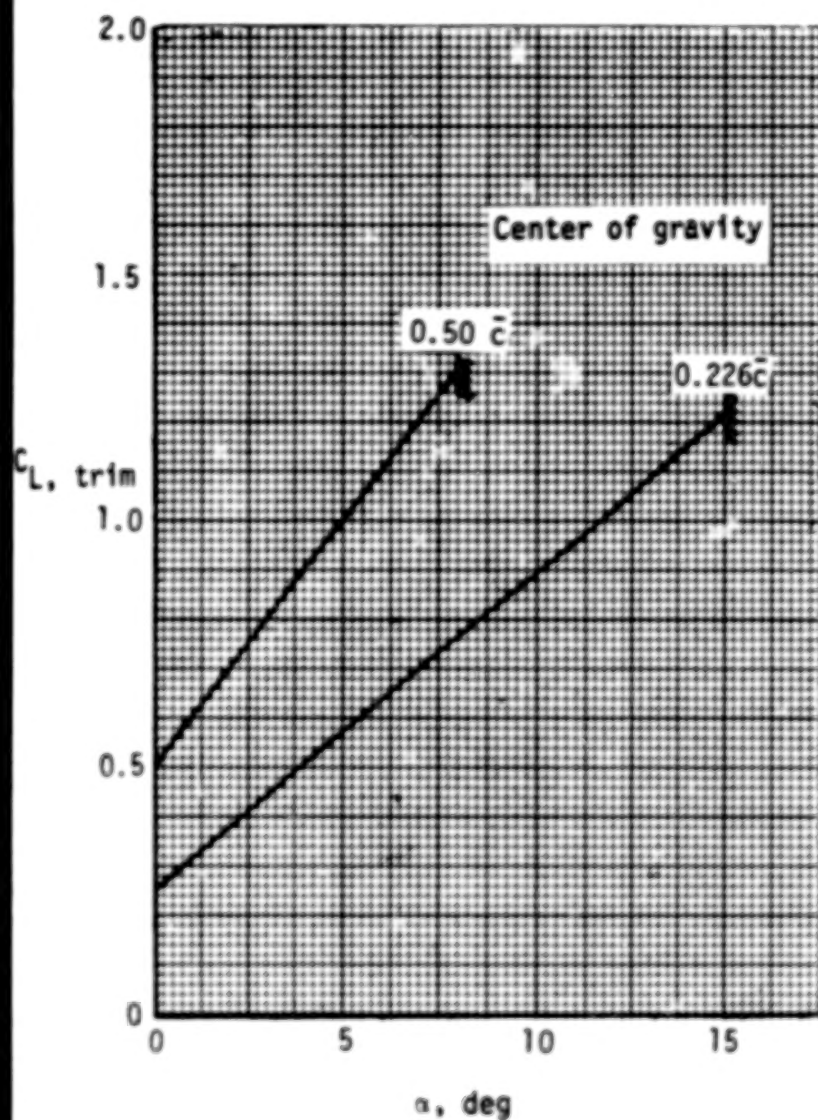
Figure 28.- Aircraft final approach trim and stability. Out-of-ground effect; $\delta_f = 20°$.

63
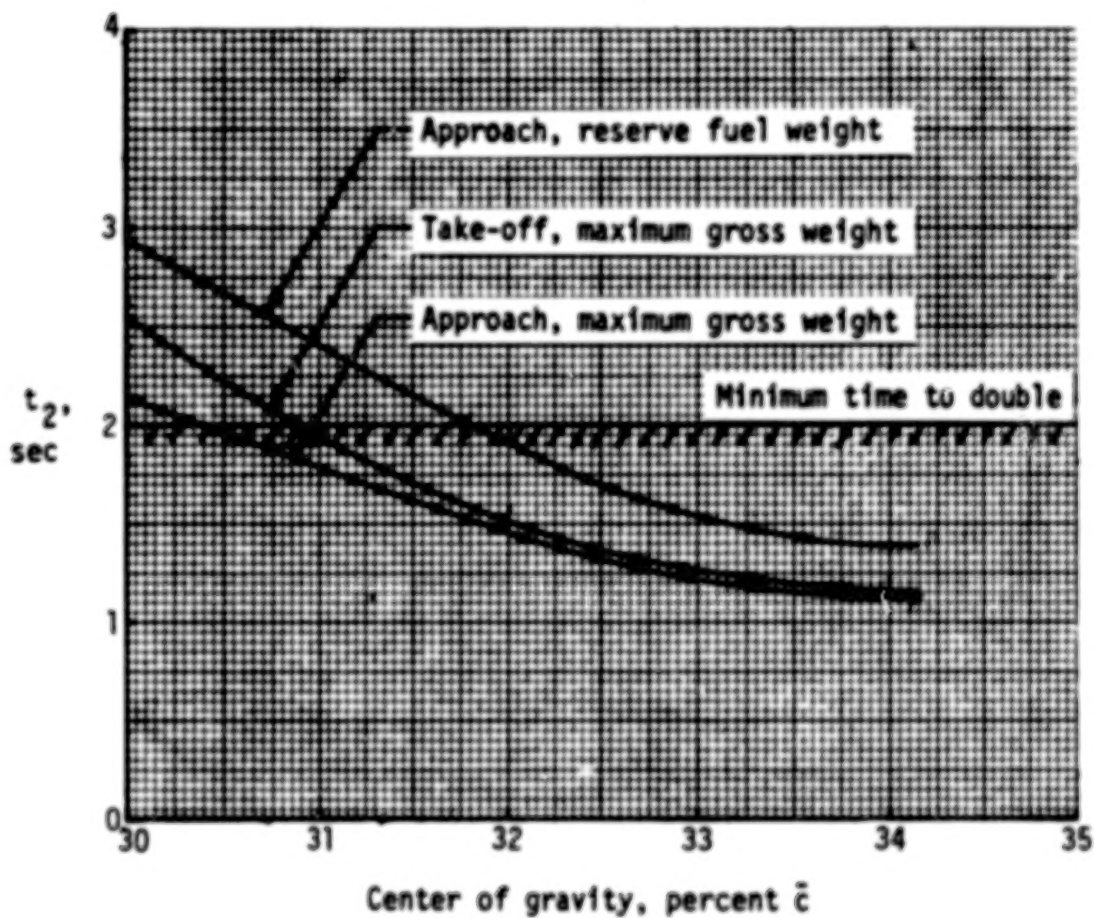
Figure 29.- Estimated time to double amplitude for aircraft in approach and take-off configurations.

64.
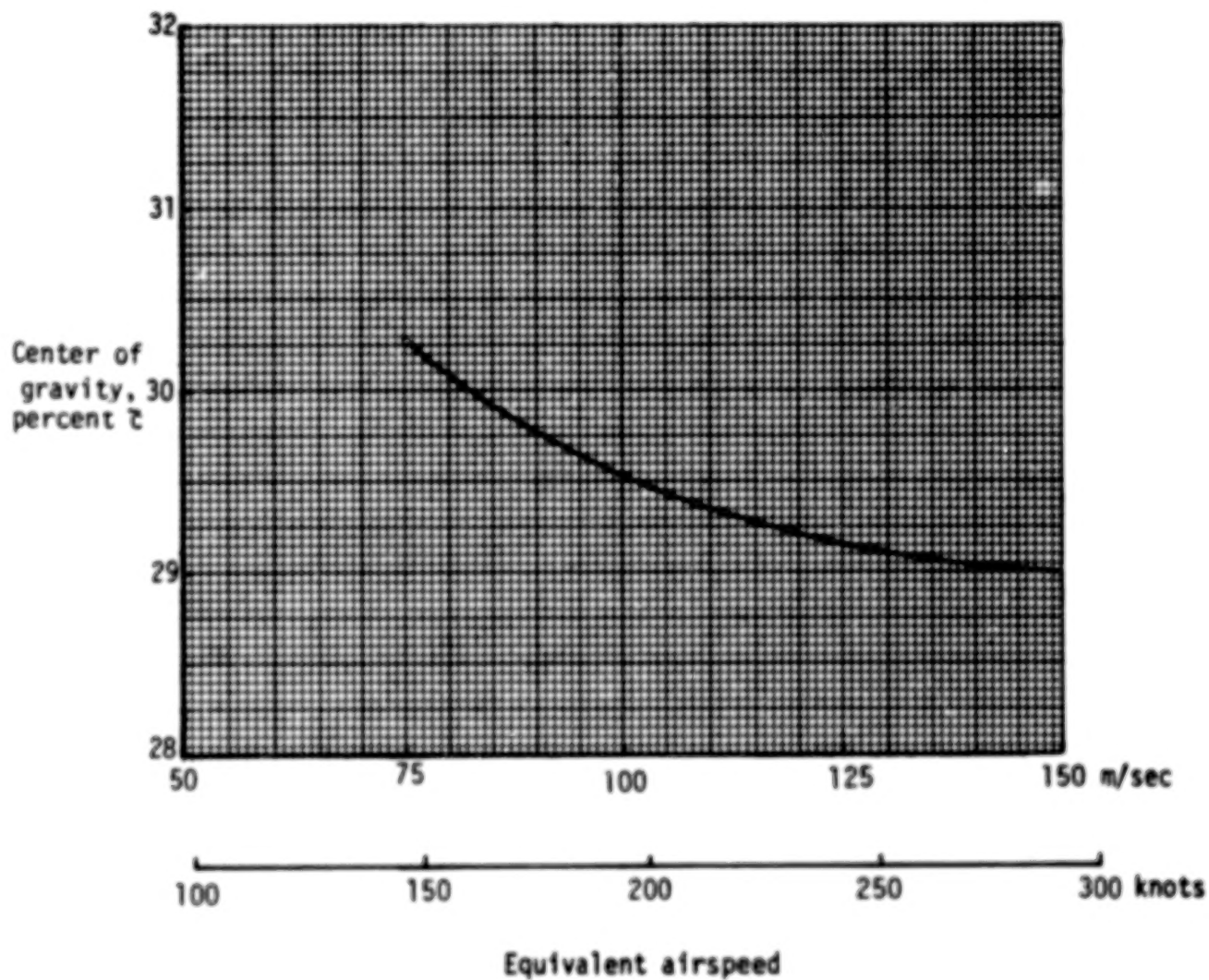
Figure 30.- Rearward dynamic center-of-gravity limit for climb-acceleration mode. $\delta_f = 0°$.

65.
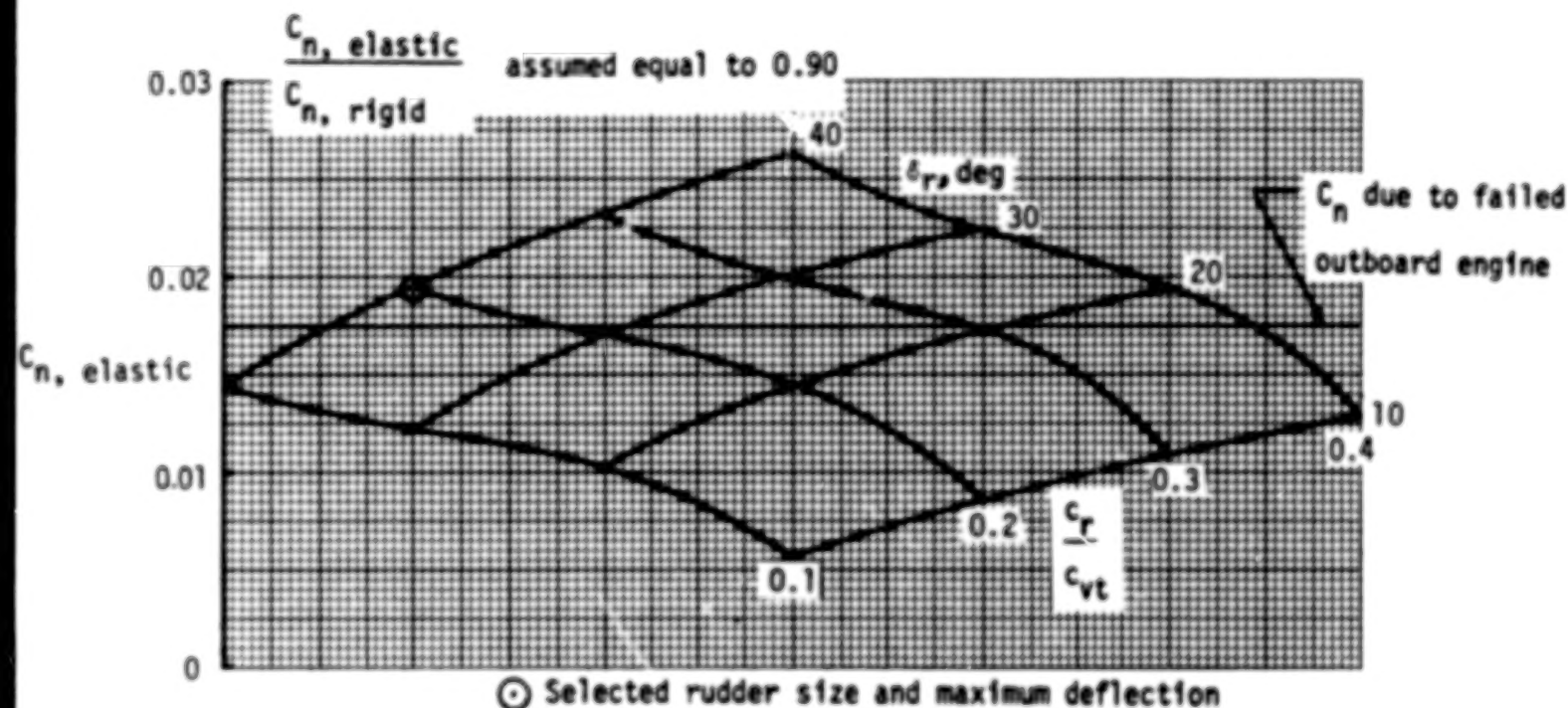
Figure 31.- Estimated aircraft directional control capability
assuming an outboard engine failure. W = 6 052 250 N
(1 360 600 lbf); maximum thrust on five operating engines;
V = 263 km/hr (142 knots) EAS; S_V = 219.4 m^2 (2362 ft^2).

66
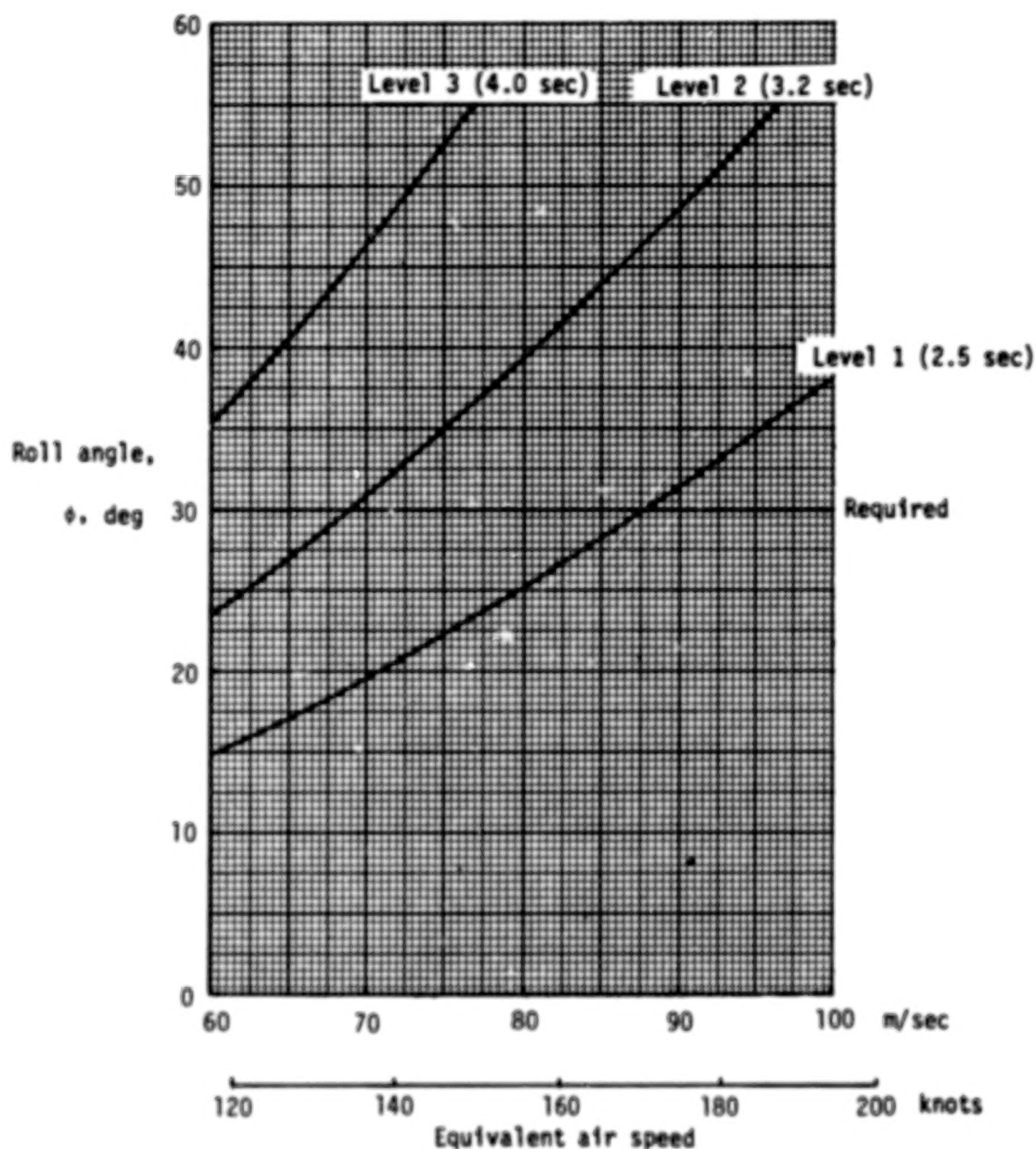
Figure 32.- Estimated aircraft roll response to a lateral
step input. Landing approach. Approach configuration;
$C_{n,elastic}/C_{n,rigid}$ assumed equal to 0.90; class III;
category C, reference 14.
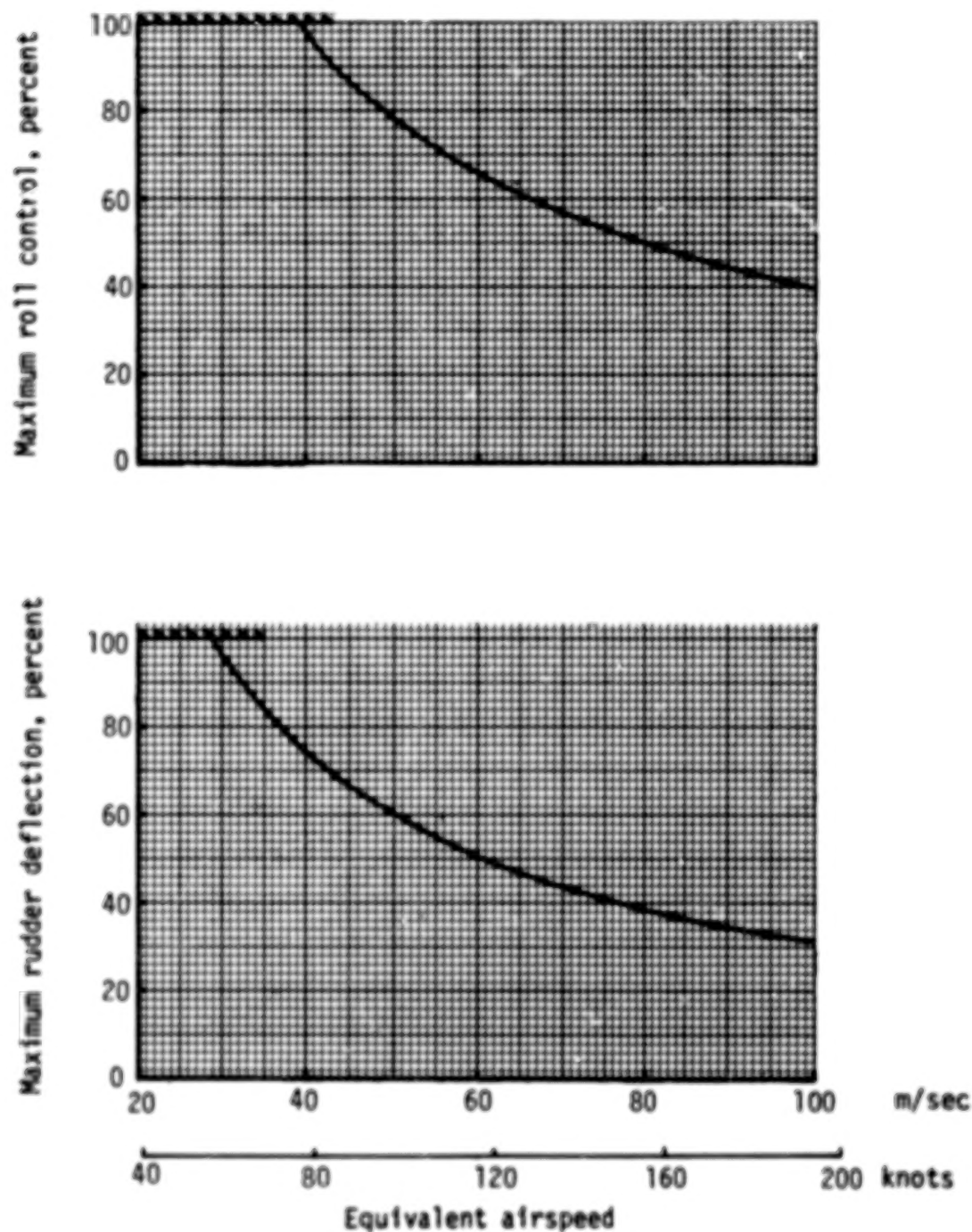
Figure 33.- Estimated aircraft directional trim requirements in a 90°, 15.4 m/sec (30 knots) cross wind.
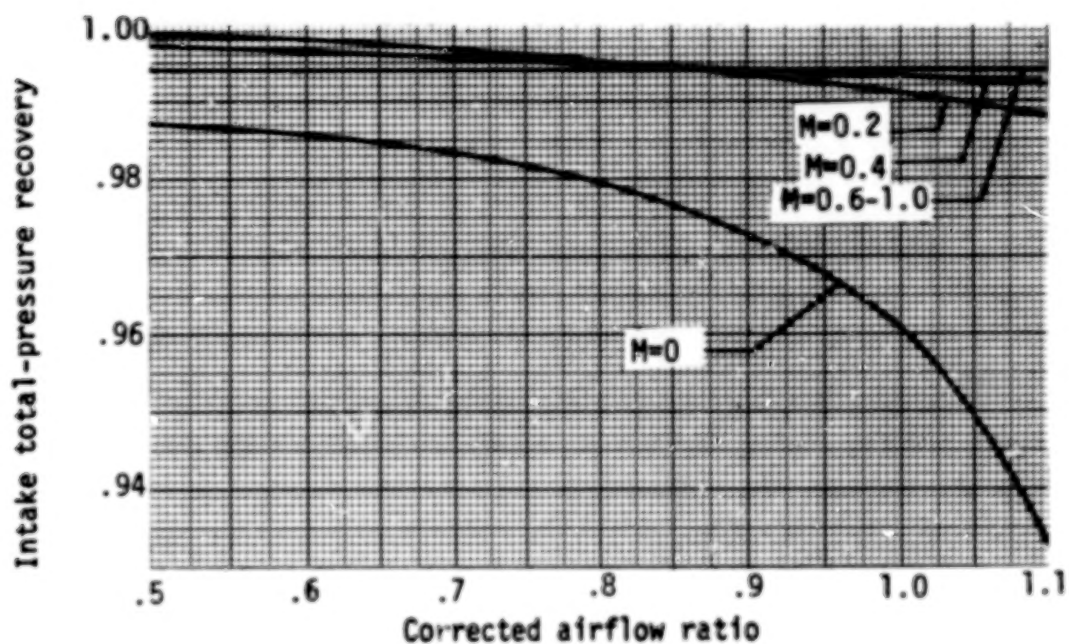
Figure 34.- Air-inlet total pressure recovery.
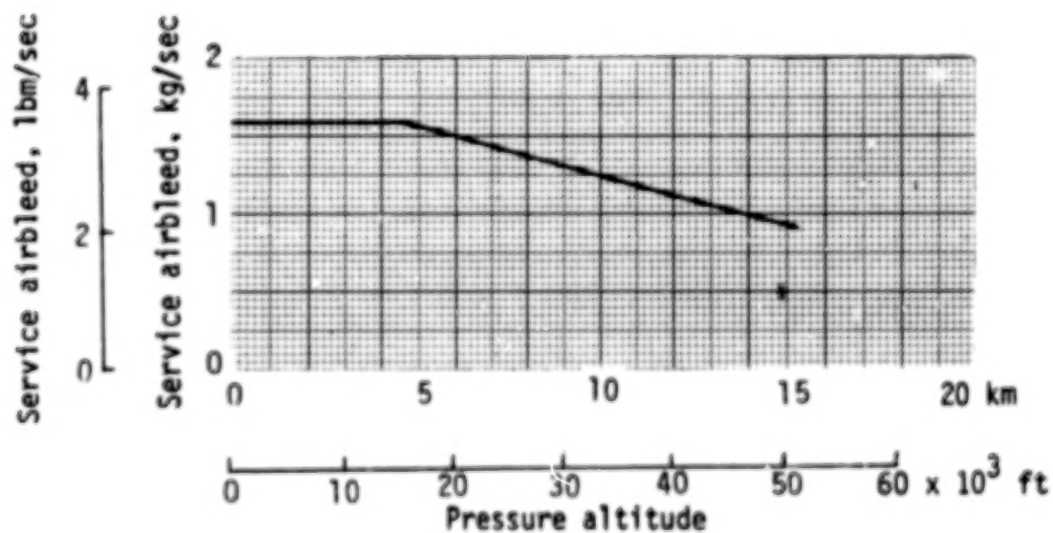
Figure 35.- Service airbleed schedule per engine.
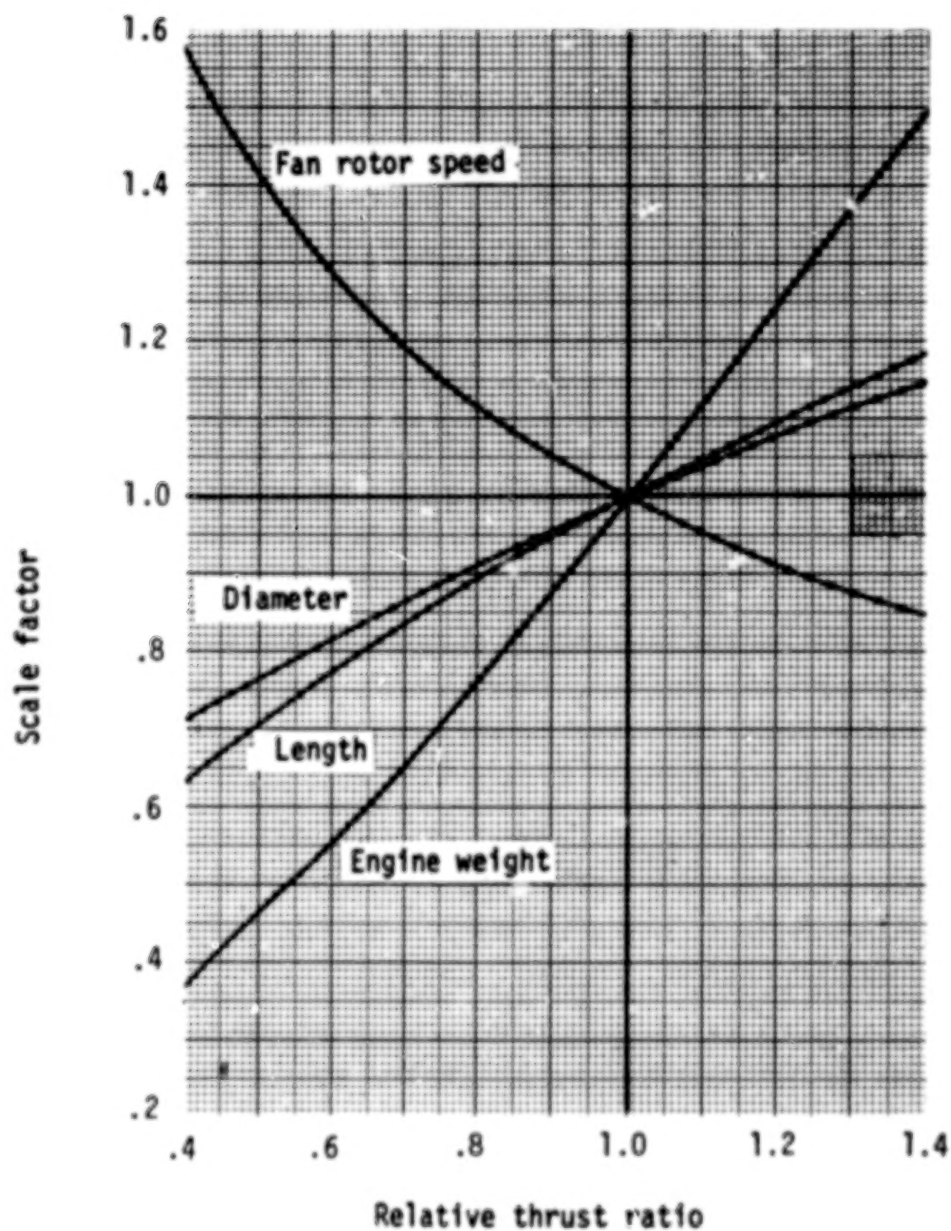
Figure 36.- Engine and nacelle scaling factors.
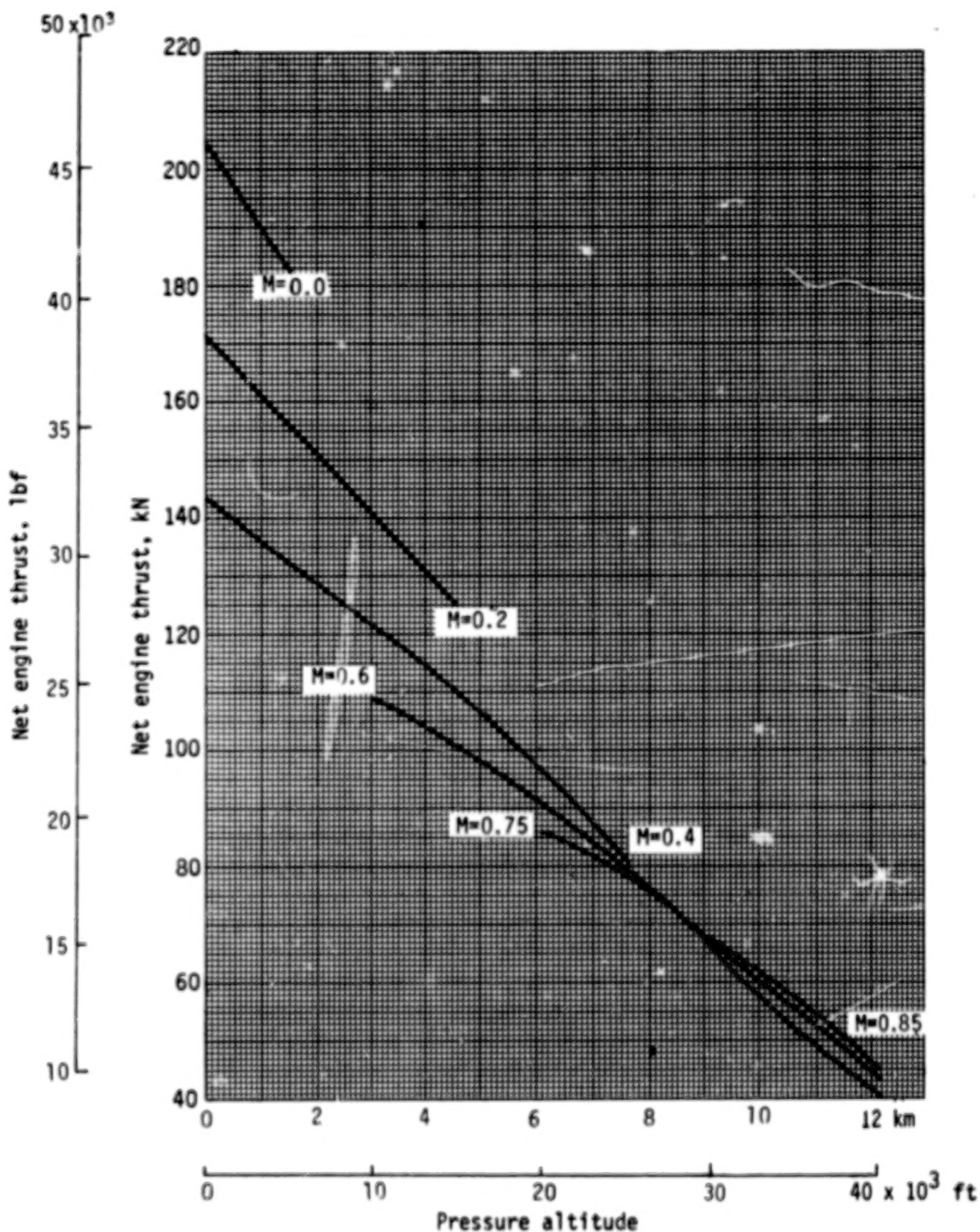
Figure 37.- Installed maximum-climb net engine thrust.
Standard day to (standard day + 10° C).
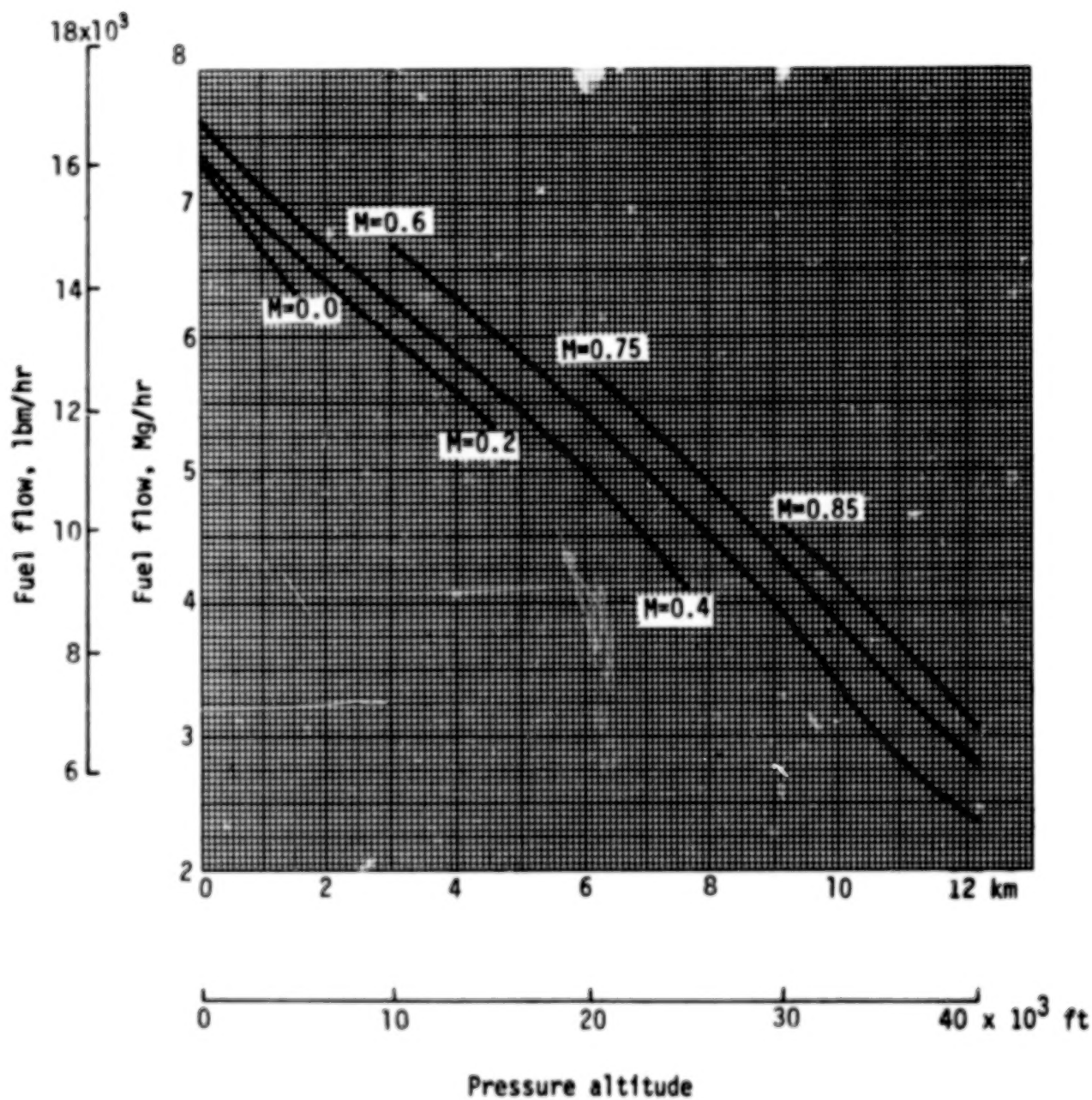
Figure 38.- Installed maximum-climb fuel flow. Standard day.
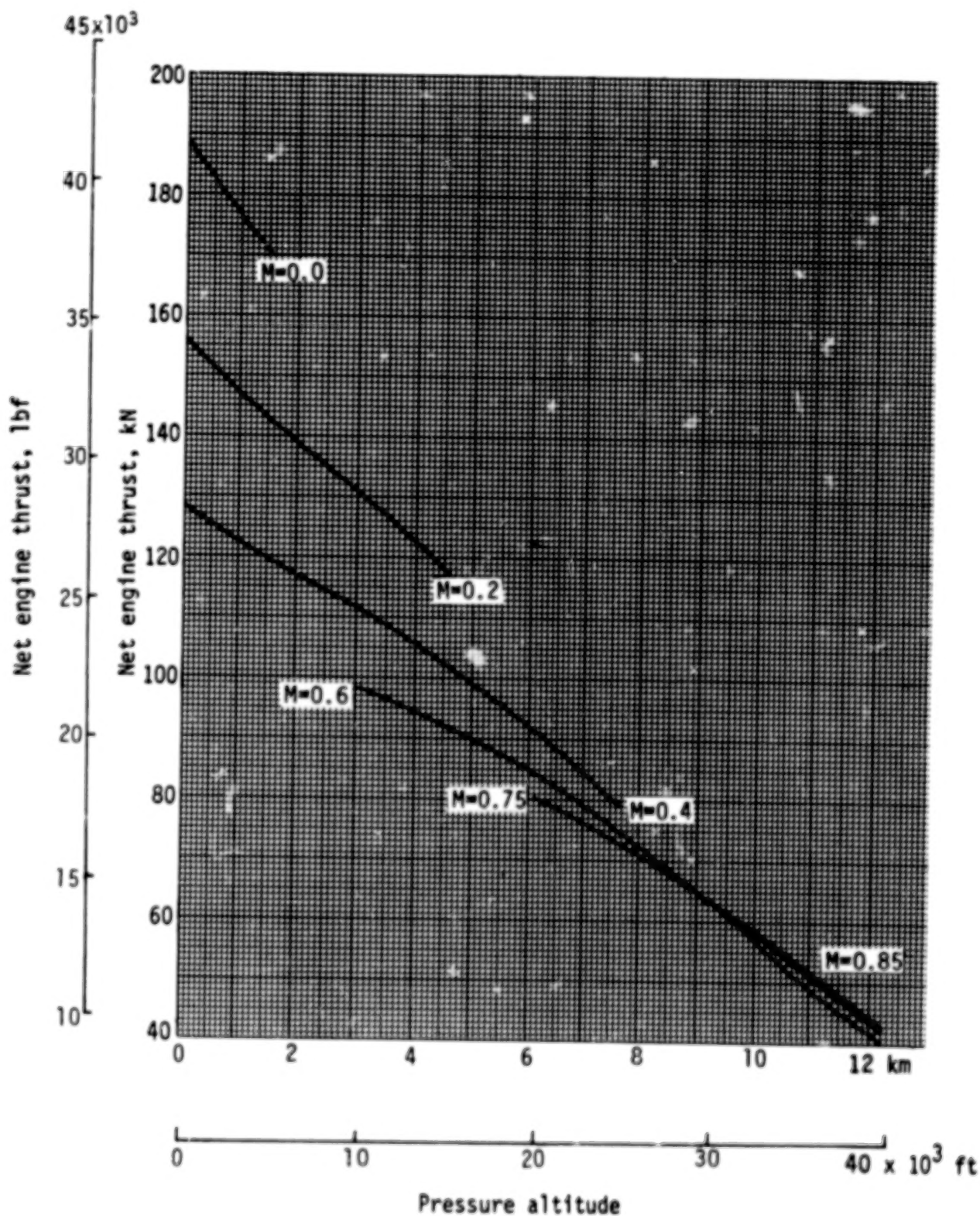
Figure 39.- Installed maximum-cruise net engine thrust.
Standard day to (standard day + 15° C).
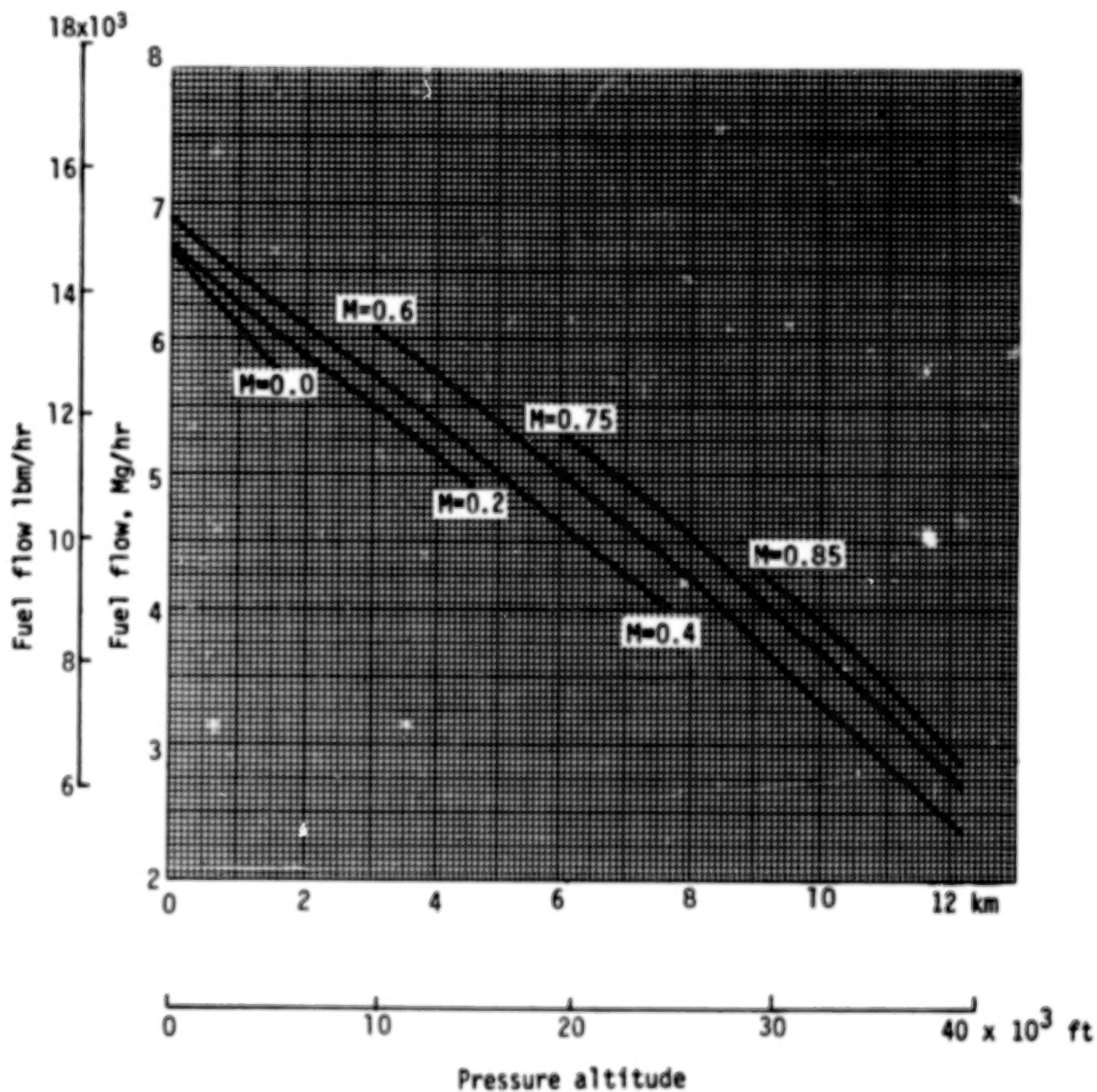
Figure 40.- Installed maximum-cruise fuel flow. Standard day.
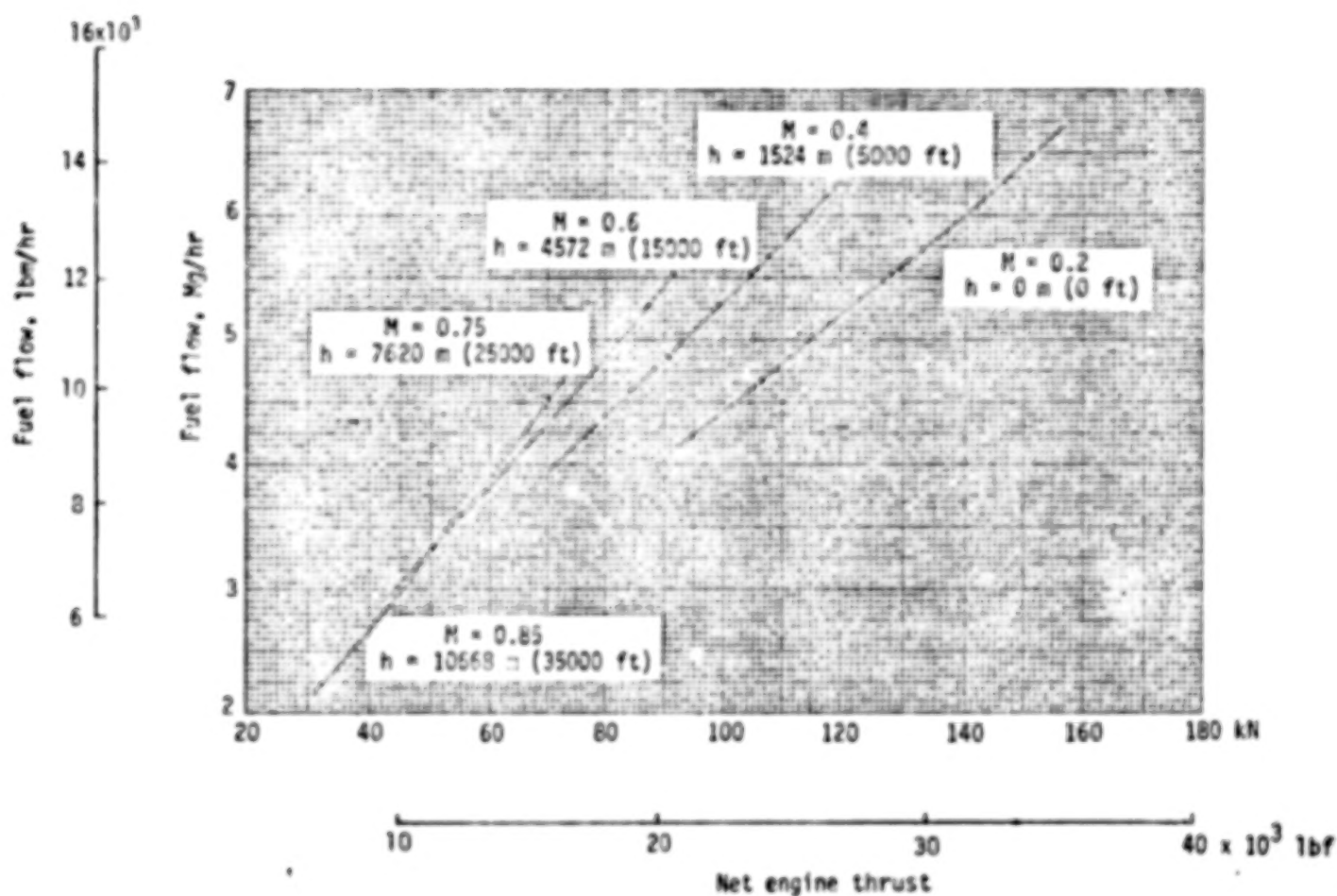
Figure 41.- Installed fuel flow at maximum and part-power
cruise thrust. Standard day.

75.
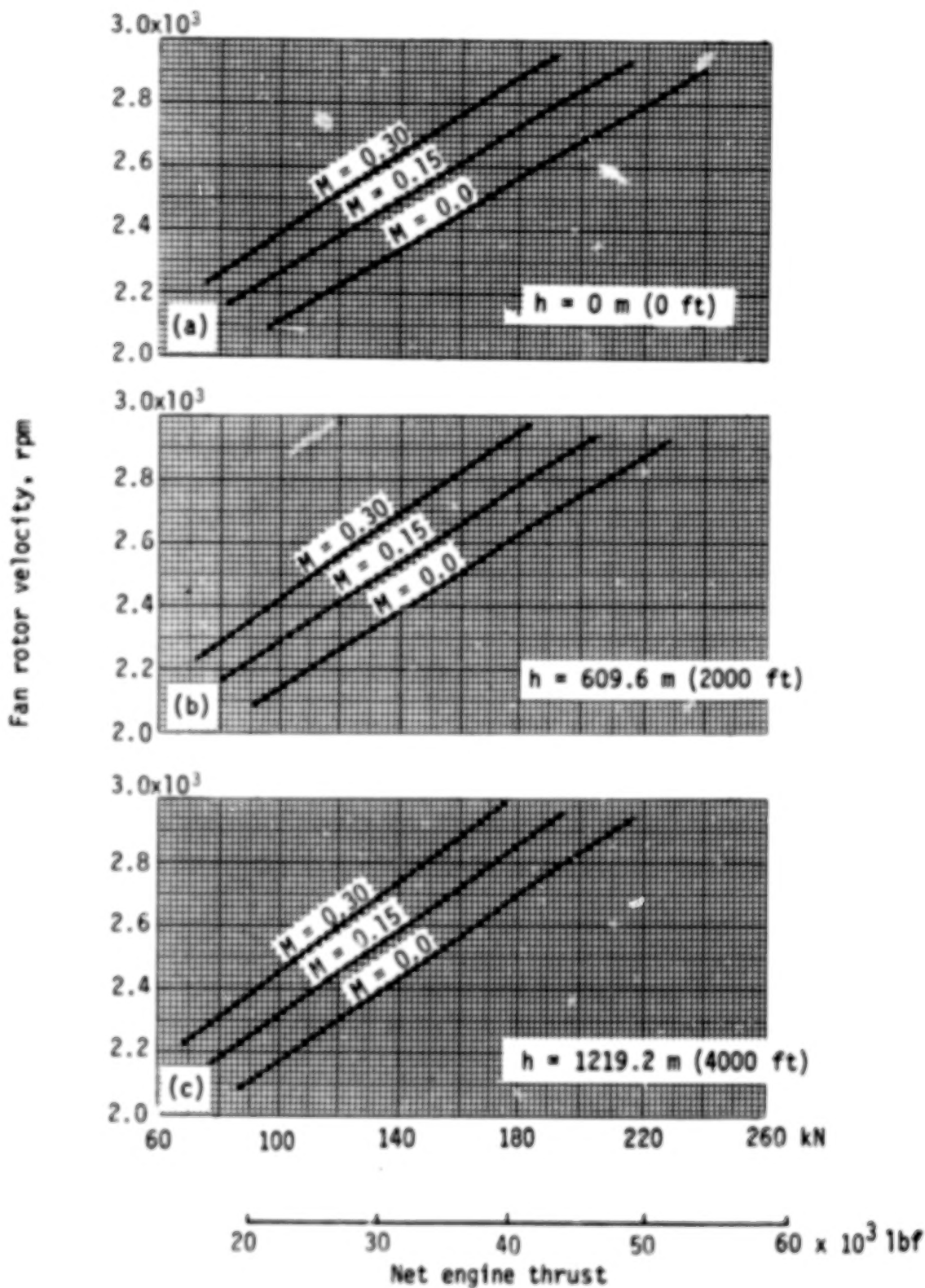
Figure 42.- Installed fan rotor speed at take-off and part-power cruise thrust. Standard day + 10° C.
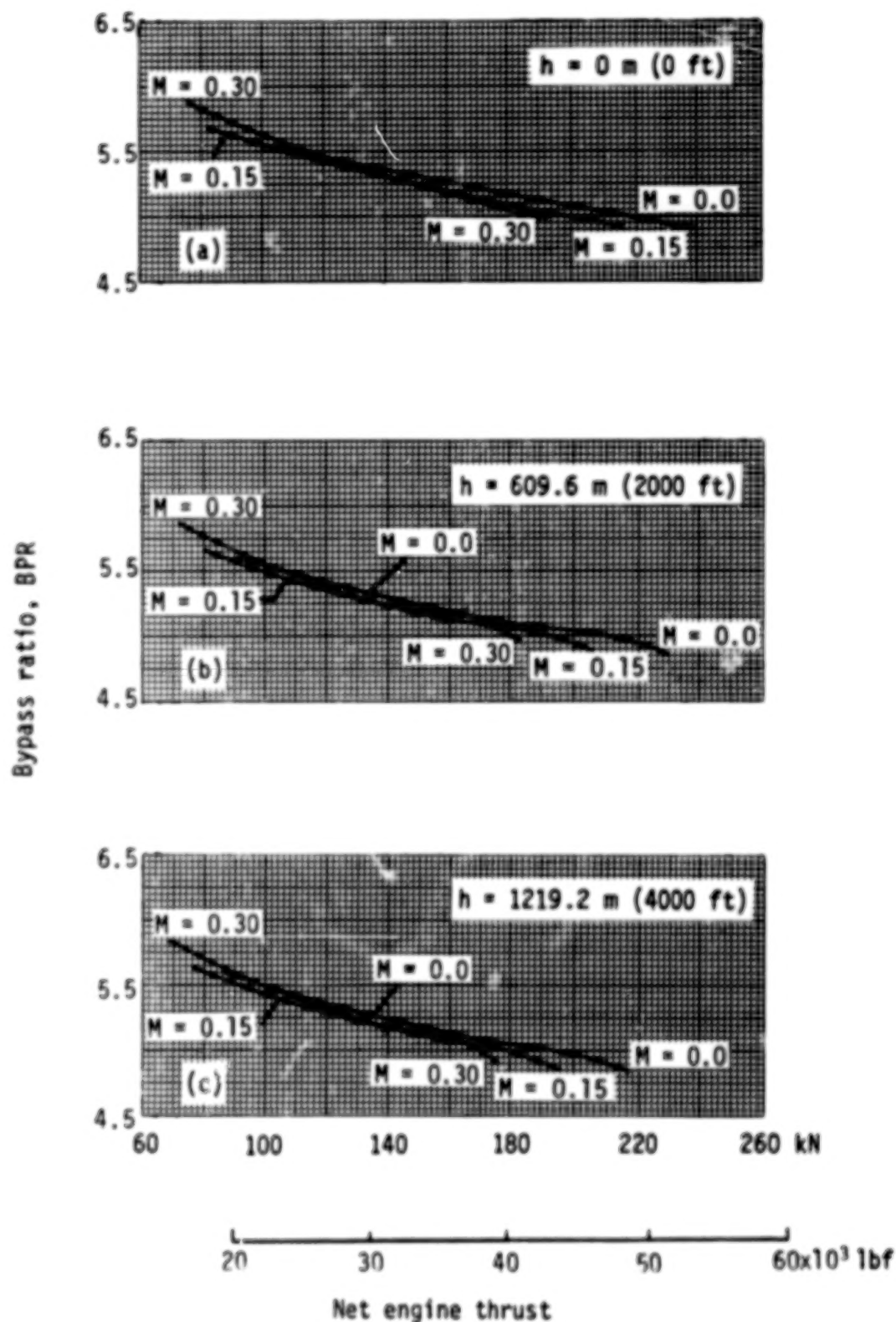
Figure 43.- Installed engine bypass ratio at take-off
and part-power cruise thrust. Standard day + 10° C.
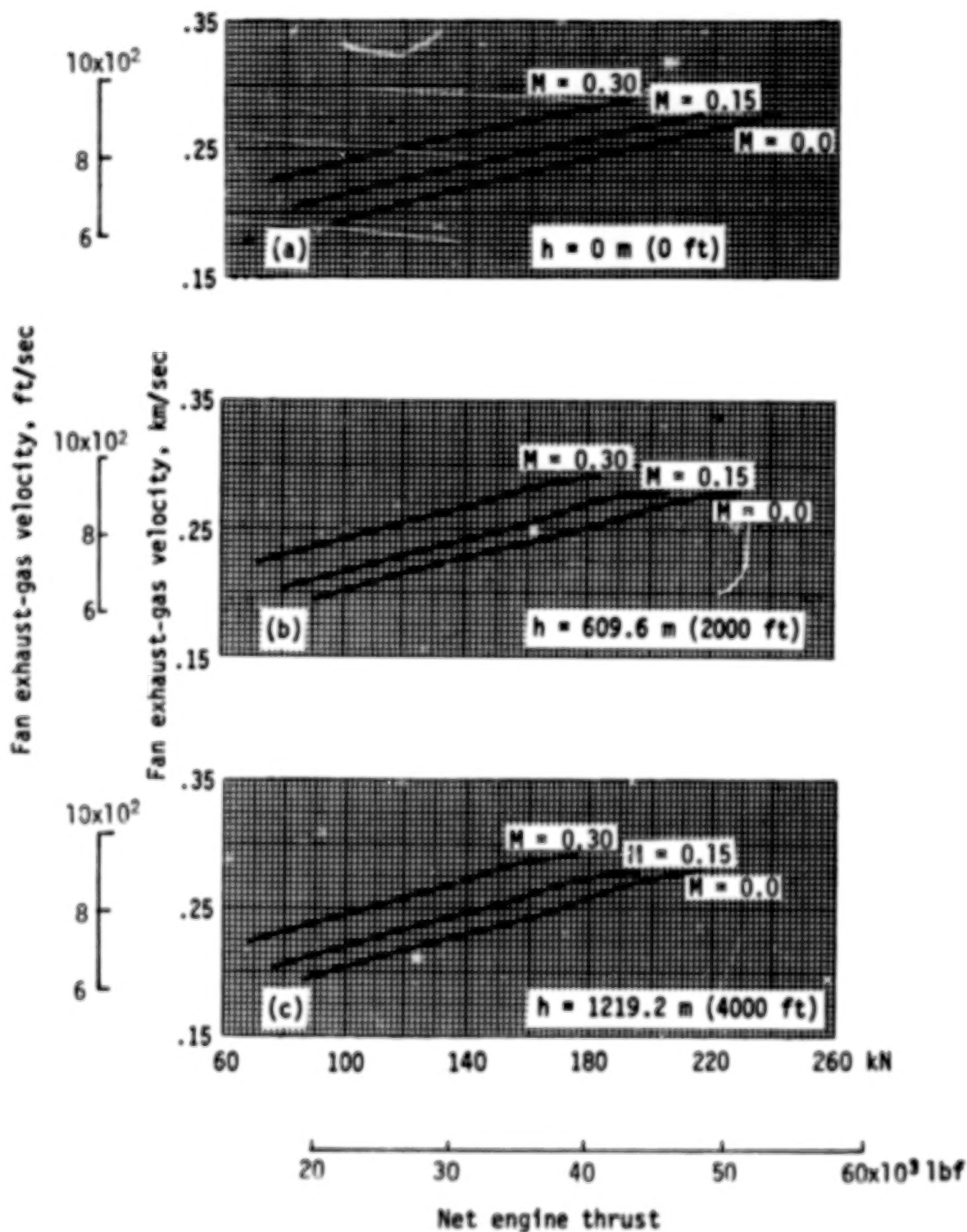
Figure 44.- Installed fan exhaust-gas velocity at take-off
and part-power cruise thrust. Standard day + 10° C.
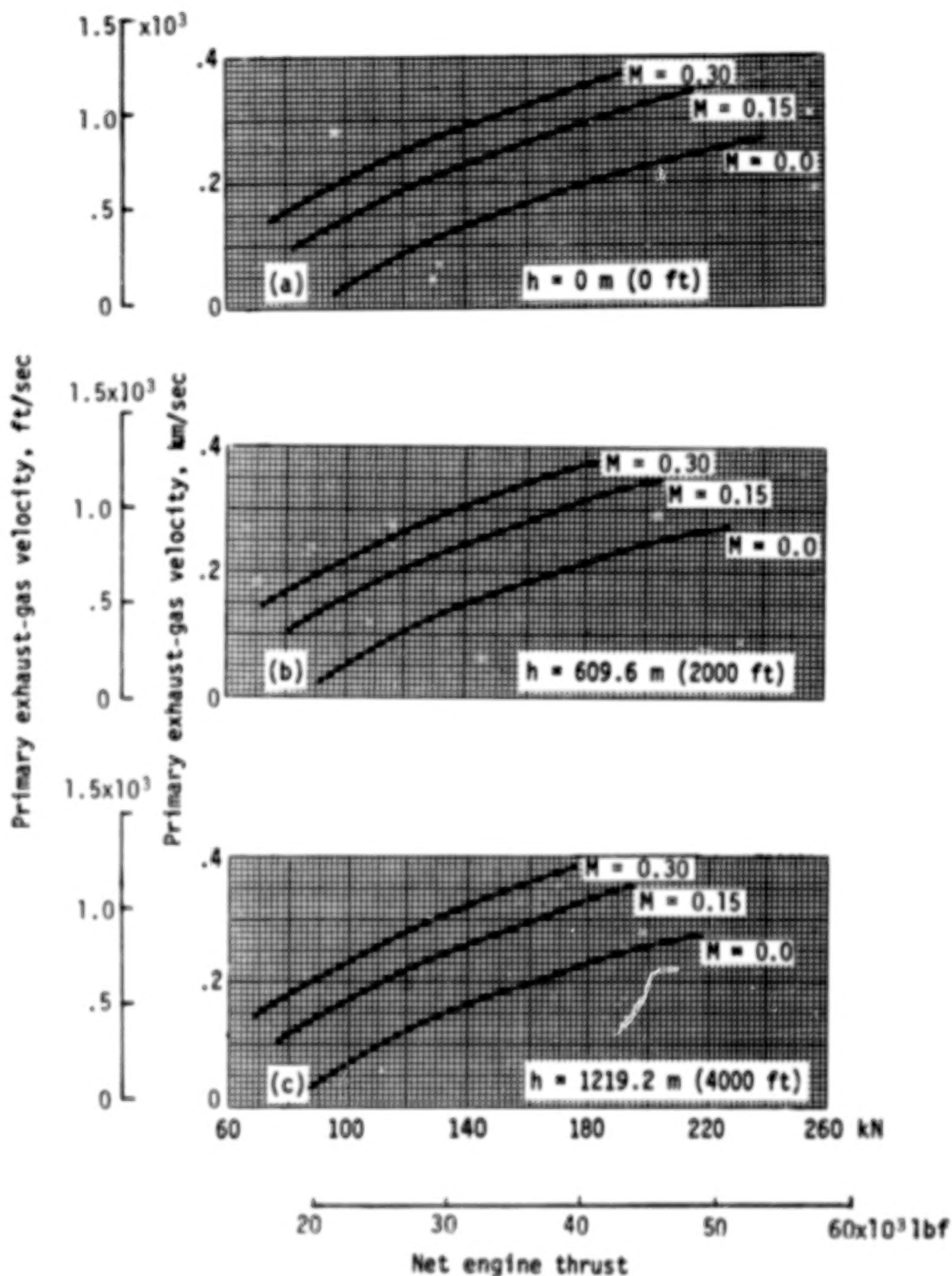
Figure 45.- Installed primary exhaust-gas velocity at take-off
and part-power cruise thrust. Standard day + 10° C.
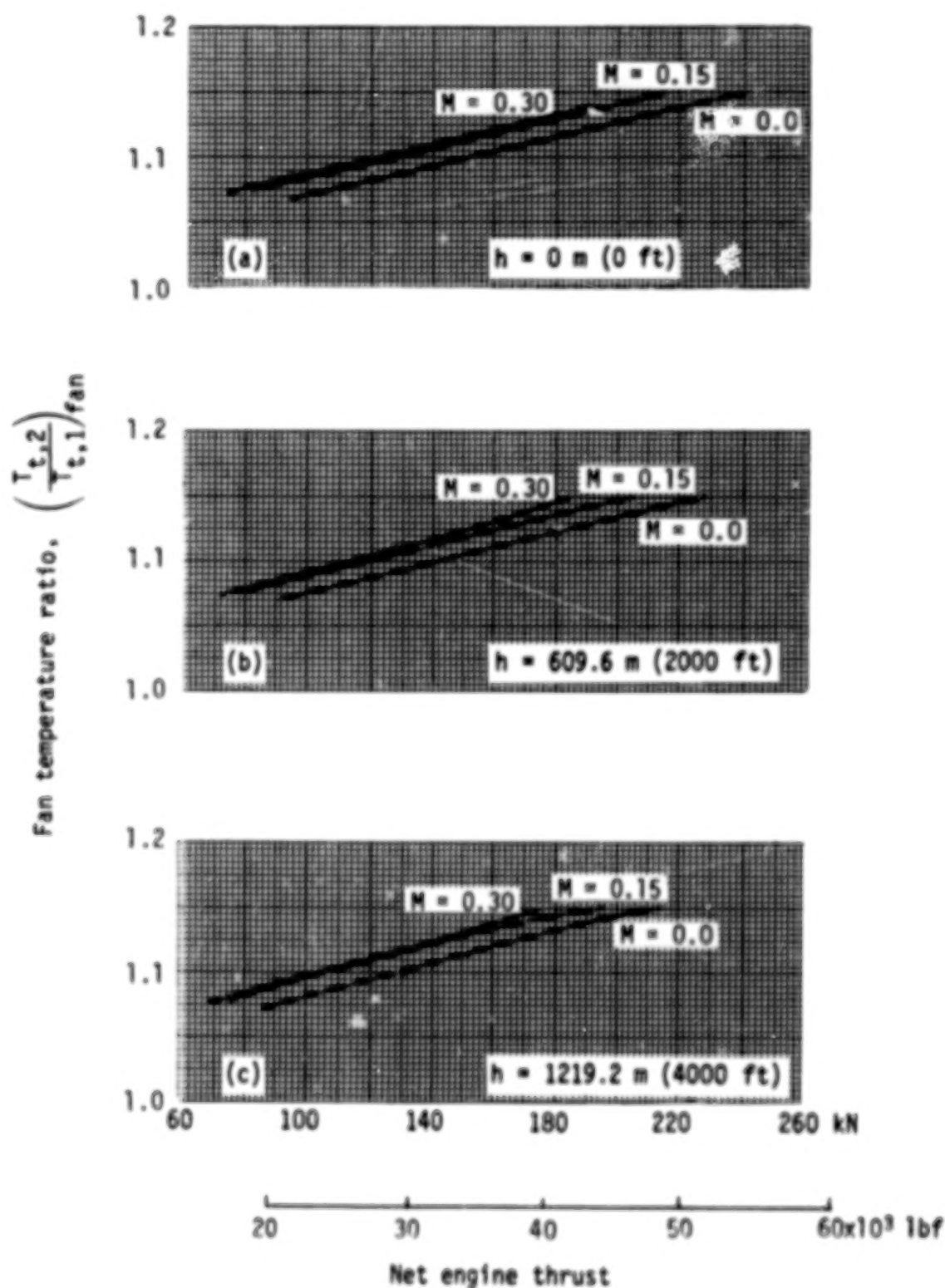
Figure 46.- Installed fan temperature ratio at take-off
and part-power cruise thrust. Standard day + 10° C.

Figure 47.- Installed engine temperature ratio at take-off
and part-power cruise thrust. Standard day + 10° C.
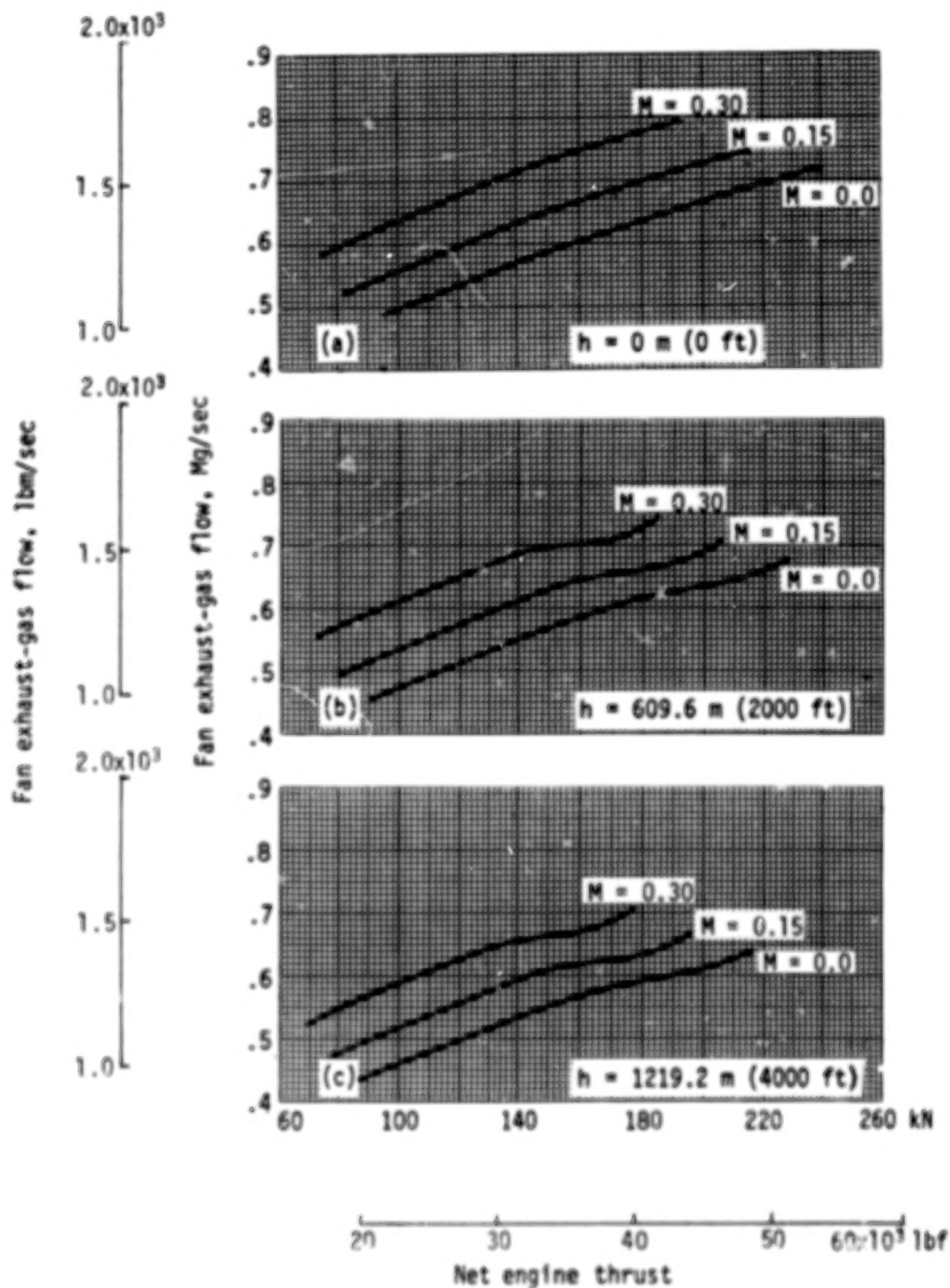
Figure 48.- Installed fan exhaust-gas flow at take-off and part-power cruise thrust. Standard day + 10° C.

Figure 49.- Installed primary exhaust-gas flow at take-off
and part-power cruise thrust. Standard day + 10° C.
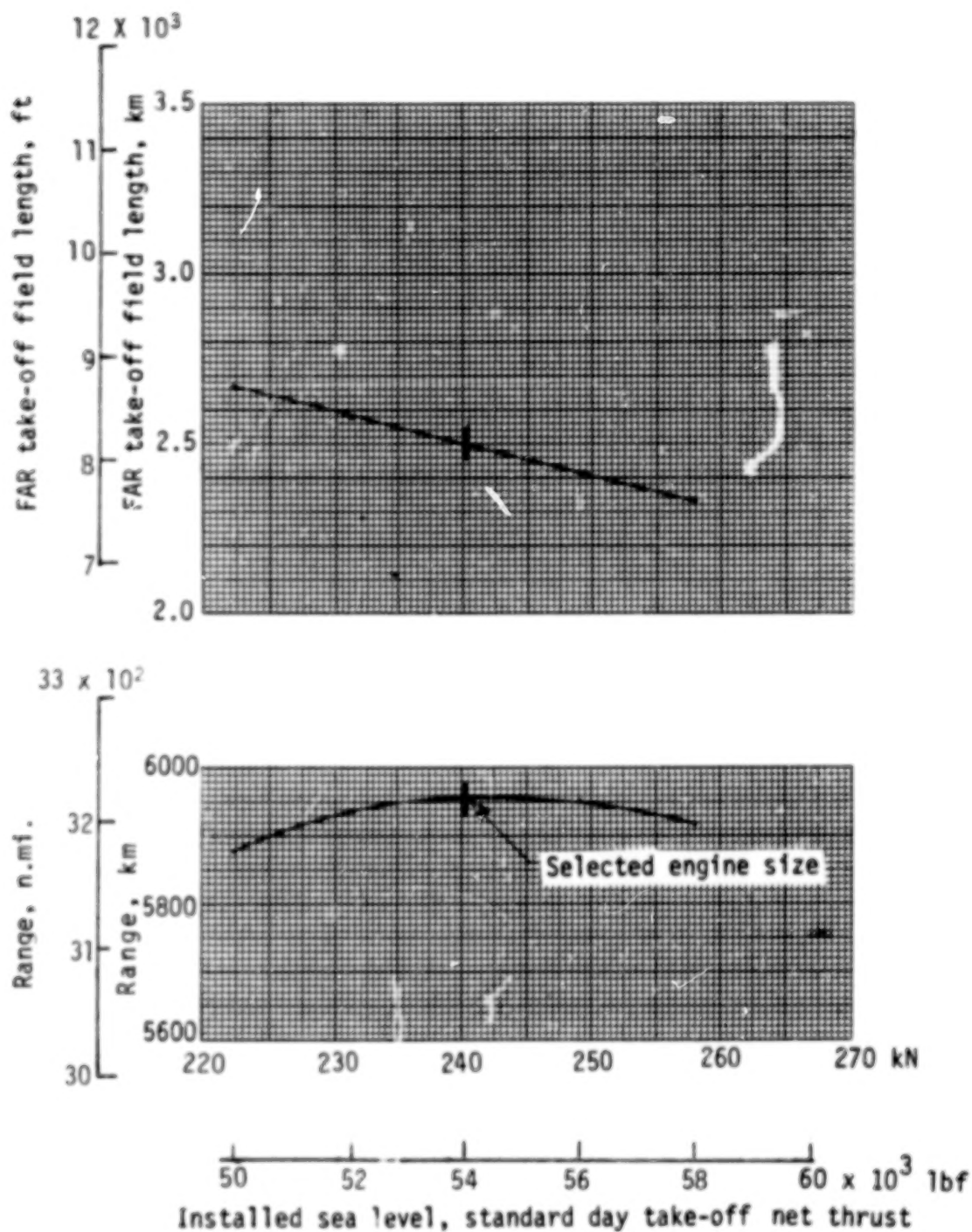
Figure 50.- Effect of engine size on range and FAR take-off
field length. Standard day, sea level, 20° flaps.
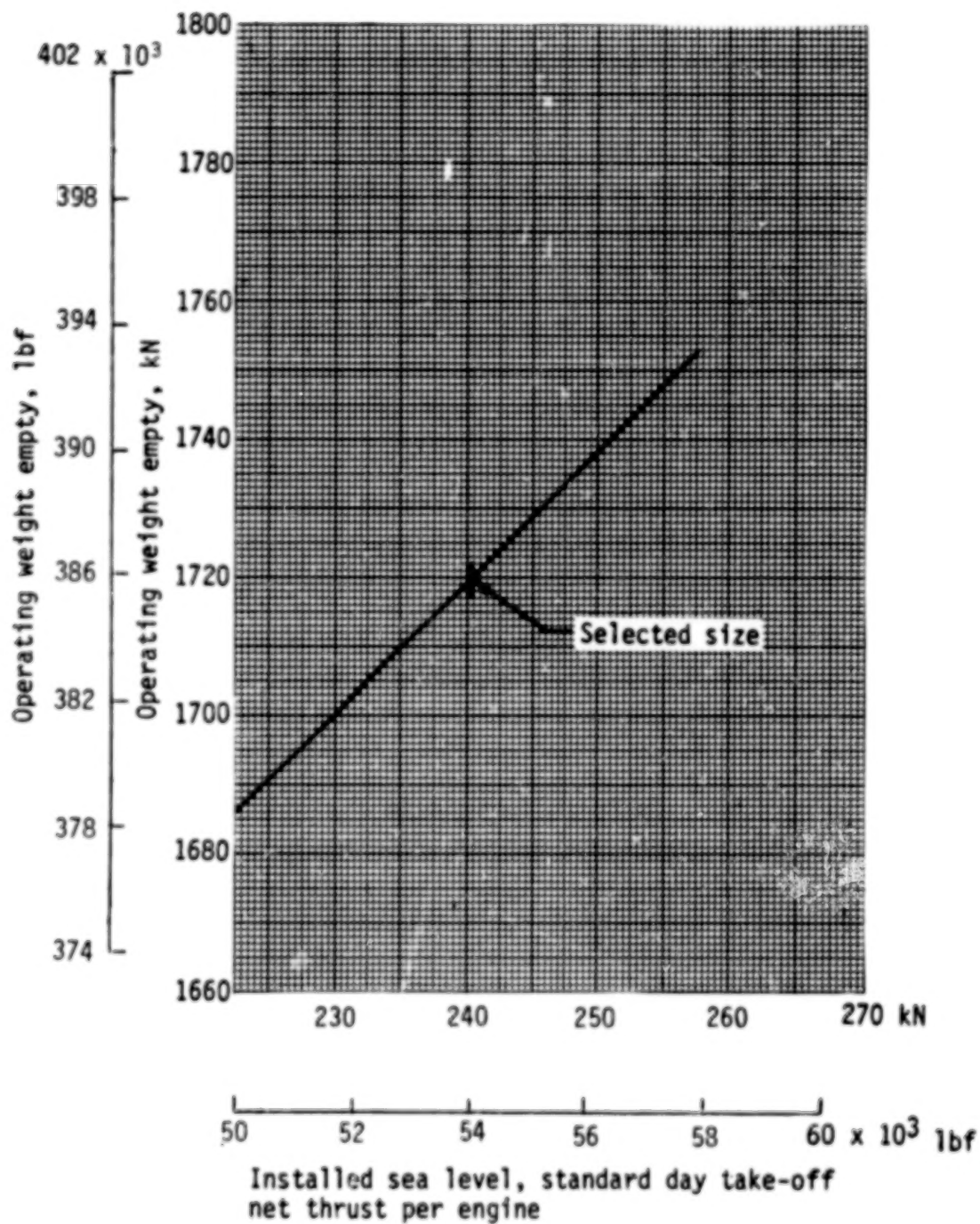
Figure 51.- Effect of engine size on operating weight empty.
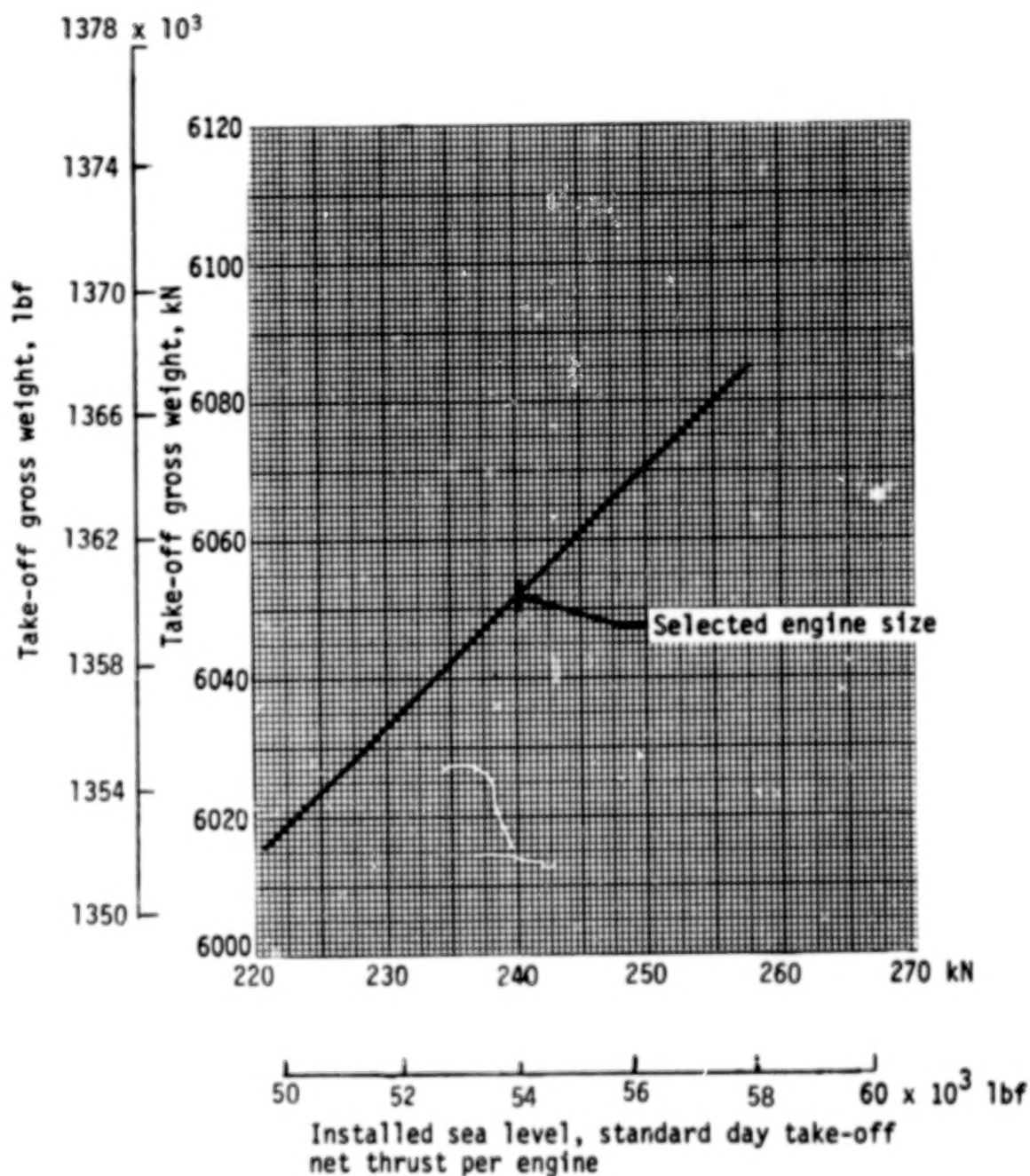
Figure 52.- Effect of engine size on gross weight.
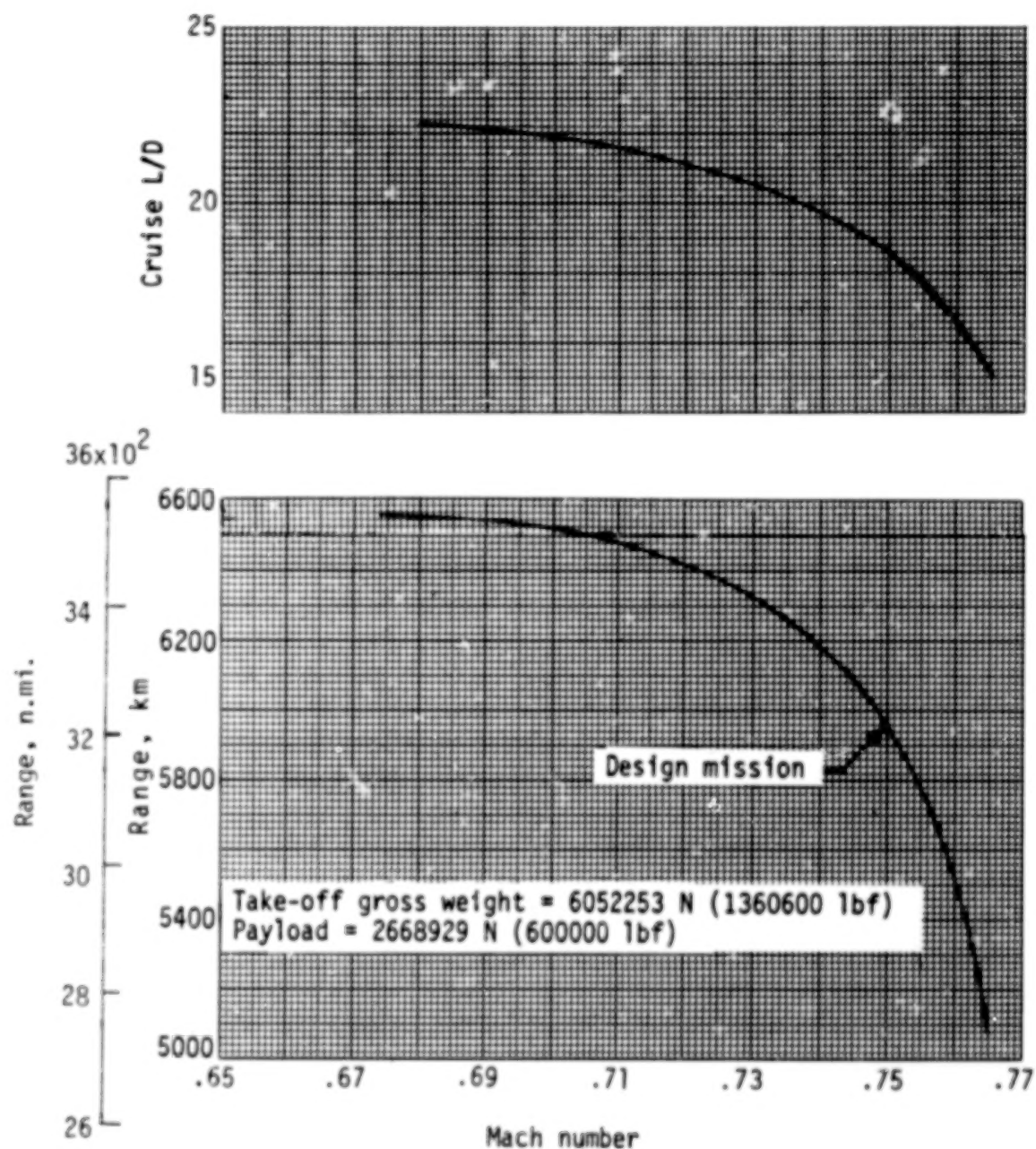
Figure 53.- Effect of Mach number on range and L/D.
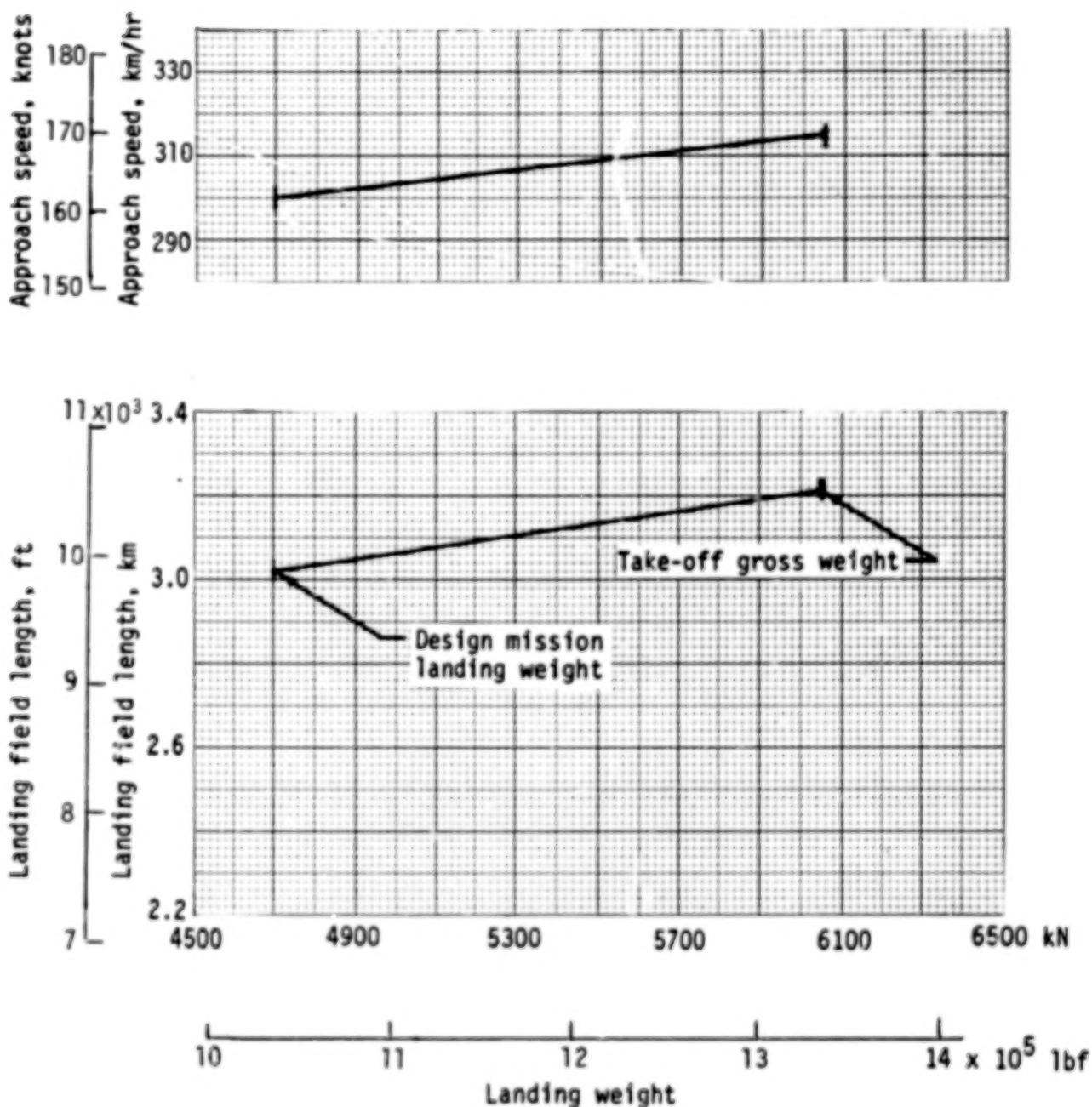
Figure 54.- Landing performance. No reverse thrust; spoilers;
20° flaps. Field length = 1.667 × take-off roll distance.
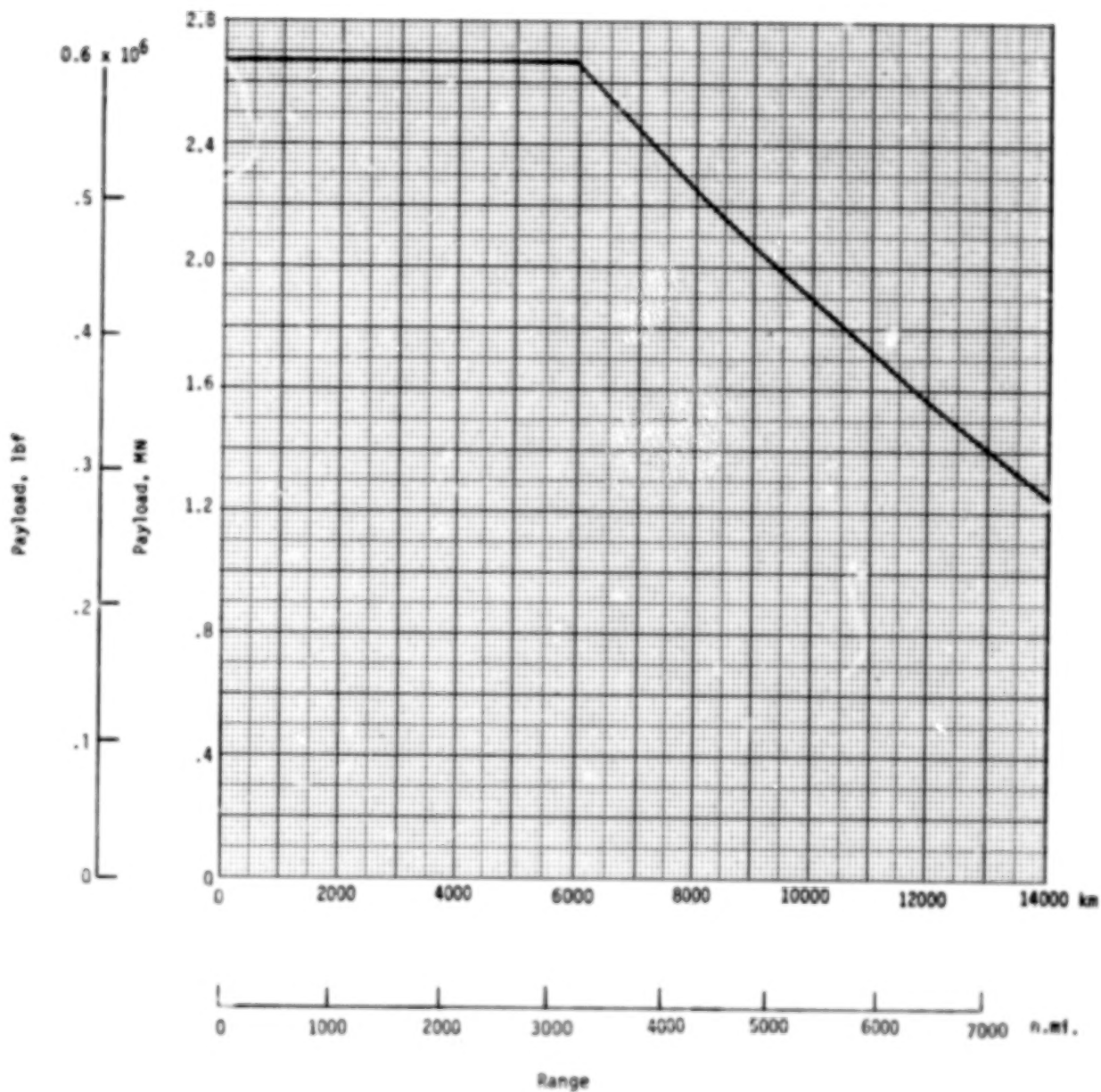
Figure 55.- Variation of payload with range.

89.

Thrust cutback

Threshold point
altitude = 15.24 m
(50 ft)

Lift-off

3°

1853 m
(1.0 n.mi.)

Brake release
for take-off

Runway center line

Point 1

649 m
(.35 n.mi.)

6486 m
(3.5 n.mi.)

Point 2

Ref. 18
Measurement points

Ref. 18 measurement point 3
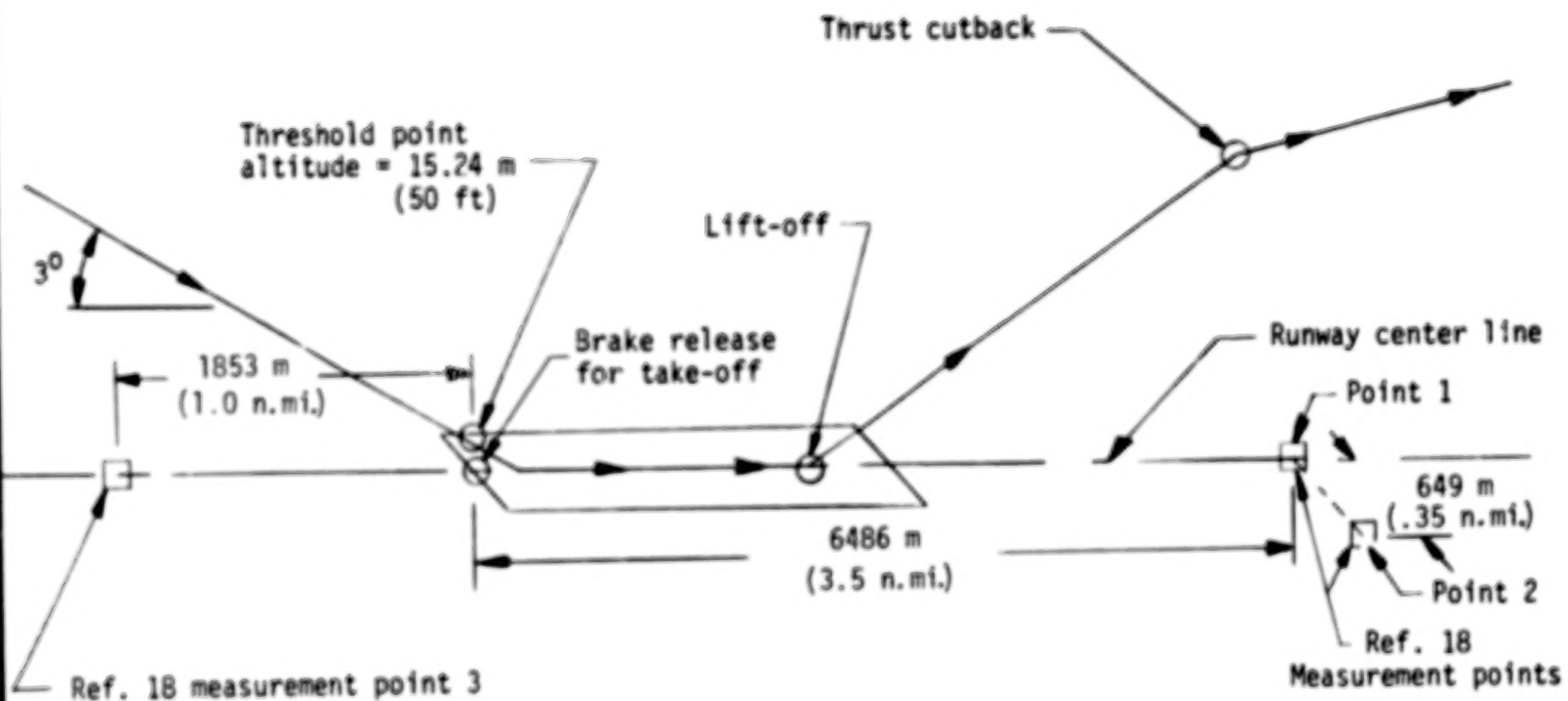
Figure 56.- Noise measurement locations for approach and take-off.
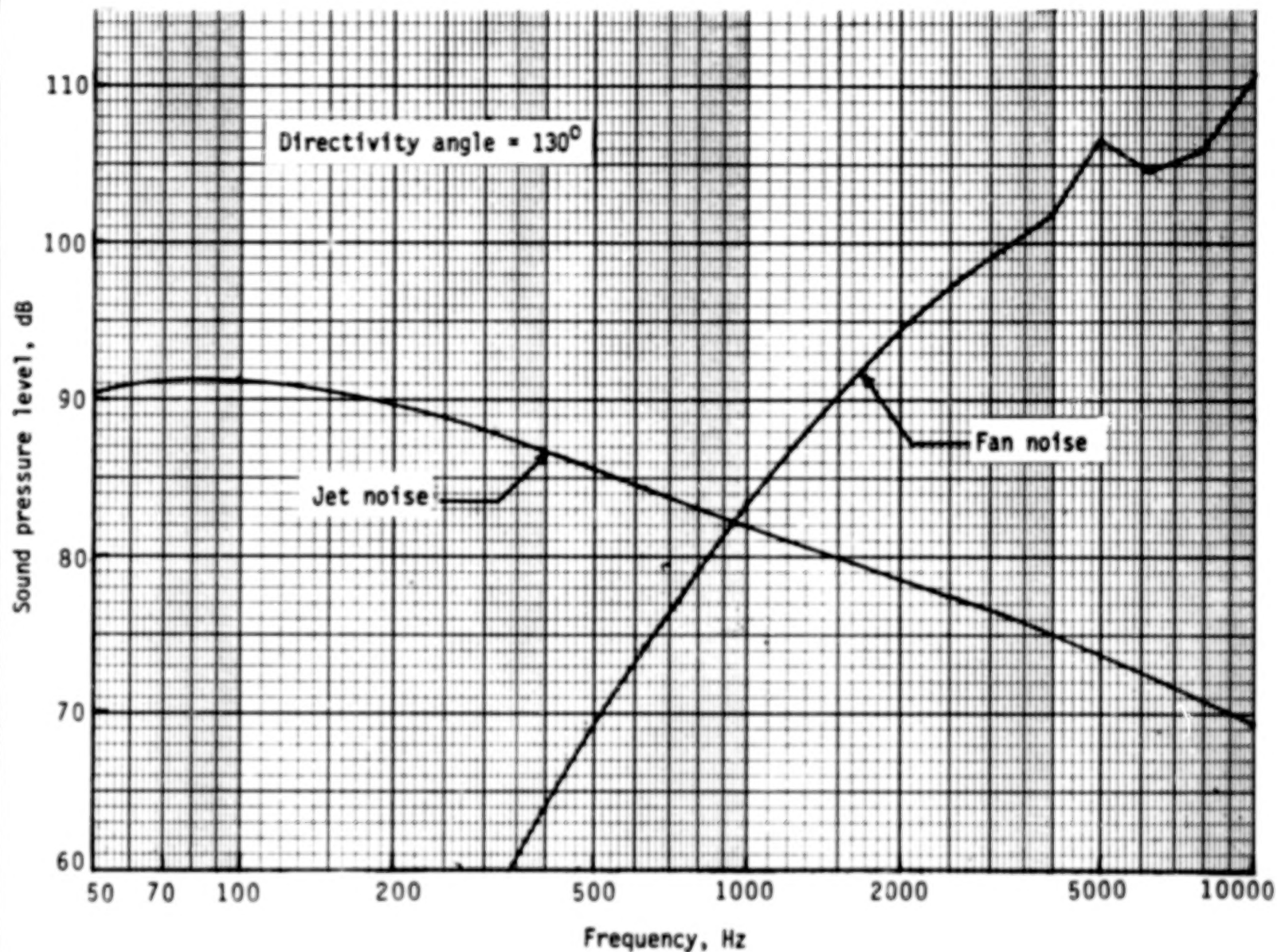
Figure 57.- Variation of engine take-off source noise levels with frequency after thrust cutback.
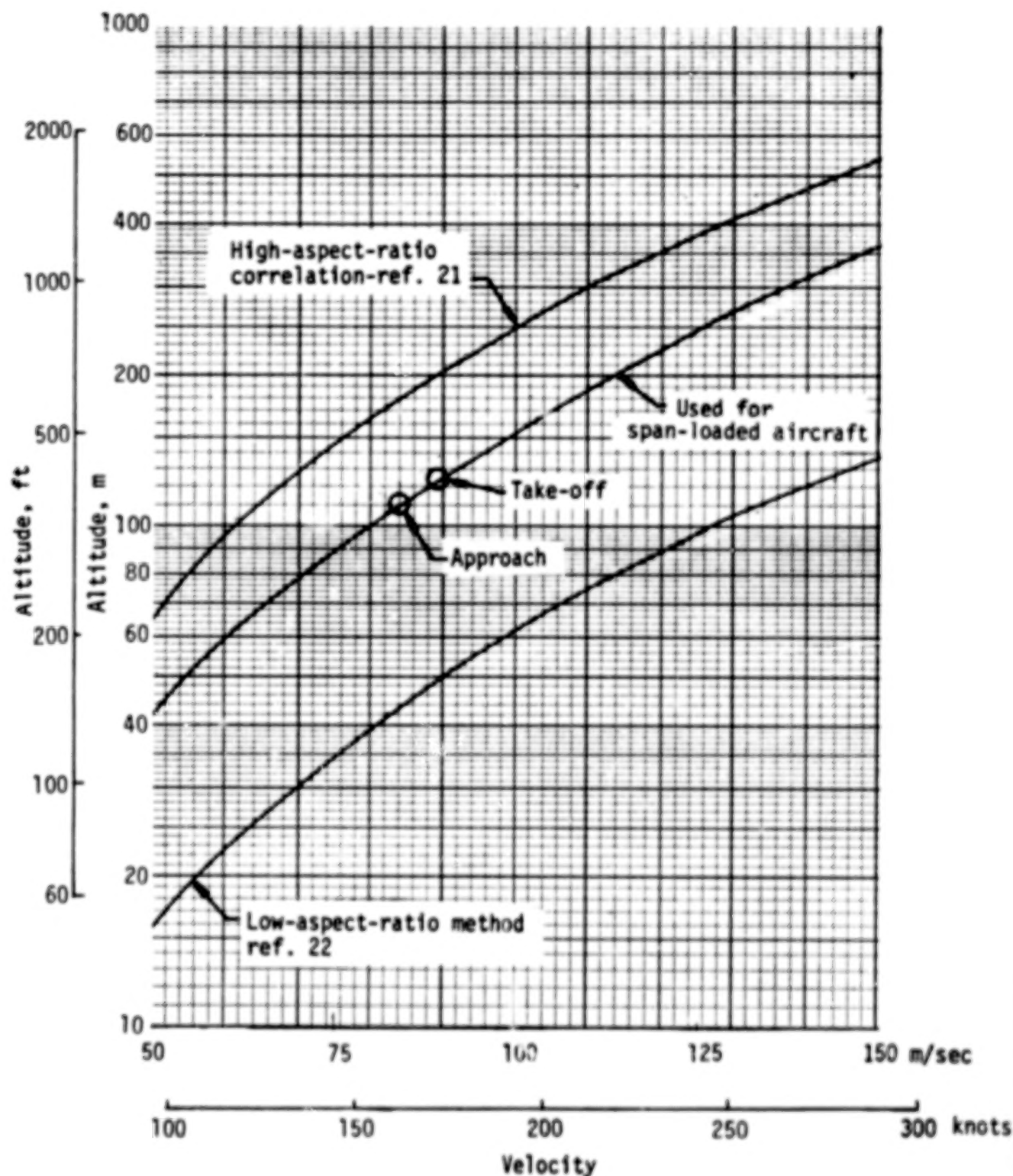
Figure 58.- Variation of altitude with velocity for span-loader airframe noise level of 108 dB. (Airplane is directly over measurement point.)

92
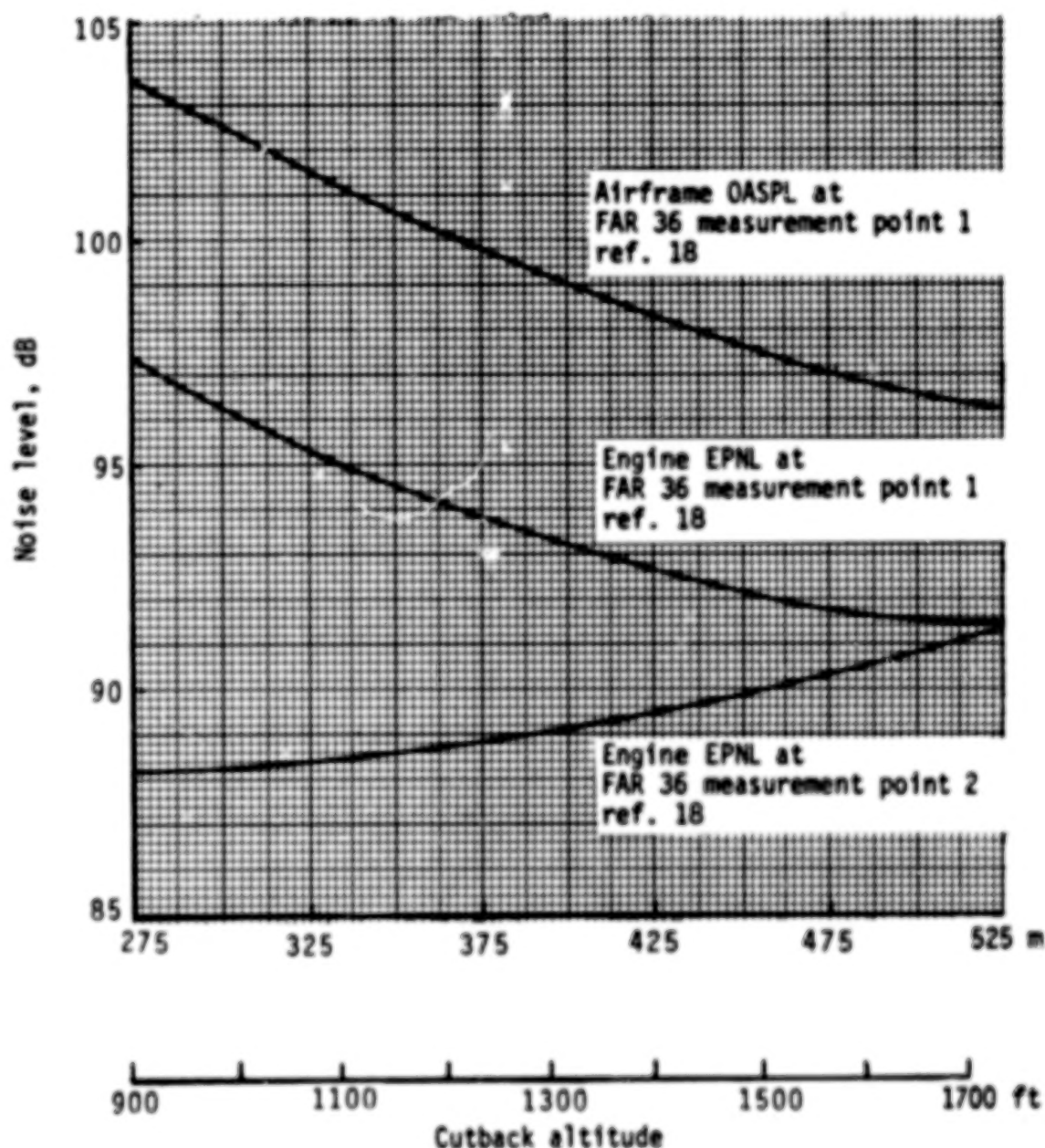
Figure 59.- Effect of cutback altitude on span-loader take-off noise levels.

93.
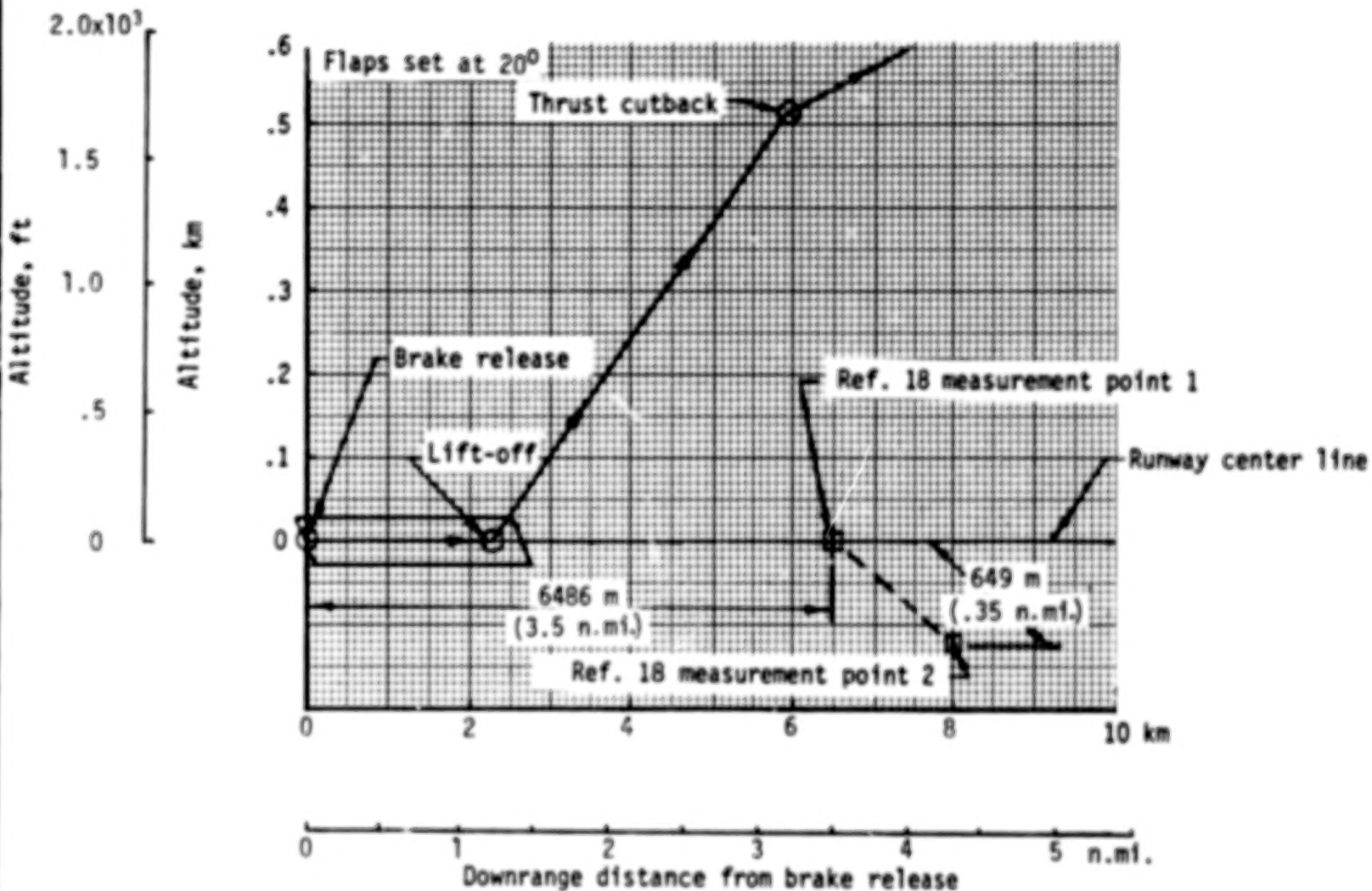
Figure 60.- Take-off profile. Sideline noise is measured where noise level after lift-off is greatest.
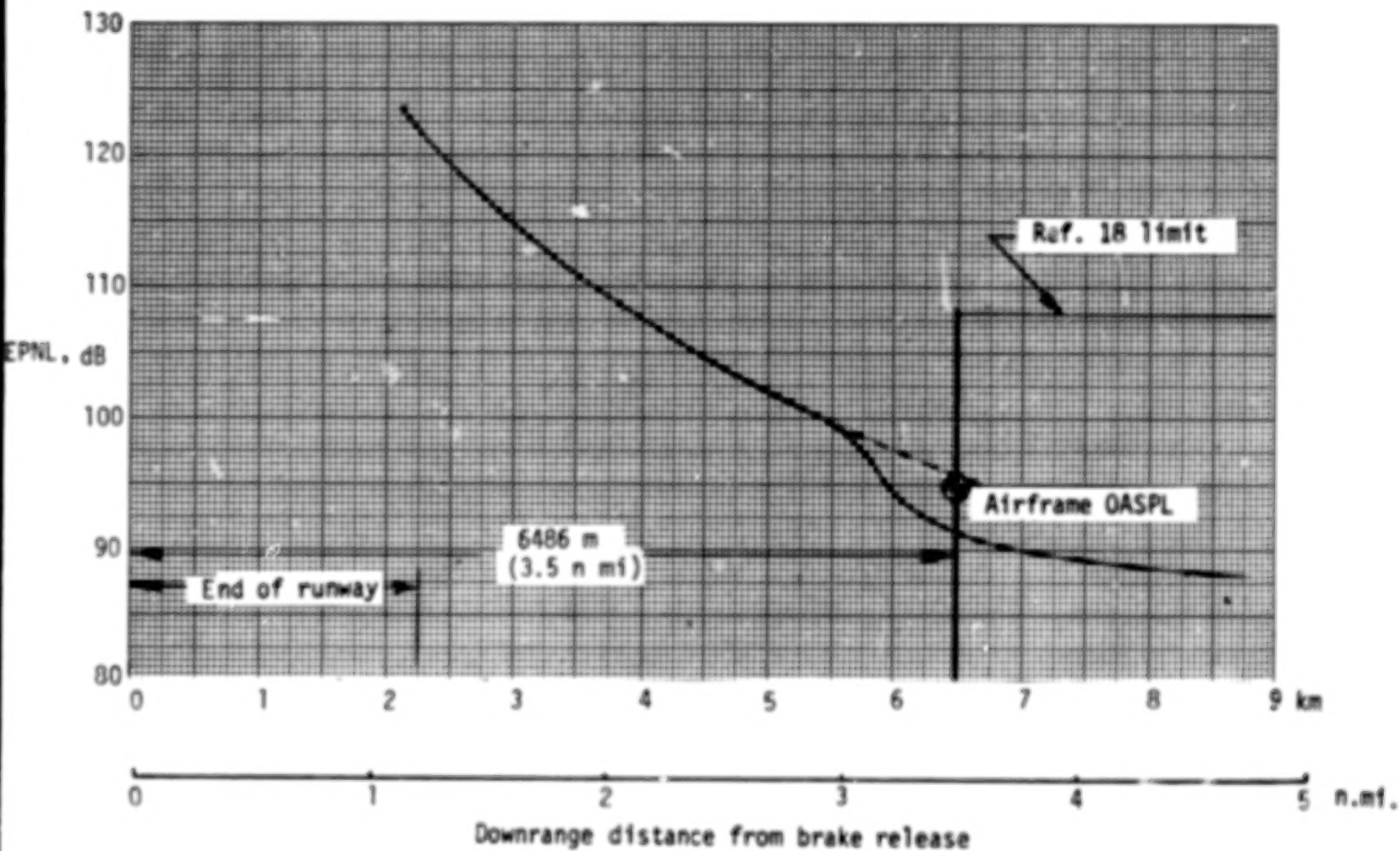
Figure 61.- Effective perceived noise level along runway center
line during take-off.
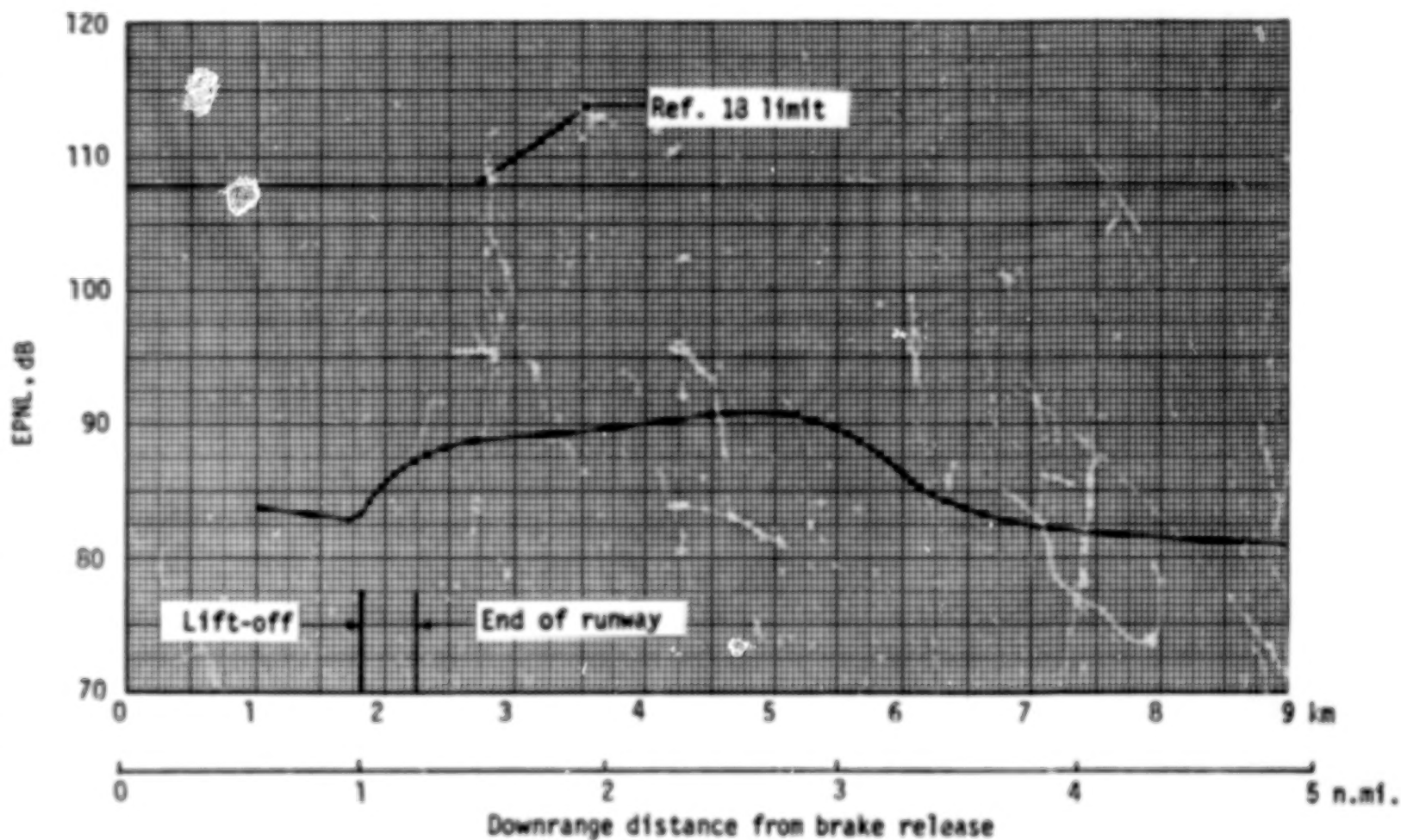
Figure 62.- Effective perceived noise level along sideline during take-off.

96.
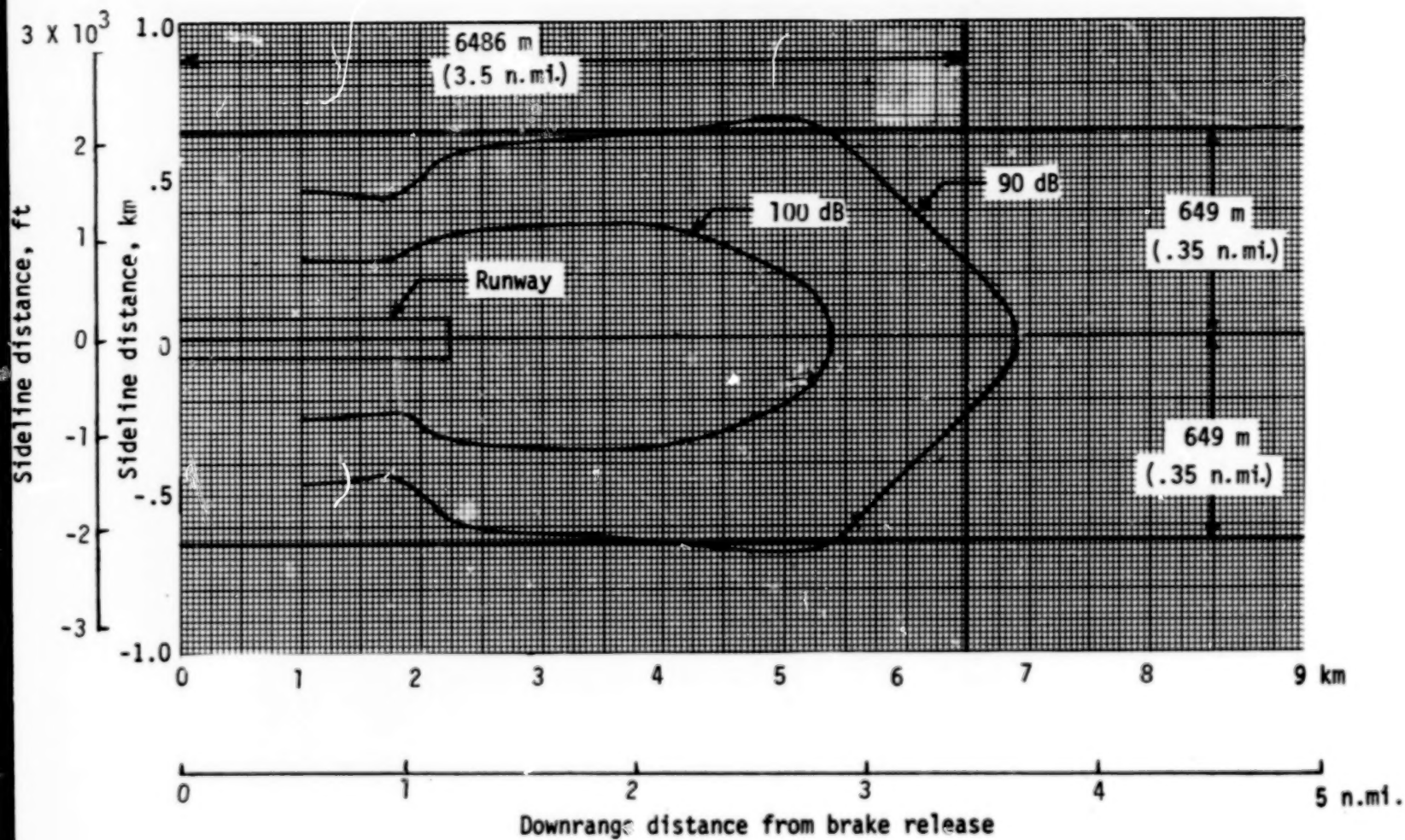
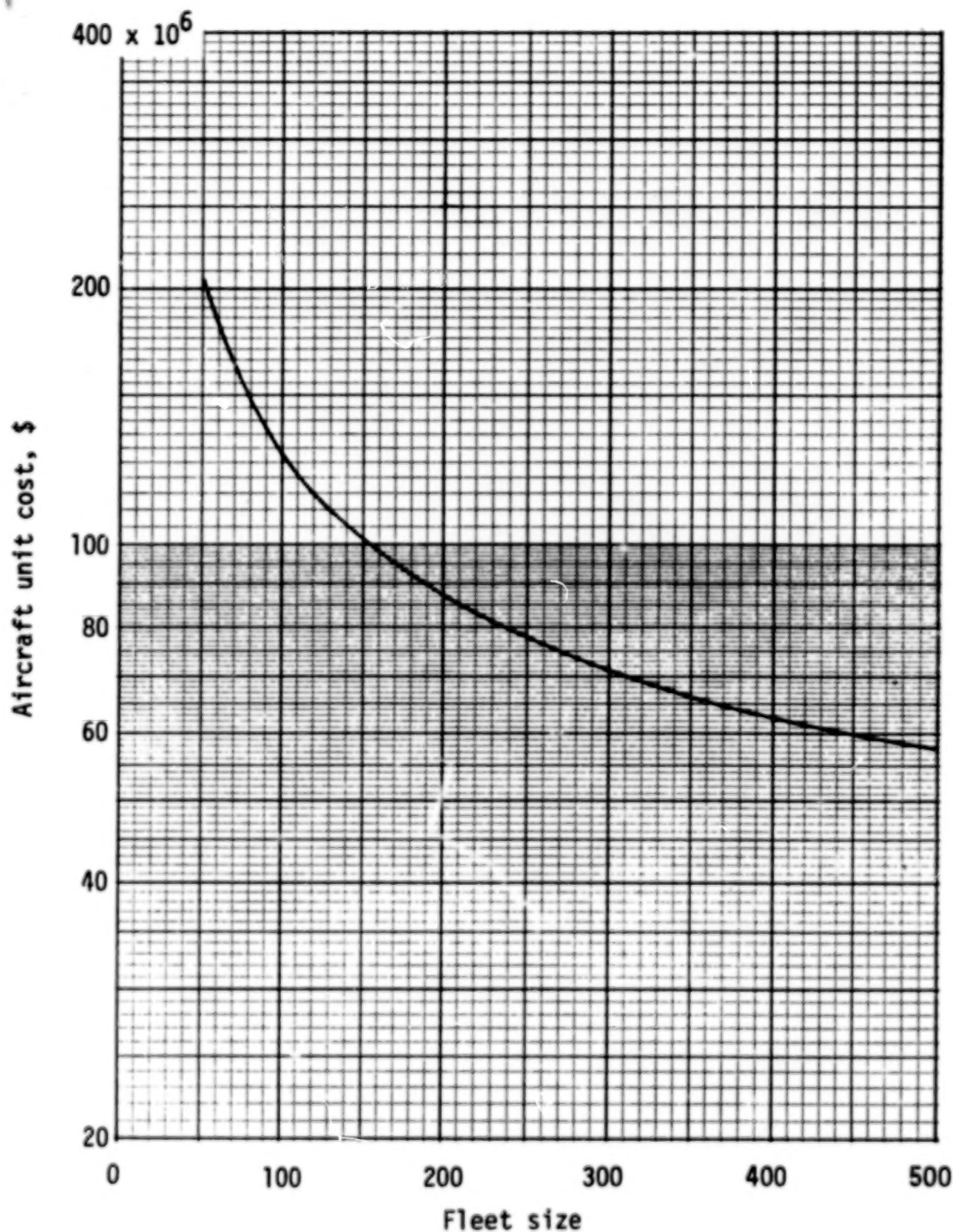Figure 63.- Constant engine effective perceived noise levels during take-off.

97.

Figure 64.- Variation of aircraft unit cost with number of
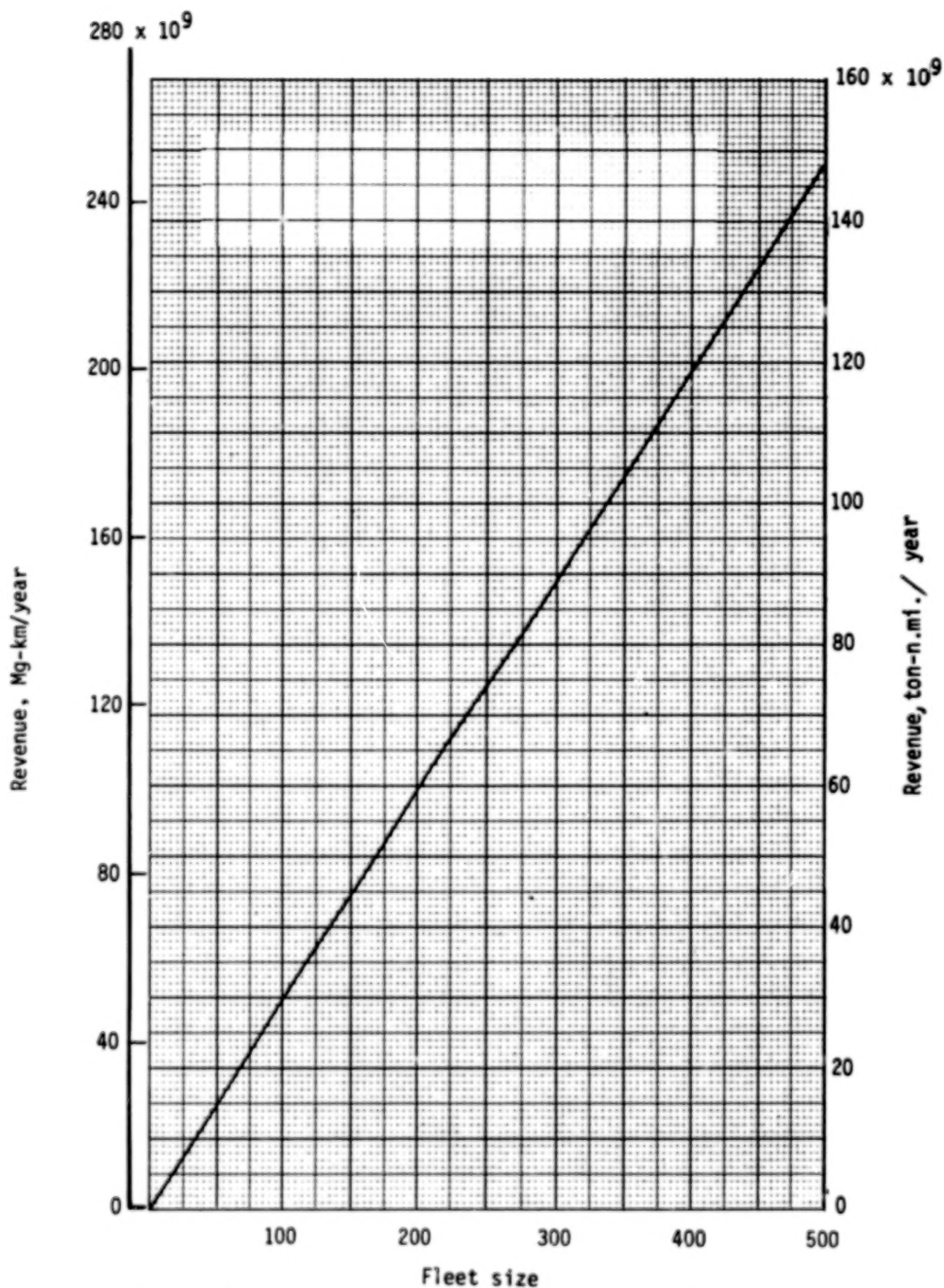units produced, 1977 dollars.

Figure 65.- Variation of productivity with fleet size.
Utilization, 3500 hr/yr; load factor, 0.65; range,
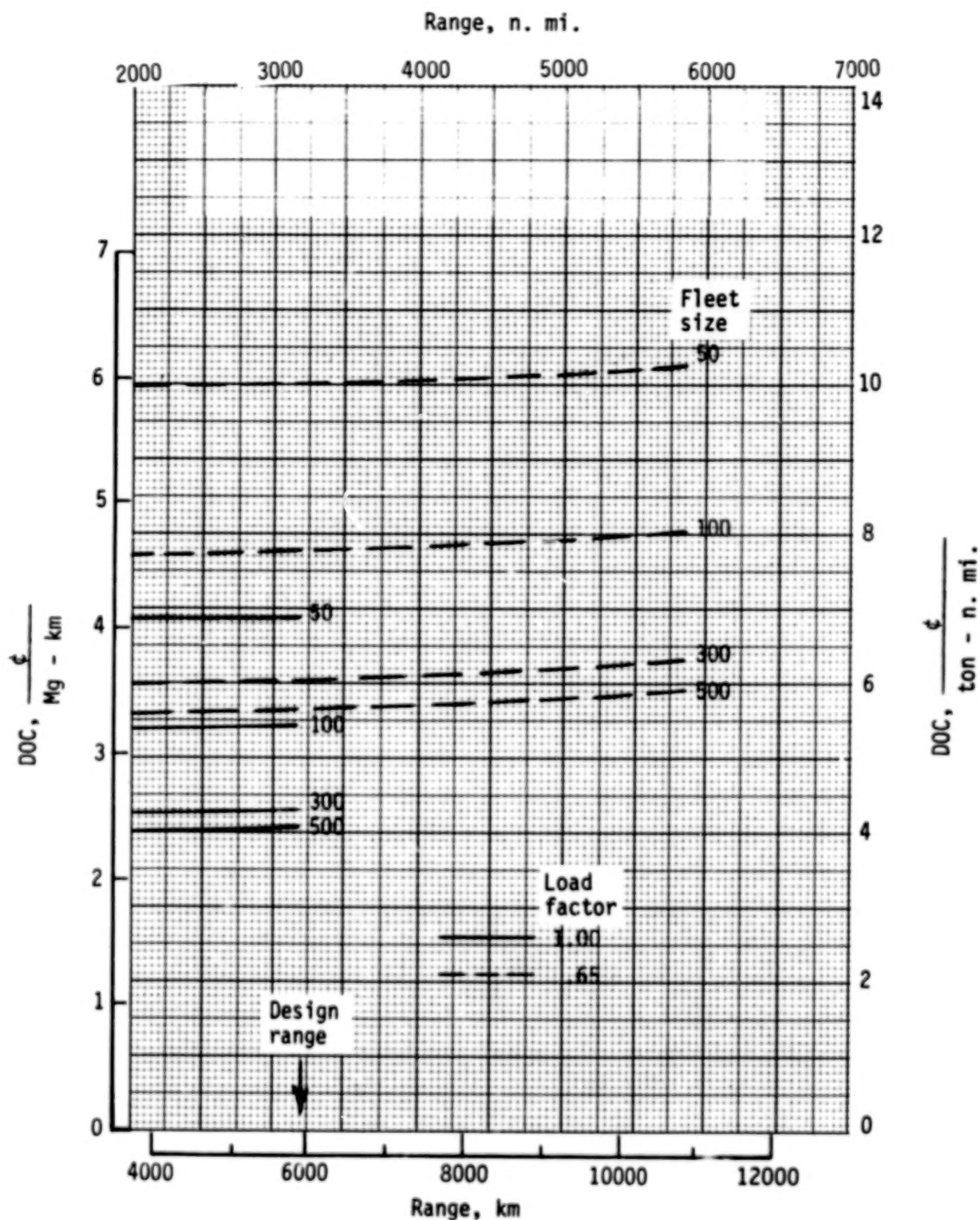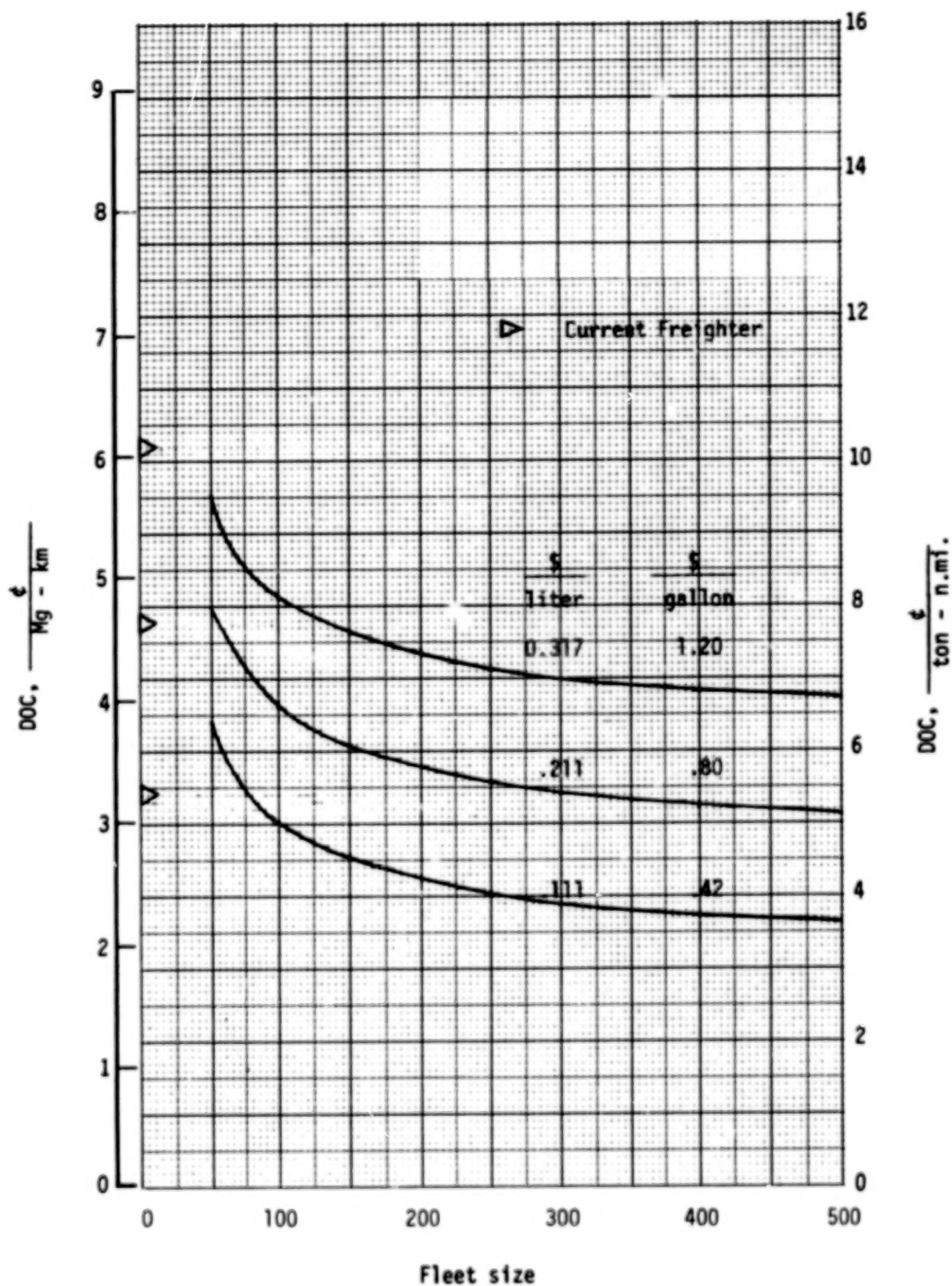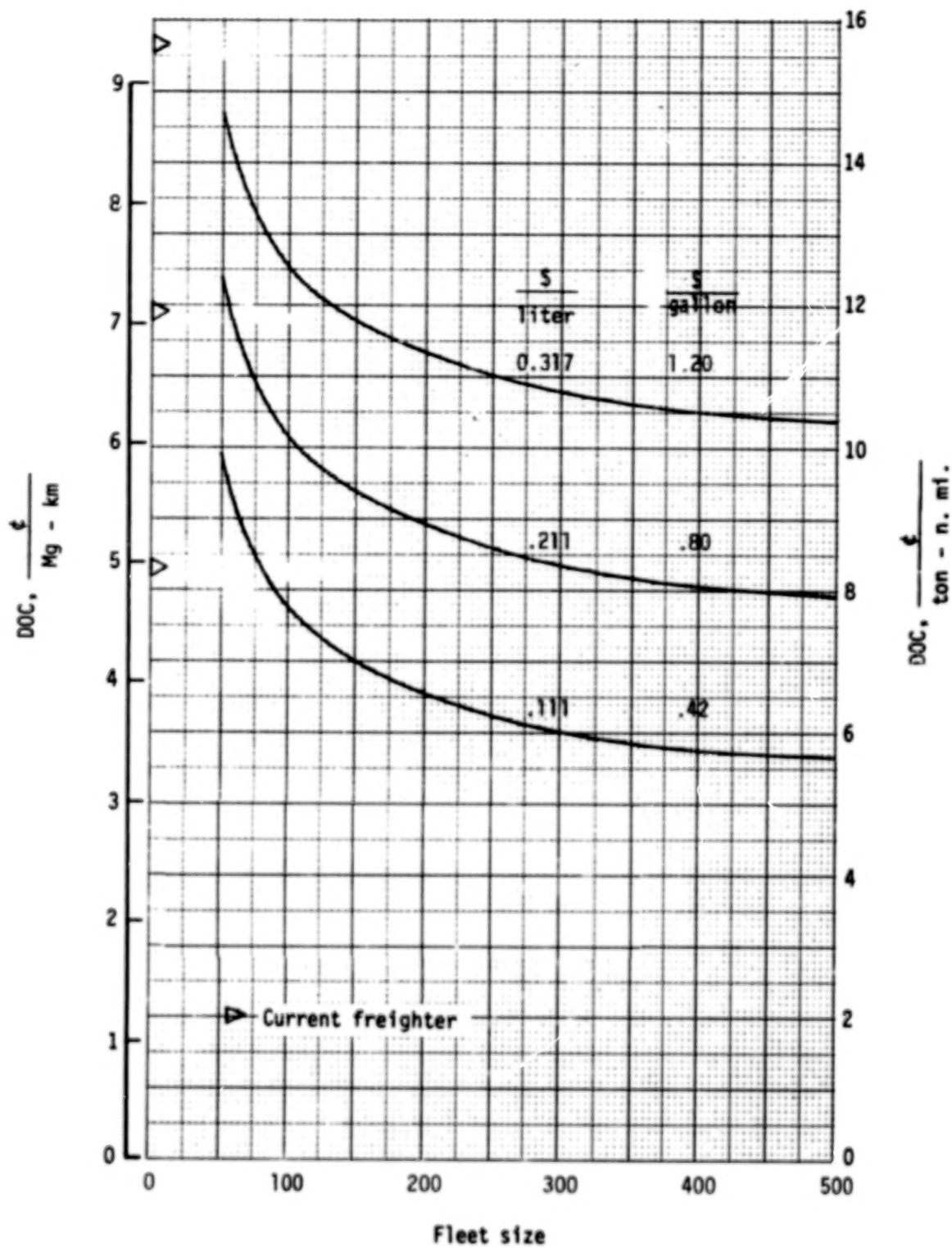5926 km (3200 n. mi.).

Figure 66.- Effect of range and fleet size on direct operating cost. Utilization, 3500 hr/yr; fuel price, $0.111/liter ($0.42/gallon).

(a) Load factor, 1.00.

Figure 67.- Effect of fleet size and fuel cost on direct
operating cost. Utilization, 3500 hr/yr; range,
5926 km (3200 n. mi.).

(b) Load factor, 0.65.

Figure 67.- Concluded.

1. Report No. NASA TP-1158	2. Government Accession No.	3. Recipient's Catalog No.
4. Title and Subtitle PRELIMINARY STUDY OF A LARGE SPAN-DISTRIBUTED-LOAD FLYING-WING CARGO AIRPLANE CONCEPT		5. Report Date May 1978
		6. Performing Organization Code
7. Author(s) Lloyd S. Jernell		8. Performing Organization Report No. L-11943
		10. Work Unit No. 516-50-23-01
9. Performing Organization Name and Address NASA Langley Research Center Hampton, VA 23665		11. Contract or Grant No.
12. Sponsoring Agency Name and Address National Aeronautics and Space Administration Washington, DC 20546		13. Type of Report and Period Covered Technical Paper
		14. Sponsoring Agency Code

15. Supplementary Notes
Portions of the analysis presented herein were conducted by the Vought Corp., Hampton Technical Center, under contract NAS1-13500.

16. Abstract

A preliminary study has been conducted of an aircraft capable of transporting containerized cargo over intercontinental distances. The specifications for payload weight, density, and dimensions in essence configure the wing and establish unusually low values of wing loading and aspect ratio. The structural weight comprises only about 18 percent of the design maximum gross weight. Although the geometric aspect ratio is 4.53, it is estimated that the winglet effect of the wing-tip-mounted vertical tails increases the effective aspect ratio to approximately 7.9.

Sufficient control power to handle the large rolling moment of inertia dictates a relatively high minimum approach velocity of 315 km/hr (170 knots). The airplane has acceptable spiral, Dutch roll, and roll-damping modes. A hardened stability augmentation system is required.

The most significant noise source is that of the airframe. However, for both take-off and approach, the levels are below the FAR-36 limit of 108 dB.

The design mission fuel efficiency is approximately 50 percent greater than that of the most advanced, currently operational, large freighter aircraft. The direct operating cost is significantly lower than that of current freighters, the advantage increasing as fuel price increases.

17. Key Words (Suggested by Author(s)) Advanced cargo aircraft Span-distributed payload Cargo aircraft design	18. Distribution Statement Unclassified - Unlimited
	Subject Category 05

19. Security Classif. (of this report) Unclassified	20. Security Classif. (of this page) Unclassified	21. No. of Pages 102	22. Price* $6.50